

The role of resonances in strong field and ultrafast processes

by

J. Venzke

B.S., Drake University, 2012

M.S., University of Colorado at Boulder, 2020

A thesis submitted to the
Faculty of the Graduate School of the
University of Colorado in partial fulfillment
of the requirements for the degree of
Doctor of Philosophy
Department of Physics
2021

Committee Members:

Andreas Becker, Chair

TBD

TBD

TBD

TBD

Venzke, J. (Ph.D., Physics)

The role of resonances in strong field and ultrafast processes

Thesis directed by Dr. Andreas Becker

Often the abstract will be long enough to require more than one page, in which case the macro “\OnePageChapter” should *not* be used.

But this one isn't, so it should.

TODO

Dedication

To my family and friends.

Acknowledgements

Here's where you acknowledge folks who helped. But keep it short, i.e., no more than one page, as required by the Grad School Specifications.

TODO

Contents

Chapter

1	Introduction	1
1.1	Attosecond time scale	1
1.2	Light sources	2
1.2.1	High harmonic generation	2
1.2.2	Free electron lasers	2
1.3	Organization of this thesis	2
2	Theoretical and experimental background	3
2.1	Attosecond dynamics	3
2.2	Pump prop spectroscopy	3
2.3	Few photon ionization	3
2.4	Rydberg state excitations induce by strong fields	3
2.5	Electron correlation	3
3	Modeling laser atom interactions	4
3.1	Time-dependent Schrödinger equation	4
3.2	Perturbation theory	5
3.2.1	Selection rules	6
3.3	Numerical Methods	7
3.3.1	Coordinate systems	8

3.3.2	Finite difference	9
3.3.3	Radial basis functions	11
3.3.4	Numerical integration	14
3.3.5	Boundary conditions	14
3.3.6	Bound state calculations	16
3.3.7	Continuum states	16
3.3.8	Time propagation	18
3.3.9	Convergence studies	19
3.3.10	Parallel Computing	20
3.4	Single active electron potentials	21
3.5	Observables	22
3.6	Laser pulses	23
3.6.1	Frequency shift ¹	24
4	Imaging attosecond wave packet dynamics with photoelectrons	39
4.1	Short pulse effect in helium	41
4.2	Generalized asymmetry parameters	52
4.2.1	*	55
4.2.2	*	58
4.3	Wavefunction reconstruction method	63
5	Rydberg state excitations induced by intense IR radiation	80
5.1	Linear polarization	81
5.1.1	Short vs. long pulses and CEP effects	86
5.2	Bi-circular polarization	90
5.2.1	Excitation with co-rotating pulses	93
5.2.2	Excitation with counter-rotating pulses	96

¹ The content of this subsection has been also published in J. Venzke et al. PRA **98**, 063409 (2018)

6	Correlation effects in attosecond electron dynamics	102
6.1	Hyperspherical harmonics	102
6.1.1	TDSE in hyperspherical coordinates	103
6.2	Application TBD	113
7	Summary and Prospective	114
	Bibliography	115

Tables

Table

3.1	The relative error of the ground state energy for a hydrogen-like atom with a nuclear charge Z . A grid spacing around 0.1 produces well converged results for $Z = 1$. Excited states have lower relative error.	19
3.2	Coefficients of SAE potentials in Eq. 3.33 for hydrogen, helium, and neon from [62].	21
3.3	Several common analytic pulse envelopes. The conversion factor between N , as defined in Eq. (3.44) (number of cycles within one standard deviation to either side of the maximum), and the more typical N_{FWHM} (number of cycles in the full-width half-maximum of the electric field) is given. The last column shows the excess kurtosis γ_2 , defined in Eq. (3.48), which is independent of the pulse duration T	27

Figures

Figure

- | | | |
|-----|---|----|
| 3.1 | Panels a (b) show the convergence of the lowest energy bound states in Hydrogen without (with) an attached Slater type orbital for various radial spacing (dr). Panel c shows the minimum and maximum imaginary part of the calculated bound state energies. | 13 |
| 3.2 | The finite difference stencil near the edge of the grid. Panel (a) shows how in the fourth order finite difference the stencil extends beyond the grid leading to a boundary condition being imposed at two points. Panel (b) shows the non-centered 4th order stencil that enforces a single boundary condition. | 15 |
| 3.3 | Convergence with respect to grid spacing for various orders of FD for the $1s$ (a), $2s$ (b), and $3s$ (c) states in hydrogen atom. | 20 |
| 3.4 | Scaling results for present Crank-Nicolson method. Two runs each for calculations with 1 million (blue with squares) and 15 million grid points (green with triangles) have been performed. Note that the scaling improves with increasing number of grid points. | 20 |
| 3.5 | Temporal (left) and spectral (right) distributions of vector potential (solid lines) and electric field (dashed line) for pulses with FWHM of 1 cycle (top), and 3 cycles (bottom) at central frequency $\omega_A = 1.0$ a.u. of the vector potential. Also shown is the Gaussian envelope of the vector potential. | 24 |

- 3.6 (Color online) Ratio ω_E/ω_A as a function of the normalized number of cycles N defined in Eq. (3.44). The numerical results were calculated by maximizing $\tilde{E}(\omega)$ for Gaussian (dotted line), sech (dashed-dotted line), and \sin^4 (dashed line) envelopes and are compared with the simple analytic estimate (solid line) given in Eq. (3.43). The inset reveals a slight dependence on envelope shape, which can be attributed to the correction term in Eq. (3.43). 35
- 3.7 (Color online) Photoelectron spectra $P(k)$ as function of photoelectron momentum obtained for interaction of hydrogen atom with laser pulses at central frequencies $\omega_A = 2$ (dashed line) and $\omega_E = 2$ (solid line) and duration of (a) 10 cycles and (b) 2 cycles FWHM. 36
- 3.8 (Color online) Population in $2p$ state following one-photon excitation of hydrogen atom with a laser pulse as a function of ω_A (left) and ω_E (right) for different pulse lengths at peak intensity 10^{12} W/cm². Each line represents results obtained for a fixed pulse duration in terms of $\tau_1 = 405$ as. The results from time-dependent Schrödinger equation (TDSE) calculations (a,b) and predictions within first-order perturbation theory (PT) (c,d) are in excellent agreement. The vertical line marks the energy difference between $2p$ and initial $1s$ state. The green dots indicate the maximum excited state population for each pulse duration. 36
- 3.9 (Color online) Numerical results for population in $2s$ state following 2-photon excitation with $\tau_2 = 811$ as. The vertical line marks half of the energy gap between $1s$ and $2s$ representing the resonance condition for the two photon process. Other parameters are the same as in Fig. 3.8. 37

- 3.10 (Color online) HHG spectrum at driver wavelength 730 nm ($\omega_{\text{central}} = 0.0625$ a.u.) vs. number of cycles N_{FWHM} . In the upper plot the central frequency $\omega_A = \omega_{\text{central}}$ while in the lower panel $\omega_E = \omega_{\text{central}}$. The vertical white dashed lines mark field-free transition energies between excited states and the ground state, while the green solid lines mark the harmonic energies $n_p \omega_E$ with respect to the central frequency of the electric field. 38
- 4.1 Schematic representation of one- (a), two- (b), and three-photon (c) ionization in an ultrashort pulse. The Gaussian distribution shows the spectral width of the ultrashort pulse centered about the energy of the $2p$ -state. The red arrows represent the photon absorption pathways, and the black lines depict some of the resonant structure of the helium atom. 45
- 4.2 Photoelectron angular distributions for helium atom ionized by laser pulses at central photon energy $\omega_0 = 22.2$ eV, peak intensity $I_0 = 10^{11}$ W/cm², carrier-to-envelope phase $\phi = 0$ and three different pulse durations: $N = 0.6$ FWHM cycles (0.112 fs, left column), $N = 1.2$ FWHM cycles (0.224 fs, middle column) and $N = 1.8$ FWHM cycles (0.335 fs, right column). Angular distributions are obtained for three values of photoelectron energy $E = 1.45(2\omega_0 - |E_{1s}|) = 1.0$ a.u. (top row), $E = 2\omega_0 - |E_{1s}| = 0.687$ a.u. (middle row), and $E = 0.58(2\omega_0 - |E_{1s}|) = 0.4$ a.u. (bottom row), where E_{1s} is the energy of the $1s$ state in the SAE potential. 46
- 4.3 Cross section $\sigma(E)$ as a function of peak intensity for photoelectron emission at energy $E = 2\omega_0 - I_p = 18.7$ eV in 0.5-cycle (one-photon process dominates), 1.0-cycle (transition regime), and 1.5-cycle (two-photon process dominates). Central photon energy $\omega_0 = |E_{2p} - E_{1s}| = 22.2$ eV and carrier-to-envelope phase $\phi = 0$. . . 47
- 4.4 Parameters β_1 (a) to β_4 (d) as function of pulse duration (FWHM) and peak intensity. Central photon energy $\omega_0 = |E_{2p} - E_{1s}| = 22.2$ eV, carrier-to-envelope phase $\phi = 0$ and photoelectron energy $E = 2\omega_0 - I_p = 18.7$ eV. 48

- 4.5 Anisotropy parameters β_1 (left) and β_2 (right) as function of pulse duration and photoelectron energy E for central frequencies $\omega_0 = 1.1|E_{1s} - E_{2p}|$ (top row), $\omega_0 = |E_{1s} - E_{2p}|$ (middle row) and $\omega_0 = 0.9|E_{1s} - E_{2p}|$ (bottom row) at peak intensity of 10^{11} W/cm² and $\phi = 0$. In each panel the dashed line corresponds to $E = 2\omega_0 - I_p$. 49
- 4.6 Anisotropy parameter β_5 (a) as function of pulse duration and peak intensity at central frequency $\omega_0 = |E_{1s} - E_{2p}|$ and photoelectron energy $2\omega_0 - |E_{1s}|$ and (b) as function of pulse duration and photoelectron energy at central frequency $\omega_0 = 0.9|E_{1s} - E_{2p}|$ and peak intensity of 10^{13} W/cm². The dotted lines correspond to $E = 2\omega_0 - I_p$ and $E = 3\omega_0 - I_p$. The other parameters are as in Figures 4.4 and 4.5, respectively. 50
- 4.7 Anisotropy parameters β_1 (solid line), β_2 (dashed line), β_3 (dotted line) and β_4 (dashed-dotted line) as function of carrier-envelope-phase. The results averaged using a Gaussian distribution for the CEP (c.f., Eq. (4.6)) with widths of (b) $\alpha = 0.2$ (in units of 2π) and (c) $\alpha = 0.4$ are compared with the unaveraged results (a). Peak intensity: 10^{11} W/cm², central frequency: $\omega_0 = |E_{1s} - E_{2p}|$, pulse duration: 1.2 FWHM cycles and photoelectron energy $2\omega_0 - |E_{1s}|$ 51
- 4.8 Anisotropy parameters β_1 (left) and β_2 (right) as function of pulse duration of the Gaussian window used in modeling the FEL pulses and photoelectron energy averaged over 10 (middle row) and 200 (bottom row) partially incoherent free electron pulses as compared to a single shot result (top row). Peak intensity of the Gaussian window: $I_0 = 10^{11}$ W/cm² and central frequency of the spectral distribution $\omega_0 = |E_{1s} - E_{2p}|$ 52
- 4.9 (a-c): Ionization pathways effective in different intensity and pulse length regimes. (d) Photoelectron angular distributions for ionization of neon atom, prepared in $2p_{-1} - 3d_2$ superposition, as function of intensity and pulse length. (e) The same as (d) including additionally ionization from the $2p_0$ and $2p_1$ states. 75

- 4.10 Conceptual illustration of GAPs (for $\Delta m = 3$). Left: Integrals $I_{\pm}^{even/odd}$, Eqs. (3,4), are defined over regions of constructive and destructive interference, indicated by different colors (dark blue, light blue, dark red, light red), in xy -plane. Middle: GAPs are constructed based on the parity of the parameter $\gamma = l_e + m_e + l_g + m_g + N_p$ from the integrals over the regions denoted by a certain color (light blue, dark red). Right: Exemplary PADs displaying the asymmetry captured by the parameters for even and odd γ 76
- 4.11 Generalized asymmetry parameters A_0^1 (solid lines) and A_1^1 (dashed lines) as function of intensity for ionization of superpositions of $2p_{-1} - 3d_0$ (a), $2p_0 - 3d_1$ (b), and $2p_1 - 3d_2$ (c) in neon atom with initial populations of 0.5 for each state (top row). Results in bottom row for superpositions with populations of $P_{2p_{-1}} = 0.98, P_{3d_0} = 0.02, P_{4s_0} = 0.00057$ (d), $P_{2p_0} = 0.94, P_{3d_1} = 0.06$ (e), and $P_{2p_1} = 0.88, P_{3d_2} = 0.12$ (f). Results have been obtained for one-cycle (blue lines) and four-cycle (orange lines) pulses at photoelectron energy $E = 2\omega - I_p$ 77
- 4.12 Same as Fig. 4.11 but for superpositions generated by a right-handed circularly polarized pulse via one-photon transition in helium atom (a), three-photon transition in neon atom (b), and one-photon transition in neon atom (c) (for details see text). 77
- 4.13 Asymmetry parameter A_1^1 for ionization of helium atom ($1s-2p_1$) with one- and four-cycle pulses at central frequency $\omega = 1.2\omega_0$ 78
- 4.14 Asymmetry parameter A_0^1 for ionization of helium atom ($1s-2p_1$) with one-cycle pulses at central frequency ω_0 . Results of averages over different Gaussian distributions of CEP with width α are compared with those at fixed CEP ($\alpha = 0$, solid line). 78

- 4.15 (a) Isosurfaces of the $1s - 2p_1$ wave function ($|r\Psi|^2$ is shown) evolving in time. (b) Ionization scheme in the $x - y$ plane. The laser polarization along the x -axis is depicted in red, the direction of the ionized electron is shown in orange, and the charge migration is shown in yellow. Selection rules for ground state signal (c) and excited state signal (d). The solid lines illustrate the transitions of photons absorbed at the central frequency and the dashed lines show the pathways for short pulse effect due to the large bandwidth of an ultrashort pulse. 78
- 4.16 Results of TDSE calculations for photoelectron angular distributions as a function of time delay for ionization of $1s - 2p_1$ superposition with ultrashort two-cycle (left column) and ten-cycle (right column) laser pulse with peak intensities of 10^{14} W/cm² (top row), 10^{12} W/cm² (middle row), and 10^{10} W/cm² (bottom row). 78
- 4.17 Errors in amplitude (solid lines with symbols) and phase (dashed lines with symbols) for two-state reconstruction using PADs generated with laser pulses at two, five and ten cycle pulse duration. In the insets the residual $R(\mathbf{a})$ is shown. The reconstruction is based on PADs at 20 time samples ($\Delta t = \tau/20$) using PADs in the full $x - y$ plane (a) and photoelectron signals in forward-backward direction (b). 79
- 4.18 Same as Fig. 4.17(a) but neglecting (a) only the two-photon transition from the excited state and (b) both the one-photon transition from the ground state and the two-photon amplitude from the excited state in the reconstruction. 79
- 4.19 Same as Fig. 4.17 but based on PADs at just two time delays ($\Delta t = \tau/2$). 79
- 4.20 Same as Fig. 4.17(a) but with accuracy of PADs limited to (a) 1% and (b) 10% of maximum value. 79
- 4.21 Same as Fig. 4.17 but for ionization at a detuned photon frequency of $\omega = 0.8\omega_0$ (a) and $\omega = 1.2\omega_0$ (b). Reconstruction is based on full PADs in $x - y$ plane at 20 time delays. 79
- 4.22 Same as Fig. 4.17 but for an arbitrary unknown two-state superposition. Reconstruction is based on full PADs in $x - y$ plane at 20 time delays. 79

4.23	Same as Fig. 4.17 but at peak intensities of 10^{11} W/cm ² (blue lines) and 10^{13} W/cm ² (orange lines) and pulse duration of 2 cycles. Results are shown as a function of variation of (a) carrier-to-envelope phase, (b) peak intensity and (c) both carrier-to-envelope phase and peak intensity. Reconstruction is based on full PADs in $x - y$ plane at 20 time delays.	79
4.24	Same as Fig. 4.17(a) but for the superposition $(1s\rangle + 2p_1\rangle + 3p_1\rangle)/\sqrt{3}$ in the helium atom.	79
5.1	Excited state distribution as function of n (vertical axis) and l (horizontal axis) at the end of 20 cycle pulses with sin squared envelope and peak intensities: (a) $I_0 = 3.4 \times 10^{13}$ W/cm ² , (b) $I_0 = 6.0 \times 10^{13}$ W/cm ² , (c) $I_0 = 8.6 \times 10^{13}$ W/cm ² , and (d) $I_0 = 1.12 \times 10^{14}$ W/cm ² . Left (right) column corresponds to cases in which the Rydberg states are resonant with an even (odd) number of photons.	83
5.2	Same as Fig. 5.1 but for pulses with Gaussian envelope and 14 cycles FWHM. The pulse duration approximately matches that for the sine-squared pulses in Fig. 5.1 at FWHM.	84
5.3	The absorption pathways in an even (odd) photon process in the top (bottom) panel. Green squares represent virtual states with energy $N\omega$ above the ground state and angular momentum l . The yellow squares represent real states labeled by the quantum numbers. Solid lines refer to open pathways while dashed lines represent pathways which are suppressed due to population trapping in a lower excited state. . . .	85
5.4	Excited state distribution as function of l (horizontal axis) and n (vertical axis) at the end of 2 cycle (panels on left), 10 cycle (panels in middle), and 20 cycle (panels on right) pulses, at low peak intensity $I_0 = 3.4 \times 10^{13}$ W/cm ² (top row), and high peak intensity $I_0 = 1.64 \times 10^{14}$ W/cm ² (bottom row).	86
5.5	Population of excited states from a 20 cycle pulse with peak intensity of $I_0 = 1.64 \times 10^{14}$ W/cm ² and CEP of $\phi_A = 0.204\pi$ (a) and $\phi_A = 0.882\pi$ (b)	88

- 5.6 Radiation spectra generated during the pulse (red dashed lines) and those including line emissions after the pulse (black solid lines) are shown for peak intensities: (a) $I_0 = 3.4 \times 10^{13} \text{ W/cm}^2$, (b) $I_0 = 6.0 \times 10^{13} \text{ W/cm}^2$, and (c) $I_0 = 1.64 \times 10^{14} \text{ W/cm}^2$. The vertical gray lines show the field free energy differences between the np energy levels (up to $14p$) and the $1s$ ground state. 99
- 5.7 (Color online) Excited state distribution as function of n (vertical axis) and ℓ (horizontal axis) for (a) $m = -1$, (b) $m = -2$, (c) $m = -3$ and (d) $m = -4$ at the end of 20 (at 800 nm) cycle pulses (40 cycle at 400 nm) with sin squared envelope and total peak intensity of $1 \times 10^{14} \text{ W/cm}^2$ for co-rotating laser pulses of equal intensity. 100
- 5.8 (Color online) Absorption pathways in co-rotating laser pulses at frequencies ω and 2ω starting from a $m = 0$ -state. Without lack of generalization it is assumed that both pulses have left-handed helicity. Absorption of a photon at frequency ω and at frequency 2ω is represented by a red and blue arrow, respectively. The numbers in the boxes denote the minimum number of photons to reach a certain level. 100
- 5.9 (Color online) Excited state distribution as function of orbital angular quantum number ℓ summed over $n \geq 4$ and m at (a) $I_{400} = 5 \times 10^{13} \text{ W/cm}^2$, $I_{800} = 5 \times 10^{12} \text{ W/cm}^2$, (b) $I_{400} = 5 \times 10^{13} \text{ W/cm}^2$, $I_{800} = 1 \times 10^{13} \text{ W/cm}^2$, (c) $I_{400} = 5 \times 10^{13} \text{ W/cm}^2$, $I_{800} = 5 \times 10^{13} \text{ W/cm}^2$, and and (d) $I_{400} = 1 \times 10^{13} \text{ W/cm}^2$, $I_{800} = 5 \times 10^{13} \text{ W/cm}^2$. Pulse durations: 20 cycles at 400 nm, 10 cycles at 800 nm. 100
- 5.10 (Color online) Excited state distribution as function of n (vertical axis) and m (horizontal axis) summed over ℓ . Laser parameters: 20 (800 nm) cycle pulses with sin squared envelope and total peak intensity of $1 \times 10^{14} \text{ W/cm}^2$ for co-rotating laser pulses of equal intensity. 100
- 5.11 (Color online) Distribution in magnetic quantum states for (a) $\ell = 2$ and (b) $\ell = 3$ and different peak intensities of the 800 nm pulse. $I_{400} = 5 \times 10^{13} \text{ W/cm}^2$ and other parameters are as in Fig. 5.10. 100
- 5.12 (Color online) Same as Fig. 5.7 but for counterrotating laser pulses. 100

5.13 (Color online) Absorption pathways in counter-rotating laser pulses at frequencies ω and 2ω starting from a $m = 0$ -state. Without lack of generalization it is assumed that the pulses at frequency ω has left-handed helicity, while the second harmonic pulse has right-handed velocity. Other symbols as in Fig. 5.8.	100
5.14 (Color online) Excited state distributions as a function of m , summed over $n \geq 4$ and ℓ (top), and as a function of n and m , summed over ℓ (bottom), for the interaction with a left-handed circularly polarized laser pulse at 800 nm (20 cycles) and a right-handed circularly polarized laser pulse at 400 nm (40 cycles). Both pulses have the same peak intensity of 5×10^{13} W/cm ²	100
5.15 (Color online) Orbital angular momentum distributions in excited states induced by counter-rotating laser pulses at 400 nm (20 cycles) and 800 nm (10 cycles) at peak intensities of (a) $I_{400} = 5 \times 10^{13}$ W/cm ² , $I_{800} = 5 \times 10^{12}$ W/cm ² , (b) $I_{400} = 5 \times 10^{12}$ W/cm ² , $I_{800} = 5 \times 10^{13}$ W/cm ² , and (c) $I_{400} = 5 \times 10^{13}$ W/cm ² , $I_{800} = 5 \times 10^{13}$ W/cm ²	101
6.1 How the hyperradius (R) relates to the two single-electron sub coordinate systems (r_1, r_2)	104
6.2 The Jacobi coordinates for three body interactions. Each coordinate can be obtained from the previous by utilizing a Raynal-Revai Coefficient	107

Chapter 1

Introduction

In the 1800's, it was not fully understood if all four of a horses' legs left the ground when it was at a full gallop. With the human eye, it is imposible to tell as the effective "shutter speed" of the human eye is to slow to resolve that time scale. In 1878, Eadweard Muybridge published detailing his study of a horse galloping where he shows all of the horses legs leave the ground at the same time when at a full gallop. This is considered the beginning of high speed photography.

- limitations of high speed photography
- Discussion of Eistiens photoelectric effect
- Multiphoton
- Electron motion and attosecond physics

1.1 Attosecond time scale

Throughout this thesis, I will study laser atom on the attosecond (10^{-18} sec) to 10s of femtoseconds (10^{-15} sec). To provide some prospective, it is nice to note that there are more attoseconds in a single second than there are seconds in the lifetime of the universe. On the attosecond time scales, electron motion dominates and the motion of nuclei in molecules are essentially frozen. Having laser pulses with durations as short as 10s of attoseconds, it is possible to image electron structure and generate a "movie" of both the electron and nuclear motion with unprecedented precision.

1.2 Light sources

1.2.1 High harmonic generation

TODO

1.2.2 Free electron lasers

TODO

1.3 Organization of this thesis

Atomic units ($\hbar = e = m = 1$) are used throughout unless noted otherwise.

Chapter 2

Theoretical and experimental background

- 2.1 Attosecond dynamics
- 2.2 Pump prop spectroscopy
- 2.3 Few photon ionization
- 2.4 Rydberg state excitations induce by strong fields
- 2.5 Electron correlation

Chapter 3

Modeling laser atom interactions

In order to study laser atom interactions on the attosecond time scale, one must develop or implement a variety of numerical and analytic tools. Sec. 3.1 introduces the Time-dependent Schrödinger equation (TDSE), Sec. 3.2 introduces the perturbative solution to the TDSE, Sec. 3.3 gives the details for how we solve the TDSE numerically, Sec. 3.4 discusses the various single active electron (SAE) potentials used to model atoms other than Hydrogen, Sec. 3.6 provides details on the laser pulses utilized in the calculations including a frequency correction we helped develop, and Sec. 3.5 provides details on how the various observables are calculated.

3.1 Time-dependent Schrödinger equation

The TDSE can be written as

$$i \frac{\partial}{\partial t} \psi(\mathbf{r}, t) = \hat{H} \psi(\mathbf{r}, t) \quad (3.1)$$

where $i = \sqrt{-1}$ is the imaginary number, \hat{H} is the Hamiltonian which describes the system, and $\psi(\mathbf{r}, t)$ is the time dependent wavefunction. The Hamiltonian for a system with N_e correlated electrons interacting with a laser field and N_n fixed nuclei is

$$\hat{H} = \sum_{e=1}^{N_e} \left(\frac{\hat{\mathbf{p}}_e^2}{2} + V_{las}(\mathbf{r}, t) - \sum_{n=1}^{N_n} \frac{Z_n}{r_{e,n}} \right) + \sum_{e_1 < e_2=1}^{N_e} \frac{1}{r_{e_1, e_2}} \quad (3.2)$$

where $\hat{\mathbf{p}}_e = (-i\nabla_e)$ is the momentum operator of the e^{th} electron, $V_{las}(\mathbf{r}, t)$ is the laser operator, Z_n is the charge of the n^{th} nucleus, and $r_{i,j}$ is the Euclidean distance between particles i and j . The

laser interaction is typically considered using both the dipole and non-relativistic approximation in either the length gauge ($V_{las} = -\mathbf{E}(t) \cdot \mathbf{x}$) or velocity gauge ($V_{las} = -\mathbf{A}(t) \cdot \hat{\mathbf{p}}_e/c$). No analytic solution for more than one electron in a central potential are known as the problem is not separable. Therefore numerical methods are required. Solving the TDSE accurately in full dimensions for more than one electron is extremely difficult and next to impossible for three or more active electrons. For most studies, we make the single active electron approximation (SAE) where all except one 'active' electron and the nuclei are fixed in space. A SAE potential generated by the nuclei and remaining electrons is then used to model the interaction of the active electron with the fixed electrons and nuclei. The SAE Hamiltonian of an atom interacting with a laser field therefore becomes

$$\hat{H} = \frac{\hat{\mathbf{p}}^2}{2} + V_{las}(\mathbf{r}, t) + V_{SAE}(r), \quad (3.3)$$

where $V_{SAE}(r)$ is the SAE potential. The exact form of the SAE potentials used in this work is given in Sec. 3.4. Extensions on two-active electron calculation beyond the SAE approximation are discussed in Chapter 6. Finally, it is often convenient to split the problem into a field free Hamiltonian (\hat{H}_0) and the time dependent laser field such that

$$\hat{H} = \hat{H}_0 + V_{las}(\mathbf{r}, t). \quad (3.4)$$

The resulting H_0 is time independent and its associated Eigenfunctions can be used to analyze the results of a simulation.

3.2 Perturbation theory

In the case of a weak laser field (typically intensities $< 10^{13}$ W/cm²) relative to the atomic potential the TDSE can be solved using perturbation theory (PT). In some cases, such as for the hydrogen atom, the corresponding terms of the perturbation series can be solved analytically. However, for many of the SAE potentials that we use there is no analytic solutions. In such a case, a numerical solution to the first-order terms of the series provides much of the same insight.

Therefore, it is advantageous to provide a general framework that can be used for both analytical and numerical solutions. We start by diagonalizing the field free Hamiltonian H_0 to

discretize both the bound (Sec. 3.3.6) and continuum states (Sec. 3.3.7). The result can be written as a Green's function

$$G_0(t, t') = \sum_g e^{-iE_g t} |\phi_g(t)\rangle \langle \phi_g(t')| e^{iE_g t'}, \quad (3.5)$$

where $|\phi_g(t)\rangle$ are the field free states (both bound and continuum), E_g is the energy of the state, and t denotes time. For some initial wavefunction $|\Psi_0(\mathbf{r}, t)\rangle$, the consecutive orders of the PT can be obtained via

$$|\Psi_{i+1}(\mathbf{r}, t)\rangle = \int_{-\infty}^t dt_1 G_0(t, t_1) V_{las}(t_1) |\Psi_i(\mathbf{r}, t_1)\rangle, \quad (3.6)$$

with $i = 0, 1, 2, \dots$. The total wavefunction in N th order can then be obtained via a sum such that

$$|\Psi(\mathbf{r}, t)\rangle^{(N)} = \sum_i^N |\Psi_i(\mathbf{r}, t)\rangle. \quad (3.7)$$

By taking $N \rightarrow \infty$, the resulting wavefunction is exact in the regime where the perturbation is small as compared to other interaction terms. However, if the perturbation is of similar order as compared to other terms in the Hamiltonian, the series will not converge to the correct answer leading to the breakdown of PT. The wavefunction obtained using PT can be used to extract observables (Sec. 3.5) in the same way as for a (full) numerical solution of the TDSE. Additionally, for laser-matter interactions PT offers the option to analyze the wavefunction of a particular order to extract further information about how many photons are involved in a process.

3.2.1 Selection rules

The wavefunction is often expanded in 3D spherical harmonics to take advantage of selection rules for interactions with an electric field. We proceed by considering the selection rules for length gauge ($V_{las} = -\mathbf{E} \cdot \mathbf{r}$). For simplicity, we consider a linearly polarized laser field along the z -axis, i.e.

$$V_{las} = -E_z z. \quad (3.8)$$

Noting that $z = r \cos(\theta)$ we obtain

$$V_{las} = -E_z r \cos(\theta) \quad (3.9)$$

$$= -2E_z r \sqrt{\frac{\pi}{3}} Y_1^0(\theta, \phi), \quad (3.10)$$

where $Y_\ell^m(\theta, \phi)$ is a spherical harmonic. This expansion can then be used to calculate the angular portion of a matrix element between two wavefunctions with V_{las} as a perturbation:

$$\langle Y_{\ell'}^{m'} | V_{las} | Y_\ell^m \rangle = -2E_z r \sqrt{\frac{\pi}{3}} \langle Y_{\ell'}^{m'} | Y_1^0 | Y_\ell^m \rangle. \quad (3.11)$$

The integral over three spherical harmonics can be written as

$$\int_{4\pi} Y_{\ell_1}^{m_1*} Y_{\ell_2}^{m_2*} Y_L^M = \sqrt{\frac{(2\ell_1+1)(2\ell_2+1)}{4\pi(2L+1)}} \langle \ell_1, 0, \ell_2, 0 | L, 0 \rangle \langle \ell_1, m_1, \ell_2, m_2 | L, M \rangle, \quad (3.12)$$

where $\langle \ell_1, m_1, \ell_2, m_2 | L, M \rangle$ is a Clebsch–Gordan coefficient. Thus, we get

$$\langle Y_{\ell'}^{m'} | V_{las} | Y_\ell^m \rangle = -E_z r \sqrt{\frac{(2\ell_1+1)(2\ell_2+1)}{3(2L+1)}} \langle \ell', 0, 1, 0 | \ell, 0 \rangle \langle \ell', m', 1, 0 | \ell, m \rangle, \quad (3.13)$$

which is only non-zero for $\ell' = \ell \pm 1$ and $m' = m$. Therefore, the selection rules for a linearly polarized laser along the z -axis are given by $\Delta\ell = \pm 1$ and $\Delta m = 0$. Similarly, for a linearly polarized laser along either the \hat{x} or \hat{y} axis one gets $\Delta\ell = \pm 1$ and $\Delta m = \pm 1$. Finally, a circularly polarized laser in the xy -plane leads to $\Delta\ell = \pm 1$ and $\Delta m = 1$ for absorbing a photon from a right-handed circularly polarized field and $\Delta\ell = \pm 1$ and $\Delta m = -1$ for absorption of a photon from a left-handed circular polarized laser field. By taking advantage of these selection rules, one can greatly reduce the size of a wavefunction used in a particular order of PT or in a numerical TDSE solution.

3.3 Numerical Methods

For much of the parameter regime we are interested in, perturbation theory fails as an approximation method. Therefore, we have developed and implemented numerical solvers of the TDSE. As for most partial differential equations, numerical solutions to the TDSE have a relatively simple

general form with the complexity hidden in the details. First, one chooses a basis/discretization to write down the solution, in our case the wavefunction. Next, the operators are expanded in the basis and written as a matrix. Then, one obtains a set of initial conditions at the start of the simulation, in our case typically a bound state of the atom or molecule. Finally, the initial condition is propagated in time with updates to the operating matrix between time steps. In this section, we will layout the basis/discretization choices in Sec. 3.3.1, followed by a detailed discussion of the implementation in the remaining subsections. For the sake of simplicity, we will focus on single active electron calculations in this section (for details on two-active electron calculation see Chapter 6).

3.3.1 Coordinate systems

The solution to a single active electron calculation is three dimensional in space. The simplest and most general strategy would be to expand the wavefunction on a 3D grid in real space with the atom or molecule placed in the center. Such a grid is generated by discretizing each dimension (1D problem) with N grid points and then taking a Kronecker product producing a 1D vector that represents the full 3D Cartesian space. The derivative operators can then be discretized utilizing finite differences (discussed in the next section) and stored in a matrix. The implementation is relatively straight forward and there are no assumptions about the symmetry of the problem. However, this method has its flaws. If a potential has a singularity, such as the Coulomb potential at zero ($V = -1/r$), special care must be taken to avoid sampling that point. Additionally, the size of the calculation scales like N^3 when the number of grid points in each dimension (N) increases. Therefore, obtaining converged results for large atoms, which require smaller grid spacing to sample the core properly, and high intensities, which require larger box sizes to keep the wavefunction on the grid, becomes computationally impractical. It is, therefore, useful to consider the symmetries of the problem in question to greatly speed up the calculations. Two standard approaches are to utilize cylindrical or spherical coordinates.

The problem of an atom or a linear molecule aligned along a linearly polarized laser is

cylindrically symmetric. Therefore, in this case the using cylindrical coordinates is the natural choice. By choosing the laser polarization (and internuclear axis) along the z -axis, the solution in the angular coordinate ϕ is given by the initial condition and can be given analytically. Thus, one only needs to find a solution in the z and ρ dimensions numerically, reducing the problem to two dimensions. As a result, solutions scale like N^2 which significantly accelerates calculations as compared to a 3D Cartesian code.

However, in our studies we have actually found that spherical codes are often even faster. When written in spherical coordinates, the TDSE for a central potential (such as an atom) can be separated into a radial equation that contains the potential, and an angular portion that is independent of the potential. The angular solution can then be found analytically in the form of spherical harmonics and the radial solution is all that remains. For the hydrogen atom an analytic solution exists. However, in general for a radial potential it is not guaranteed that there is an analytic solution. Therefore, we expand the wavefunction in spherical harmonics and use finite difference to discretize the radial portion. Since the laser field only couples spherical harmonics according to the selection rules $\ell \rightarrow \ell \pm 1$ and $m \rightarrow m, m \pm 1$ depending on the polarization, the number of spherical harmonics needed is rather small (typically $\ell_{max} < 50$) with a weak dependence on laser intensity and wavelength. The result is a code that scales like $N\ell_{max}$ for linear polarization and $N\ell_{max}^2$ for arbitrary polarization. Since ℓ_{max} is small, the code typically scales like N as the pulse intensity, wavelength, or target atom is changed.

3.3.2 Finite difference

To discretize the spatial derivatives, we use finite difference. When using finite differences (FD), derivatives are represented by a set of coefficients called a stencil. The stencil provides the non-zero weights c_i for various sample points of the function. We can then write the second derivative of ψ known at various evenly spaced grid points labeled by n as

$$\frac{d^2}{dx^2}\psi_n = \frac{1}{\Delta x^2} \sum_i c_i \psi_i \quad (3.14)$$

The non-zero c_i coefficients are given in the table below for various orders of accuracy:

Order	c_{n-3}	c_{n-2}	c_{n-1}	c_n	c_{n+1}	c_{n+2}	c_{n+3}
2nd			-1	2	-1		
4th		-1/12	4/3	-5/2	4/3	-1/12	
6th	1/90	-3/20	3/2	-49/18	3/2	-3/20	1/90

Although it is possible to hard code the stencil weights, it becomes quite tedious particularly for high order stencils, non-uniform grids, and near boundaries where off-centered stencils are needed. Therefore in this work we utilize the Fornberg method [19] to obtain the necessary stencil for a particular simulation.

TODO: add brief explanation

For the remainder of this discussion, we will assume that we are using second order derivatives. However, it is straightforward to expand it to higher order derivatives by adding more off-diagonal elements in matrices discussed in this section.

We begin with a 1D wavefunction and later extend to ND wavefunctions. Let us assume that we start with $\psi(x)$ known at various points along the x axis spaced by a grid step of dx . We will label the points by n such that $\psi_n = \psi(x_0 + ndx)$ with x_0 being the smallest x value. Plugging this into Equation 3.14 we get

$$\frac{d^2}{dx^2}\psi_n = \frac{1}{\Delta x^2} (-\psi_{n-1} + 2\psi_n - \psi_{n+1}). \quad (3.15)$$

For the point ψ_{n+1} we can therefore write

$$\frac{d^2}{dx^2}\psi_{n+1} = \frac{1}{\Delta x^2} (-\psi_n + 2\psi_{n+1} - \psi_{n+2}). \quad (3.16)$$

This holds until we reach the other end of the grid. If we consider as boundary condition that $\psi(x_0 - dx) = \psi(x_N + dx) = 0$, then the points at $x_0 - dx$ and $x_N + dx$ can be simply left out of the matrix, which automatically imposes this boundary condition. For higher order stencils, an off centered difference formula is needed such that the boundary condition is only imposed at one

point. The operator becomes a system of linear equations in the form of a matrix:

$$\frac{d^2\psi}{dx^2} = \frac{1}{\Delta x^2} \begin{bmatrix} 2 & -1 & & & \\ -1 & 2 & -1 & & \\ & \ddots & \ddots & \ddots & \\ & & -1 & 2 & -1 \\ & & & -1 & 2 \end{bmatrix} \begin{bmatrix} \psi_0 \\ \psi_1 \\ \vdots \\ \psi_{N-1} \\ \psi_N \end{bmatrix} \quad (3.17)$$

One uses a tensor product to produce the two and three dimensional versions of the operator.

3.3.3 Radial basis functions

A disadvantage of grid based methods, such as 3D Cartesian codes, is the structure of the grid. The required structured grids for FD do not give the freedom to refine the sampling in points of interest, such as near the nucleus, while sparsely sampling at large radii, due to the Kronecker product. Radial basis functions (RBF), on the other hand, is a meshless method that allows for sampling points, called nodes, to be placed anywhere [20]. The lack of required structure significantly reduce the number of points required to approximate the wavefunction. In this work the RBF method described below was applied to quickly obtain bound and continuum states. However, more work will be needed to allow for time propagation of the wavefunction in a laser field.

The RBF method starts with a set of N unique points in space called nodes that discretize the problem space. A stencil of size $n < N$ is then made for each node via its $n - 1$ closest neighbors by using a k -nearest neighbors algorithm. For a RBF wavefunction $\phi(r)$, one defines the matrix

$$\mathbf{A} = \begin{bmatrix} \phi(|\mathbf{x}_1 - \mathbf{x}_1|) & \phi(|\mathbf{x}_2 - \mathbf{x}_1|) & \cdots & \phi(|\mathbf{x}_n - \mathbf{x}_1|) \\ \phi(|\mathbf{x}_1 - \mathbf{x}_2|) & \phi(|\mathbf{x}_2 - \mathbf{x}_2|) & \cdots & \phi(|\mathbf{x}_n - \mathbf{x}_2|) \\ \vdots & \vdots & & \vdots \\ \phi(|\mathbf{x}_1 - \mathbf{x}_n|) & \phi(|\mathbf{x}_2 - \mathbf{x}_n|) & \cdots & \phi(|\mathbf{x}_n - \mathbf{x}_n|) \end{bmatrix}, \quad (3.18)$$

where \mathbf{x}_j is the coordinates of a node. It is then possible to calculate the weights ω_j of an operator

\mathcal{L} evaluated at some point x_c by solving

$$\begin{bmatrix}
 & & & | & 1 & x_1 & y_1 & z_1 & \cdots & e^{-\alpha r_1} \\
 & \mathbf{A} & & | & \vdots & \vdots & \vdots & \vdots & & \vdots \\
 & & & | & 1 & x_n & y_n & z_n & \cdots & e^{-\alpha r_n} \\
 - & - & - & + & - & - & - & - & - & - \\
 1 & \cdots & 1 & | & & & & & & \\
 x_1 & \cdots & x_n & | & & & & & & \\
 y_1 & \cdots & y_n & | & & & 0 & & & \\
 z_1 & \cdots & z_n & | & & & & & & \\
 \vdots & & \vdots & | & & & & & & \\
 e^{-\alpha r_1} & \cdots & e^{-\alpha r_n} & | & & & & & &
 \end{bmatrix}
 \begin{bmatrix}
 \omega_0 \\
 \vdots \\
 \omega_n \\
 - \\
 \omega_{n+1} \\
 \omega_{n+2} \\
 \omega_{n+3} \\
 \omega_{n+4} \\
 \vdots \\
 \omega_{n+m}
 \end{bmatrix}
 =
 \begin{bmatrix}
 \mathcal{L}\phi(|\mathbf{x} - \mathbf{x}_1|)|_{\mathbf{x}=\mathbf{x}_c} \\
 \vdots \\
 \mathcal{L}\phi(|\mathbf{x} - \mathbf{x}_n|)|_{\mathbf{x}=\mathbf{x}_c} \\
 - \\
 \mathcal{L}1|_{\mathbf{x}=\mathbf{x}_c} \\
 \mathcal{L}x|_{\mathbf{x}=\mathbf{x}_c} \\
 \mathcal{L}y|_{\mathbf{x}=\mathbf{x}_c} \\
 \mathcal{L}z|_{\mathbf{x}=\mathbf{x}_c} \\
 \vdots \\
 \mathcal{L}e^{-\alpha r}|_{\mathbf{x}=\mathbf{x}_c}
 \end{bmatrix}. \quad (3.19)$$

The matrix \mathbf{A} imposes the RBF restrictions while the additional rows and columns allow for polynomials up to some degree $(1, x, y, z, x^2, xy, \dots)$ to be attached, improving the order of accuracy for the stencil. We can also attach other functions such as a Slater type orbital¹ ($e^{-\alpha r}$) to treat the discontinuity in the hydrogen atom wavefunction at $r = 0$. The weights ω_j for $j = 1, \dots, n$ are used as the matrix elements in the operator matrix and weights with $j > n$ are discarded. When solving a PDE, it is often useful to take $x_c = x_1$ for each stencil such that the weights can be reused during time propagation. However, one can freely choose x_c allowing for the node placements to adapt to the PDE solution over time.

For the solution to the hydrogen atom we use 7th order polyharmonic spline functions ($\phi(r) = r^7$). The node set is then chosen to emulate the standard spherical codes that are used. To do this, we discretize the radius at values $r_j = (j + dr)/2$ for $j = 0, \dots, j_{max}$. A maximal determinate (MD) node set [64] for each radius is added to the total RBF node set. The MD node sets simulate the use of spherical harmonics, which strongly reduces the required number of nodes for the problem at hand.

¹ The method was developed in collaboration with Dylan Abrahamsen (Department of Applied Mathematics (University of Colorado Boulder)).

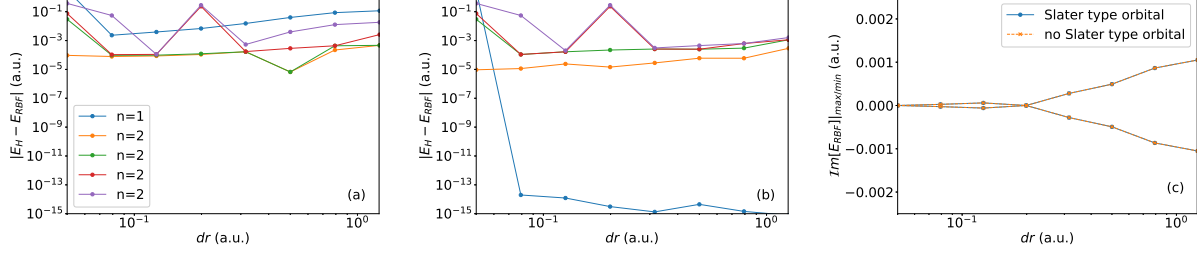


Figure 3.1: Panels a (b) show the convergence of the lowest energy bound states in Hydrogen without (with) an attached Slater type orbital for various radial spacing (dr). Panel c shows the minimum and maximum imaginary part of the calculated bound state energies.

Choosing a fixed order of MD nodes for all values of r leads to two major issues. At small r , the nodes on each shell are much closer together as compared to the distance to the neighboring shells leading to the obstacle that stencils do not couple in the radial direction. This can be avoided by reducing the order of the MD node sets at small r so that the radial grid spacing (dr) is less than or equal to the average distance between neighboring MD nodes within a shell. The order of the MD node set then increases as r increases to the set maximum order. At large r , a similar issue occurs, where only nodes at fixed angles (θ and ϕ) with varying radii are chosen for a given stencil. To avoid this, each MD node set is quasi randomly rotated before being added to the total node set.

A final implementation issue is caused when attaching Slater type orbitals ($e^{-\alpha r}$) to the stencil. Since $e^{-\alpha r}$ becomes small quickly for increasing r , it can have variations below machine precision in a given stencil. The result is a linear dependence with the constant term producing poor stencils. To remedy this issue, $e^{-\alpha r}$ is only attached for stencils centered at radii with $e^{-\alpha r_1} > 10^{-10}$.

Convergence of the lowest 5 bound states using the RBF code are shown in Fig. 3.1. Results were obtained on mesh with a 30 a.u. radial extend, 8th order MD node set, 7th order PHS RBF, attached polynomials up to 3rd order, and a stencil size of 54 nodes. Panel a and b shows the error in the real part of the states energy without and with a Slater type orbital e^{-r} being attached. The addition for the Slater type orbital give machine precision for the ground state (blue line) and improves the 2s (orange line) energy until nonphysical states appear with $dr < 0.1$. The 2p states

see little benefit from the Slater type orbital.

Fig. 3.1c shows the maximum and minimum imaginary part of the energy of the 5 calculated states. The splitting occurs for the states with $m \neq 0$ when meshes other than a Cartesian lattice are used. The states with $\mathcal{Im}[E] < 0$ lead to unstable time propagation for the Crank-Nicolson method used in this work. Further work on mesh generation, Hyperviscoisty, and/or time propagation methods will be needed to study time dependent problems with the RBF.

3.3.4 Numerical integration

For the finite difference integration, either the midpoint or trapezoid rule are used for numerical integration. For both methods the integration is performed by

$$\int_x f(x')dx' = \sum_{i=1}^n c_i f(x_i) \quad (3.20)$$

where $f(x_i)$ is the value of the function at x_i and x is the integration interval. The midpoint rule is used if the grid is placed at half grid points on the interval (i.e. $x_i = (2i+1)dx/3$ for $i = 0, 1, 2, \dots, n$). In this case $c_i = 1/dx$ for all grid points. For the trapezoid rule the grid points sample the ends of the integration range resulting in $c_0 = c_n = 1/2dx$ and $c_i = 1/dx$ for $i = 1, \dots, n-1$.

In the case of the RBF code, the MD node set comes with a provided integration weight for the angular integration and the radial integration is done via the midpoint rule. For the spherical code, the angular integration is done analytically since spherical harmonics are orthonormal.

3.3.5 Boundary conditions

The wavefunction at large r must decay to zero for it to be normalizable. Therefore, we set the wavefunction to zero at r_{max} and increase the value of r_{max} until a converged result is obtained (Sec. 3.3.9). Exterior complex scaling (ECS), which is discussed in the next paragraph, insures that the wavefunction decays prior to hitting the boundary. For the Cartesian code, this is the only boundary conditions needed. For the cylindrical and spherical codes, another boundary condition at $r = 0$ is required. The cylindrical code the grid is chosen such that the grid points are given by

$$\begin{array}{c}
c_{n-2} \quad c_{n-1} \quad \left[\begin{array}{ccccc} c_n & c_{n+1} & c_{n+2} & & \\ & c_{n-1} & c_n & c_{n+1} & c_{n+2} \\ & & c_{n-2} & c_{n-1} & c_n & c_{n+1} & c_{n+2} \\ & & & \ddots & \ddots & \ddots & \ddots & \ddots \end{array} \right] \quad (a)
\end{array}
\qquad
\begin{array}{c}
c_{n-1} \quad \left[\begin{array}{cccc} c_n & c_{n+1} & c_{n+2} & c_{n+3} \\ & c_{n-1} & c_n & c_{n+1} & c_{n+2} \\ & & c_{n-2} & c_{n-1} & c_n & c_{n+1} & c_{n+2} \\ & & & \ddots & \ddots & \ddots & \ddots & \ddots \end{array} \right] \quad (b)
\end{array}$$

Figure 3.2: The finite difference stencil near the edge of the grid. Panel (a) shows how in the fourth order finite difference the stencil extends beyond the grid leading to a boundary condition being imposed at two points. Panel (b) shows the non-centered 4th order stencil that enforces a single boundary condition.

$x_j = (2j + 1)dx/2$ with $j = 0, 1, 2, \dots, n$ and the boundary condition of $\psi(-x) = \psi(x)$ is used. In the spherical code, however, $x_j = jdx$ with $j = 1, 2, 3, \dots, n$ and the boundary condition $\psi(0) = 0$ is used. To enforce a boundary condition a “ghost node” is implemented. The ghost node is a grid point that falls outside of the grid. If the ghost node is set to zero, the coefficient is left off the matrix, and the boundary condition is met. If the stencil would be extending beyond the grid by more than one point, such as in 4th order finite difference, the stencil is shifted so that only one point is beyond the grid and it retains the same width (see Fig. 3.2). For the cylindrical case, the ghost node is taken at $\psi(-dx/2)$. Since $\psi(-x) = \psi(x)$, the stencil coefficient at $\psi(-dx/2)$ is added to the coefficient for $\psi(dx/2)$ which imposes the boundary condition.

To absorb any outgoing wave packets, we utilize an exterior complex scaling method (ECS, [27]) on the outer portion of the grid. This is equivalent to changing the spatial step used in finite difference from $x_{n+1} = x_n + dx$ to $x_{n+1} = x_n + e^{i\eta}dx$. In test calculations we have found that $\eta = \pi/4.0$ works well. The result is an exponential decay of the wavefunction in the absorbing region. Obtaining the finite difference weights in the transition and ECS region is done by implementing the Fornberg method [19] using complex numbers.

3.3.6 Bound state calculations

The bound states of the system are simply the eigenstates of the Hamiltonian with energies less than zero. Therefore they satisfy the equation

$$\hat{H}\phi_i = E_i\phi_i \quad (3.21)$$

where \hat{H} is the Hamiltonian, E_i is the energy, and ϕ_i is the bound state assuming $E_i < 0$. To solve for the bound states, we use the Krylov-Schur method that is implemented in the SLEPc library **CITATION NEEDED**. When obtained using SLEPc, the states have a random complex phase associated with them. The phase is physically irrelevant unless one is creating a superposition or comparing the phase of populations between calculations that uses different bound state sets such as a TDSE and PT result. To avoid issues, it is best to use a single bound state calculation for each project. The populations obtained via projections onto excited bound states at the end of a simulation are, for example, useful to analyze and verify selection rules for a given laser polarization.

The coordinate system used for bound state calculations will control which states are generated. For spherical calculations, each ℓ block can be calculated independently and the results are independent of m . Likewise, results of cylindrical 2D calculations are obtained for fixed m quantum number. Finally, Cartesian 3D calculations will provide all n , ℓ , and m states in one calculation with the states being oriented at a random angle.

3.3.7 Continuum states

The continuum has states at all levels with energy larger than zero in the physical problem. However, when we solve the TDSE numerically, due to the finite extension of the grid the continuum is represented via a discrete set of states. For example, in spherical coordinates the TDSE solution on the grid requires $\psi(0) = \psi(r_{max}) = 0$ (for the radial coordinate). The same boundary condition is the same as for an infinite square well, however with a bottom in the shape of $V(r)$. The continuum states are therefore a distorted solution to the infinite square well problem. We can obtain these states by the same method as used in the bound state calculations providing a discrete

set of energies that represent the continuum. This method is used for the numerical PT solution discussed in Sec. 3.2.

When calculating a photoelectron (energy or angular) spectrum, however, it is advantageous to be able to select the energy of the continuum wave. For this case, we utilize the shooting method to obtain a continuum wave at a given energy. The method is given via an ODE which one solves it as follows. The wavefunction at $r = 0$ is set to zero by the boundary condition. The first point at $r_0 = dr$ is set to an arbitrary value (in this case 1) giving

$$\phi_{kl}(r_0) = 1. \quad (3.22)$$

with $k = \sqrt{2E}$. The second point is then obtained by

$$\phi_{kl}(r_1) = \phi_{kl}(r_0) \left(dr^2 \left[\frac{\ell(\ell+1)}{r^2} + 2V(r_0) - 2E \right] + 2 \right). \quad (3.23)$$

Then every additional point can be found by

$$\phi_{kl}(r_{i+1}) = \phi_{kl}(r_i) \left(dr^2 \left[\frac{\ell(\ell+1)}{r^2} + 2V(r_i) - 2E \right] + 2 \right) - \phi_{kl}(r_{i-1}). \quad (3.24)$$

Now that the wavefunction has been obtained, we match the asymptotic solution to that for a hydrogen-like atom

$$\phi_{kl}(r \gg 1) \rightarrow \sin \left[kr - \frac{l\pi}{2} + \frac{Z}{k} \ln(2kr) + \delta_{kl} \right]. \quad (3.25)$$

The continuum state oscillates between -1 and 1 at $r \gg 1$ leading to a normalization of

$$A = \left[\frac{1}{\sqrt{|\phi_{kl}(r)|^2 + \left| \frac{\phi'_{kl}(r)}{(k + \frac{Z}{kr})} \right|^2}} \right]_{r=r_{max}}. \quad (3.26)$$

Finally, we extract the phase shift δ_{kl} by

$$\delta_{kl} = \left[\text{Arg} \left(\frac{i\phi_{kl}(r) + \frac{\phi'_{kl}(r)}{(k + \frac{Z}{kr})}}{(2kr)^{iZ/k}} \right) - kr + \frac{l\pi}{2} \right]_{r=r_{max}}. \quad (3.27)$$

This continuum state can then be used to obtain the photoelectron spectrum by

$$P(k, \theta, \phi) \propto \left| \sum_{l,m} Y_{l,m}(\theta, \phi) \int e^{-i\delta_{kl}} (i)^l \phi_{kl}(r)^* \psi(r, t) dr \right|^2. \quad (3.28)$$

3.3.8 Time propagation

Time propagation is often performed using the split-operator method where the Hamiltonian (\hat{H}) is split into its spatial dimensions, e.g. along (z) and perpendicular (ρ) to the polarization direction of a linearly polarized laser. Similarly, the problem can be split along x , y , and z for an arbitrary laser polarization. The resulting propagation scheme is given by

$$\psi(\mathbf{r}, t + \Delta t) \approx e^{-i\hat{H}_\rho \frac{\Delta t}{2}} e^{-i\hat{H}_z(t)\Delta t} e^{-i\hat{H}_\rho \frac{\Delta t}{2}} \psi(\mathbf{r}, t), \quad (3.29)$$

where

$$e^{-i\hat{H}\Delta t} \approx \frac{1 - i\frac{\Delta t}{2}\hat{H}}{1 + i\frac{\Delta t}{2}\hat{H}}. \quad (3.30)$$

This produces a set of tridiagonal matrices which can be solved with $\mathcal{O}(\mathcal{N})$ operations and $\mathcal{O}(\mathcal{N})$ memory. However, parallelization of such a method on a modern supercomputer with distributed memory can be cumbersome, requiring multiple all-to-all Message Passing Interface (MPI) messages during each time step which strongly reduces its scalability.

Instead, we avoid splitting the Hamiltonian and propagate the total Hamiltonian in time using a second order Crank-Nicolson scheme where

$$\psi(\mathbf{r}, t + \Delta t) \approx e^{-i\hat{H}\Delta t} \psi(\mathbf{r}, t). \quad (3.31)$$

We note that the Crank-Nicolson method is not tridiagonal (due to a tensor product) and a direct solution would require $\mathcal{O}(\mathcal{N}^3)$ operations and $\mathcal{O}(\mathcal{N}^2)$ memory which is significantly more than in the split operator method. However, the system of equations in the full Crank-Nicolson method is sparse and iterative methods can be used to vastly accelerate the time propagation. We utilize the Generalized Minimal Residual Method (GMRES), implemented in PETSc, which solves the sparse system of linear equations in $\mathcal{O}(\mathcal{N} \log(\mathcal{N}))$ operations and $\mathcal{O}(\mathcal{N})$ memory. The PETSc library makes it straightforward to parallelize the Crank-Nicolson method on modern supercomputers with distributed memory. On a local supercomputer (Summit, CU Boulder), we achieved super-linear scaling up to 3,000+ cores (see Fig. 3.4) allowing us to complete simulations in a matter of hours that would take weeks running on a high-end workstation.

dx	Z=1	Z=2	Z=3	Z=4	Z=5
4.000e-01	5.995e-03	6.217e-02	1.590e-01	2.568e-01	3.416e-01
2.000e-01	3.035e-04	5.995e-03	2.612e-02	6.217e-02	1.086e-01
1.000e-01	1.041e-05	3.035e-04	1.841e-03	5.995e-03	1.392e-02
5.000e-02	2.225e-07	1.041e-05	7.810e-05	3.035e-04	8.331e-04
2.500e-02	-2.663e-09	2.225e-07	2.290e-06	1.041e-05	3.204e-05
1.250e-02	-7.101e-10	-2.672e-09	2.992e-08	2.225e-07	8.341e-07

Table 3.1: The relative error of the ground state energy for a hydrogen-like atom with a nuclear charge Z . A grid spacing around 0.1 produces well converged results for $Z = 1$. Excited states have lower relative error.

3.3.9 Convergence studies

Numerical solutions to the TDSE require a convergence study to ensure that the final results are reliable. One does this by varying a free parameter, such as grid spacing, spherical harmonic expansions, time step, etc, until the observable in question changes within some tolerance. It is possible to use an error calculation and reduce it until a numerical tolerance is met. However, graphical convergence, when 2 lines plotted on top of each other are indistinguishable, is often a more practical convergence criteria. In Table 3.1 we show the error of the ground state energies of a hydrogen-like atom with difference charge (Z) converges with grid spacing when using 4th order finite difference.

For a fixed target, it is advantageous to use the highest order finite difference that is stable. Fig. 3.3 shows the convergence of the $1s$, $2s$, and $3s$ energy levels of the hydrogen atom using 2^{nd} through 20^{th} order FD. The slope of the convergence for each curve matches the order of the method. 20^{th} order FD achieves a converged result with the largest grid spacing leading to a shorter calculation. It is therefore advantageous for bound state calculations. However, the Hamiltonian for higher order methods become increasingly non-Hermitian near the boundaries leading to unstable time propagation for 6^{th} or higher order FD. Therefore, we use 4^{th} order for the vast majority of calculations that we have performed in this work.

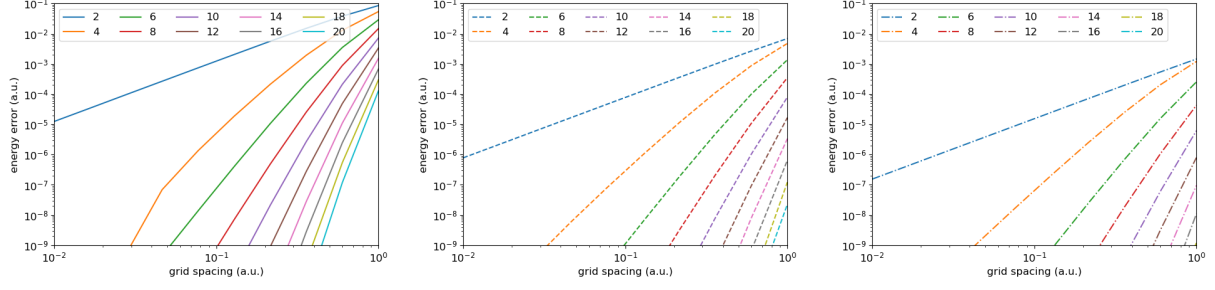


Figure 3.3: Convergence with respect to grid spacing for various orders of FD for the $1s$ (a), $2s$ (b), and $3s$ (c) states in hydrogen atom.

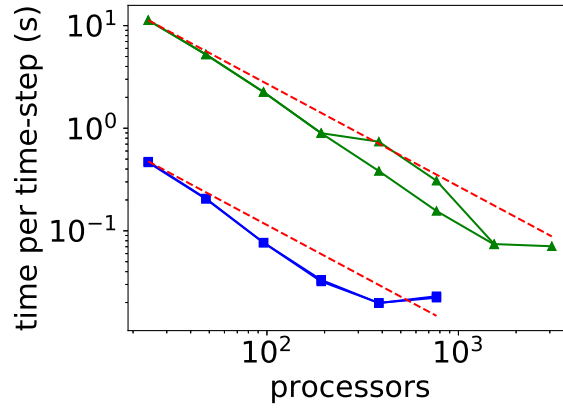


Figure 3.4: Scaling results for present Crank-Nicolson method. Two runs each for calculations with 1 million (blue with squares) and 15 million grid points (green with triangles) have been performed. Note that the scaling improves with increasing number of grid points.

3.3.10 Parallel Computing

Many simulations can be performed on a laptop or small desktop, however, the largest calculations, such as those done in Cartesian coordinates or utilizing bi-circular laser polarizations, benefit from supercomputing resources. Since the code is implemented utilizing the PETSc library and through the use of MPI, we are able to take advantage of the distributed memory of a modern supercomputer. Linear scaling, when the computational time is cut in half when twice as many processors are used, is often the benchmark for code scaling. Our code obtains super-linear (better than linear) scaling on the Summit supercomputer up to 3,000+ processors (see Fig. 3.4). This is

Atom	z	Z_c	c	a_1	b_1	a_2	b_2
H	1	-	-	-	-	-	-
He	1	1	2.0329	0.3953	6.1805	-	-
Ne	1	9	0.8870	-9.9286	1.3746	-5.9950	3.7963

Table 3.2: Coefficients of SAE potentials in Eq. 3.33 for hydrogen, helium, and neon from [62].

possible due to the increased size of cache memory as the number of CPUs increases. This allows for calculations that would take a month on a desktop to be completed in a few hours on a supercomputer. Additionally, the supercomputing systems come with a large increase in the available RAM (often on the order of terabytes) significantly reducing the memory limitations on calculation size.

3.4 Single active electron potentials

For many atoms, full treatment of Eq. 3.2 is impractical if not impossible. Since in many ultrafast laser-atom interactions primarily a single valence electron is involved, in this cases it becomes advantageous to treat only the single active electron in the potential produced by freezing the remaining $N - 1$ electrons in their ground state reducing the problem from 3^N -dimensions down to 3-dimension. The resulting Hamiltonian becomes

$$\hat{H} = -\frac{\mathbf{p}^2}{2} + V_{SAE}(\mathbf{r}) + V_{las}(t) \quad (3.32)$$

where $V_{las}(t)$ is the laser operator and $V_{SAE}(\mathbf{r})$ is the SAE potential. The SAE potentials utilized in this work take the form [62]

$$V_{SAE}(\mathbf{r}) = -\frac{z}{r} - \frac{Z_c e^{-cr}}{r} - \sum_n a_n e^{-b_n r}. \quad (3.33)$$

The coefficients are obtained by fitting to a potential obtained through density functional theory (DFT). In tab. 3.2 we show the coefficients for SAE potentials used in this thesis.

3.5 Observables

The wavefunction, as numerical solution of our calculations, is not experimentally observable, it is therefore necessary to extract experimentally relevant information via observables. For a given observable \hat{O} , the expectation value is obtained by calculating $\langle \Psi | \hat{O} | \Psi \rangle$. In this work we have studied high order harmonic generation (HHG) spectra, ionization, bound state populations, and photo ionization (energy and angular) distributions.

HHG spectra are obtained by first calculating the dipole acceleration using the Ehrenfest theorem

$$\hat{a}_j = \frac{\partial V(\mathbf{r})}{\partial j} \quad (3.34)$$

where $j \in x, y, z$ are the Cartesian coordinates. For the hydrogen atom, $\hat{a}_j = j/r^3$ where r is the distance from the nucleus. Then the HHG spectrum is obtained by taking a Fourier transform such that

$$\hat{O}_{HHG}(\omega)_j = \left| \int_{-\infty}^{\infty} e^{-i2\pi\omega t} \langle \Psi(t) | \hat{a}_j | \Psi(t) \rangle dt \right|^2 \quad (3.35)$$

Bound state populations are obtained using

$$P_{\phi_i} = |\langle \phi_i | \Psi \rangle|^2 \quad (3.36)$$

where ϕ_i is the field free bound state and Ψ is the wavefunction.

At the beginning of each simulation, the wavefunction is normalized to 1 such that

$$\langle \Psi(t_0) | \Psi(t_0) \rangle = 1 \quad (3.37)$$

Ionization can then be calculated in two manners. First is by time propagating after the pulse and allowing the ionized wave function to be absorbed by the ECS. Ionization is then obtained by taking

$$P_{ion} = 1 - |\langle \Psi | \Psi \rangle|^2 \quad (3.38)$$

since $\langle \Psi(t_0) | \Psi(t_0) \rangle = 1$. This method is slow to converge and susceptible to numerical round off

error due to extended time propagation. The preferred method for calculating ionization is

$$P_{ion} = 1 - \sum_i |\langle \phi_i | \Psi \rangle|^2 \quad (3.39)$$

where ϕ_i is a bound state and the sum over i includes all states the grid supports with a real part of the energy that is less than zero. Therefore the ionization probability can be taken at the end of the pulse reducing the computational expense and numerical error.

The photoelectron spectrum (energy and angular) can be obtained at the end of the pulse by calculating

$$P(k, \theta, \phi) \propto \left| \sum_{l,m} Y_{l,m}(\theta, \phi) \int e^{-i\delta_{kl}} (i)^l \phi_{kl}(r)^* \psi(r, t) dr \right|^2 \quad (3.40)$$

where $\phi_{kl}(r)$ is a continuum wave, δ_{kl} is a phase shift, and $Y_{l,m}(\theta, \phi)$ is a spherical harmonic. The angular distribution is obtained by plotting the angular dependence (θ and ϕ) for a given energy. The energy distribution is obtained by integrating over θ and ϕ . See Sec 3.3.7 for details on obtaining $\phi_{kl}(r)$ and δ_{kl} .

3.6 Laser pulses

In order to satisfy Maxwell's equations, the electric field of a laser pulse must integrate to zero. It is therefore convenient to set the vector potential $A(t)$ such that

$$A(t) = \frac{cE_0}{\omega_A} f(t) \cos(\omega_A t + \phi_A) \quad (3.41)$$

where $E_0 = \sqrt{I}$ is the peak electric field amplitude with I is the peak intensity, c is the speed of light, ω_A is the central frequency of the vector potential, ϕ_A is the carrier-to-envelope phase, and $f(t)$ is the envelope function that starts and ends at zero. We often consider $f(t)$ to be a Gaussian or sine squared function. The electric field can then be obtained via

$$\begin{aligned} E(t) &= -\frac{1}{c} \frac{\partial}{\partial t} A(t) \\ &= E_0 f(t) \sin(\omega_A t + \phi_A) - \frac{E_0}{\omega_A} \frac{\partial f(t)}{\partial t} \cos(\omega_A t + \phi_A). \end{aligned} \quad (3.42)$$

where the second term forces the time integral of the electric field to be zero and is only large when the envelope varies quickly over a single optical cycle. This is the case in few cycle pulses and those that turn on or off quickly.

3.6.1 Frequency shift²

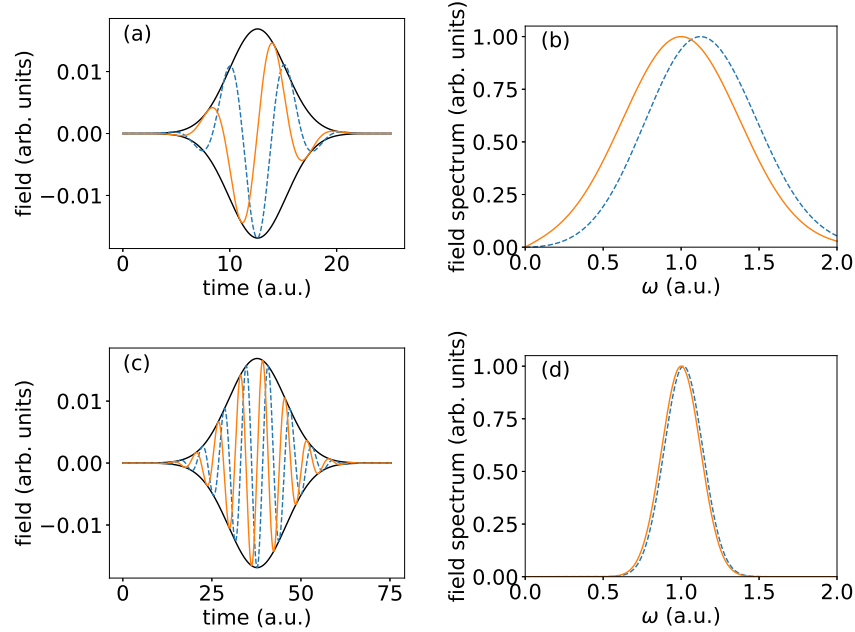


Figure 3.5: Temporal (left) and spectral (right) distributions of vector potential (solid lines) and electric field (dashed line) for pulses with FWHM of 1 cycle (top), and 3 cycles (bottom) at central frequency $\omega_A = 1.0$ a.u. of the vector potential. Also shown is the Gaussian envelope of the vector potential.

As the pulse length decreases, the central frequency (defined by the peak of the frequency spectrum) of the vector potential and electric fields differ. In Fig. 3.5 the dashed blue lines show the electric field and the orange solid lines show the vector potential for a Gaussian pulse with a pulse duration of 1 cycle FWHM (top) and 4 cycle FWHM (bottom). The time domain (right) looks similar, up to the expected $\pi/2$ phase shift, but the frequency spectrum (right) differ significantly for the 1 cycle FWHM pulses. By utilizing TDSE solutions, it is possible to show that the central frequency of the electric field is the relevant frequency in both length and velocity gauge calculations

² The content of this subsection has been also published in J. Venzke et al. PRA **98**, 063409 (2018)

[75]. It is, therefore, important to correct the central frequency used in the vector potential when the pulse length is short. An approximate correction is given by

$$\frac{\omega_E}{\omega_A} \approx \frac{1 + \sqrt{1 + 4(\pi N)^{-2}}}{2}. \quad (3.43)$$

Here

$$N \equiv \frac{\omega_A}{\pi} \sqrt{\frac{\int_{-\infty}^{\infty} (t - t_0)^2 f(t) dt}{\int_{-\infty}^{\infty} f(t) dt}}. \quad (3.44)$$

is the number of cycles within one standard deviation to either side of the pulse center, with

$$t_0 \equiv \frac{\int_{-\infty}^{\infty} t f(t) dt}{\int_{-\infty}^{\infty} f(t) dt}. \quad (3.45)$$

This correction is sufficient for most pulse shapes, however, correction terms can be found in [75].

HERE

Few-cycle laser pulses are used in many interesting strong-field applications (for reviews, see e.g., [?, ?, ?, ?, ?, ?]): For example, high-order harmonics and (isolated) attosecond pulses are generated, ultrafast atomic and molecular dynamics as well as charge transfer and exciton dynamics can be induced and time resolved, molecular structure can be imaged on ultrashort time scales, or chemical reactions may be controlled. Therefore, light sources generating ultrashort intense laser pulses in different regions of the spectrum, at extreme ultraviolet [?], ultraviolet [?], optical [?], near-infrared [?, ?, ?] and infrared wavelengths [?, ?, ?], have been developed over the past decades. The simulation of the time-dependent response of matter to a few-cycle pulse, e.g. via the numerical solution of the corresponding time-dependent Schrödinger equation (TDSE), can however crucially depend on the definition of the electric field $E(t)$ used. To achieve quantitative agreement between theory and experiment, the potential issues present in both numerical calculations and experiment must be well understood and minimized.

As pointed out by Chelkowski and Bandrauk [?], the representation of $E(t)$ via an envelope function times a trigonometric function may lead to a non-vanishing potential $A(t)$ at the end of the pulse. This inconsistency can be resolved by first defining the magnitude of the vector potential

$A(t)$ as (we use Hartree atomic units: $e = m_e = \hbar = 1$) [?]:

$$A(t) = \frac{cE_0}{\omega_A} f(t) \cos(\omega_A t + \phi_A), \quad (3.46)$$

where f , ω_A , c , E_0 and ϕ_A are the envelope function, central frequency, speed of light, peak electric field amplitude, and carrier envelope phase of the vector potential, respectively. The prefactors ensure that the peak intensity of the laser field is $I = \frac{c}{8\pi} E_0^2$. The magnitude of the electric field is then obtained via the derivative:

The expression for the electric field, Eq. (3.42), includes a term that depends on the time derivative of f and, hence, may have significant effects in the case of few-cycle pulses. As we will show below, a direct implication is that the central frequency of the electric field spectrum, ω_E , is not equal to ω_A . The frequency shift $|\omega_E - \omega_A|$ is a purely electromagnetic effect that is directly related to the definition of the electric field via the vector potential given in Eq. (3.42). For long pulses, the frequency shift is small, but it increases as pulse duration decreases. Note, that in experiment typically the central laser frequency of the electric field ω_E is measured and reported, while in numerical calculations it is useful to define the laser pulse via the vector potential and the related central frequency ω_A . It is therefore important to study what impact, if any, the difference between the central frequencies has on numerical calculations, or on the interpretation of theoretical results.

By solving the time-dependent Schrödinger equation both numerically as well as within perturbation theory, we show below that theoretical results obtained for linear processes—such as excitation and ionization—involving few-cycle pulses with the same value for the central frequencies ω_A and ω_E do not coincide. Furthermore, we find that the frequency shift is also noticeable for nonlinear processes, such as two-photon excitation and high-order harmonic generation, and it scales with the number of photons involved. Our results also demonstrate that it is the central frequency of the electric field ω_E that is the physical relevant quantity for the interpretation of laser driven quantum mechanical processes. Therefore, the frequency shift should be taken into account when setting the central frequency ω_A of the vector potential in a numerical calculation or, more

Name	Envelope Function $f(t)$	N/N_{FWHM}	γ_2
Gaussian	$e^{-(t/T)^2}$	0.849	0
Cos^2	$\begin{cases} \cos^2(\frac{t}{T}) & -\frac{\pi}{2} \leq \frac{t}{T} \leq \frac{\pi}{2} \\ 0 & \text{otherwise} \end{cases}$	0.723	-0.594
Cos^4	$\begin{cases} \cos^4(\frac{t}{T}) & -\frac{\pi}{2} \leq \frac{t}{T} \leq \frac{\pi}{2} \\ 0 & \text{otherwise} \end{cases}$	0.777	-0.381
Sech	$\text{sech}(\frac{t}{T})$	1.19	2.00

Table 3.3: Several common analytic pulse envelopes. The conversion factor between N , as defined in Eq. (3.44) (number of cycles within one standard deviation to either side of the maximum), and the more typical N_{FWHM} (number of cycles in the full-width half-maximum of the electric field) is given. The last column shows the excess kurtosis γ_2 , defined in Eq. (3.48), which is independent of the pulse duration T .

generally, a theoretical analysis.

The frequency shift due to the difference in central frequencies is illustrated in Fig. 3.5, where the vector potential A and the electric field E , obtained from Eqs. (3.46) and (3.42) for a Gaussian envelope $f(t)$, are compared in both the time and frequency domain. While the temporal behavior is satisfactory, the spectral distributions reveal different central frequencies. We define the central frequency ω_A (ω_E) as the location of the maximum in the spectral density $|\tilde{A}(\omega)|$ ($|\tilde{E}(\omega)|$). The discrepancy is much greater for the 1-cycle full-width at half-max (FWHM) pulse (top), than for the 3-cycle FWHM pulse (bottom).

For the further analysis, we note that in order for the central frequencies to be well-defined and consistent with the definition of ω_A in Eq. (3.46), we make several assumptions about the envelope $f(t)$:

- $f(t)$ is nonnegative and continuously differentiable,
- $f(t)$ falls off at least exponentially for large $|t|$,
- $f(t)$ contains no appreciable Fourier components larger than ω_A .

These assumptions could be relaxed significantly, but they are sufficient for the present discussion and all practical purposes. The ratio of the central frequencies is given by the leading terms of an

expansion in $1/N$ as (see Appendix ??): Here is the number of cycles within one standard deviation to either side of the pulse center, with

$$t_0 \equiv \frac{\int_{-\infty}^{\infty} t f(t) dt}{\int_{-\infty}^{\infty} f(t) dt}, \quad (3.47)$$

and lastly γ_2 is the excess kurtosis of the envelope

$$\gamma_2 \equiv \frac{\left[\int_{-\infty}^{\infty} (t - t_0)^4 f(t) dt \right] \left[\int_{-\infty}^{\infty} f(t) dt \right]}{\left[\int_{-\infty}^{\infty} (t - t_0)^2 f(t) dt \right]^2} - 3. \quad (3.48)$$

Note that N is proportional to the more typical N_{FWHM} (number of cycles in the FWHM of $f(t)$), but the ratio N/N_{FWHM} depends on the shape of the envelope (c.f., Table 3.3).

Eq. (3.43) indicates that the ratio ω_E/ω_A depends on the number of cycles and the pulse shape, but it is independent of peak intensity, carrier envelope phase, ellipticity, and ω_A itself. In fact, the first term of the expansion, Eq. (3.43), is a very accurate estimate even for single cycle pulses, showing that the shift is nearly independent of pulse shape. This can be seen from the comparison between the predictions based on Eq. (3.43) with the exact frequency shift for a variety of pulse shapes in Fig. 3.6. The exact shift was calculated by numerically maximizing the analytic expressions for $|\tilde{E}(\omega)|$. The slight dependence on pulse shape is visible in the inset; the differences are described well by the correction term in Eq. (3.43), which involves the excess kurtosis γ_2 .

In the next section, we demonstrate that ω_E is the physically observable and relevant central frequency. Therefore, when modeling the interaction with a pulse using Eqs. (3.46) and (3.42), one should determine ω_A such that it corresponds to the correct ω_E . There are two different methods to do this. The first one is to specify N , and use Eq. (3.43) to obtain ω_A . However since N depends implicitly on ω_A through Eq. (3.44), the envelope $f(t)$ must be stretched in time by the same factor such that N remains unchanged. The second method is to specify $f(t)$ instead of N . In that case, substituting Eq. (3.44) into Eq. (3.43) and solving for ω_A yields

$$\omega_A \approx \omega_E - \frac{\int_{-\infty}^{\infty} f(t) dt}{\omega_E \int_{-\infty}^{\infty} (t - t_0)^2 f(t) dt}. \quad (3.49)$$

Greater accuracy could be obtained in either case by including the correction term in Eq. (3.43); however, the results in Fig. 3.6 show that this is in general not necessary.

In this section we present results of numerical calculations and first-order perturbation theory which exemplify effects of the frequency shift on observables related to excitation, ionization and high harmonic generation induced by short laser pulses. The frequency shifts obtain using first-order perturbation theory and numerical calculations agree well with our analytical predictions shown in Section ?? and derived in Appendix ?. To this end, we solved the 3D one-electron time-dependent Schrödinger equation (TDSE) in velocity gauge:

$$i\frac{\partial}{\partial t}\psi(\mathbf{r},t) = \left[\frac{\mathbf{p}^2}{2} - \frac{\mathbf{A}(t) \cdot \mathbf{p}}{c} + V(\mathbf{r}) \right] \psi(\mathbf{r},t) \quad (3.50)$$

and length gauge

$$i\frac{\partial}{\partial t}\psi(\mathbf{r},t) = \left[\frac{\mathbf{p}^2}{2} + \mathbf{E}(t) \cdot \mathbf{r} + V(\mathbf{r}) \right] \psi(\mathbf{r},t) \quad (3.51)$$

for atomic hydrogen with a soft-core Coulomb potential

$$V(\mathbf{r}) = -\frac{1}{\sqrt{\mathbf{r}^2 + \alpha^2}}. \quad (3.52)$$

We consider a linearly polarized laser pulse within the dipole approximation, so $\mathbf{A}(t) = A(t)\hat{z}$ and $\mathbf{E}(t) = E(t)\hat{z}$. Taking advantage of azimuthal symmetry, the wavefunction can be represented in 2D cylindrical coordinates ρ and z . We used the second order finite difference method for spatial derivatives and the fully implicit second order Crank-Nicholson method for time propagation (for more details on the numerical implementation, see [?]). The laser field magnitudes $A(t)$ and $E(t)$ were defined as in Eq. (3.46) and Eq. (3.42), with a Gaussian envelope function $f(t)$. Specifically,

$$A(t) = \frac{E_0 c}{\omega_A} \sin(\omega_A t) e^{-(2t/\tau)^2 \ln 2}, \quad (3.53)$$

where τ is the FWHM pulse duration. The results presented below were obtained in velocity gauge, but additional test calculations in length gauge have confirmed that the results are gauge invariant.

In all calculations for single photon ionization (Sec. ??), excitation (Sec. ??) and high harmonic generation (Sec. ??) we used $\alpha = 0.029$ a.u., a grid spacing of 0.1 a.u., and a time step of 0.1 a.u. The soft core parameter is used to match the ground state energy to that of atomic hydrogen, given by $E_{1s} = -0.5001$ a.u. on the grid, and an excited state energy of $E_{2p} = -0.12504$ a.u. To

ensure the wavefunction remains on the grid for our calculation of the photoelectron spectrum, the grid extended 500 a.u. in the ρ -direction and 1000 a.u. in the z -direction, with an exterior complex scaling absorbing boundary in the outer 50 a.u. for single photon ionization (Sec. ??). The excitation (Sec. ??) and high harmonic generation (Sec. ??) calculations were performed on a grid that extended over 100 a.u. in the ρ -direction and 200 a.u. in the z -direction, with an absorbing boundary over the outer 5 a.u.

First, we consider single photon ionization of the hydrogen atom by a few-cycle laser pulse with peak intensity 10^{13} W/cm² and central frequency $\omega_{\text{central}} = 2.0$ a.u. The central frequency is implemented either by setting $\omega_A = \omega_{\text{central}}$ or setting $\omega_E = \omega_{\text{central}}$, using the method described in the previous section. Photoelectron momentum spectra $P(k)$ were obtained by the following procedure: the TDSE was propagated for five times the FWHM pulse duration plus an additional 100 a.u. in time, then all bound states with principle quantum number $n \leq 8$ were projected out, and lastly the remaining unbound wavepacket ψ_{ionized} was projected onto coulomb wave functions up to $l_{\text{max}} = 5$. That is,

$$P(k) = \sum_{l=0}^{l_{\text{max}}} \left| \int F_l\left(-\frac{1}{k}, kr\right) Y_{l0}^*(\hat{r}) \psi_{\text{ionized}}(\vec{r}) d^3\vec{r} \right|^2. \quad (3.54)$$

The results in Fig. 3.7 show that in fact the photoelectron spectra for central frequency $\omega_A = 2$ a.u. (solid lines) and $\omega_E = 2$ a.u. (dashed lines) do not agree due to the frequency shift. As expected, the discrepancy is larger for 2 cycle FWHM (panel (b)) than for 10 cycle FWHM (panel (a)) pulses. These results however raise the question whether the central frequency of the vector potential ω_A or the central frequency of the electric field ω_E is the relevant quantity for further physical interpretation or a comparison with experimental data. To address this question, we consider the resonant population transfer between bound states by analyzing results of numerical calculation as well as those obtained using first-order perturbation theory in the next subsection.

Next, we examine transitions to the $n = 2$ orbitals in the hydrogen atom as a function of both pulse length and central frequency of the vector potential (ω_A) and the electric field (ω_E). Typically, the excitation probability is greatest when the central frequency of the laser matches the

resonant frequency for n_p photon absorption, given by

$$\omega_{\text{res}} = |E_{\text{final}} - E_{\text{initial}}|/n_p, \quad (3.55)$$

where E_{final} and E_{initial} are the energy of the final and initial state, respectively. In view of the predicted frequency shift between the central frequencies ω_A and ω_E , we therefore expect that the results for resonant excitation will provide insights into the physical relevance of ω_A vs. ω_E .

Within first order perturbation theory, the excitation probability is given by (for further analysis, see Appendix ??):

$$\begin{aligned} P_{i \rightarrow f} &= |\tilde{A}(\omega_{\text{res}})|^2 \left(\frac{\mu \omega_{\text{res}}}{c} \right)^2 \\ &= \frac{\pi}{\ln 2} \left(\frac{\mu E_0 \omega_{\text{res}} \tau}{4 \omega_A} \right)^2 \left[e^{-(\omega_A - \omega_{\text{res}})^2 \tau^2 / (16 \ln 2)} \right. \\ &\quad \left. - e^{-(\omega_A + \omega_{\text{res}})^2 \tau^2 / (16 \ln 2)} \right]^2, \end{aligned} \quad (3.56)$$

Here we have used the pulse defined in Eq. (3.53) and $\mu = 2^{7.5} 3^{-5}$ is the transition dipole for the hydrogen $1s \rightarrow 2p$ transition. Eq. (3.56) shows that the excitation probability $P_{i \rightarrow f}$ is not maximized at $\omega_A = \omega_{\text{res}}$, due to the prefactor of ω_A^{-2} . This prefactor originates from Eq. (3.46), where it ensures that the peak intensity is held fixed as ω_A changes.

We have also obtained the population in the $2p$ state due to single photon excitation by direct numerical solution of the TDSE. These numerical results are presented together with those obtained within first order perturbation theory, Eq. (3.56), in Fig. 3.8 as function of ω_A (left column) and ω_E (right column) for various pulse lengths. The pulse length τ is measured in multiples of the period associated with the resonant frequency

$$\tau_{n_p} = \frac{2\pi}{\omega_{\text{res}}} = \frac{2\pi n_p}{|E_{\text{final}} - E_{\text{initial}}|}, \quad (3.57)$$

such that $\tau_1 \approx 405$ attoseconds, $\tau_2 \approx 811$ attoseconds and so on for the $1s \rightarrow 2p$ transition. For long pulses the peak in the population (marked by a green dot) occurs at the expected frequency ω_{res} (marked by vertical line) for a resonant transition in all distributions. When the pulse length is decreased, the peak in the distributions as a function of ω_E (right column) remains at ω_{res} . In

contrast, the peak shifts significantly towards lower frequencies in the distributions as a function of ω_A (left column) due to the frequency shift. We note that the results of our numerical calculations (upper row) are in excellent agreement with those obtained using first-order perturbation theory (lower row) and indeed both reveal the same dependence on the central frequencies ω_A and ω_E . Thus, the differences in the distributions as functions of ω_A and ω_E are not a numerical artifact but are due to the frequency shift. Furthermore, the observed shift agrees with our estimate obtained in the previous section. Thus, we can conclude that the central frequency of the electric field is the physically relevant quantity for interpreting laser induced excitation processes.

These conclusions are further supported by our numerical results for two-photon excitation from the $1s$ to the $2s$ state in Fig. 3.9. Whereas the peak of the population as a function of ω_E (panel b) occurs at ω_{res} , independent of the pulse duration, the peak of the population as a function of ω_A once again shifts to lower frequencies in Fig. 3.9(a). We note that, if the population as function of ω_A in Figs. 3.8 and 3.9 were used to determine the energy difference $|E_{\text{final}} - E_{\text{initial}}|$, the error caused by the frequency shift would be twice as much in the two-photon case as in the one-photon case, accounting for the difference in τ_{n_p} . This indicates that multiphoton processes may be affected by the frequency shift even more than few-photon processes. To further illustrate this point, we examine high harmonic generation in subsection ??.

Finally, we consider a highly nonlinear laser induced process. High harmonic generation (HHG) in atoms can be described as absorption of an odd number of photons leading to the excitation of a electron, followed by the emission of a single photon as the electron recombines into the ground state. Based on the results above, we expect that in this nonlinear process the frequency shift $\Delta\omega$ between ω_A and ω_E will lead to a shift of the energy of the n_p th harmonic by $n_p\Delta\omega$. In our calculations the HHG spectrum has been obtained by a Fourier transformation of the time dependent dipole acceleration along the laser polarization direction. A Hanning filter was used to return the dipole acceleration to zero at the beginning and end of the simulation.

Fig. 3.10 shows the various harmonics in a HHG spectrum as a function of the number of cycles in the driving laser pulse at a peak intensity of 1×10^{14} W/cm² and central frequencies $\omega_A = 0.0625$

a.u. (upper panel) and $\omega_E = 0.0625$ a.u. (lower panel), corresponding to a wavelength of 730 nm. The spectrum consists of odd harmonics and additional emission lines due to the population of excited states during the interaction with the laser pulse. While we will focus on the generation of harmonics, we note that the emission lines occur at photon energies between the 5th and 9th harmonics. The corresponding field-free energy differences between the excited states and the ground state in our numerical model of the hydrogen atom are marked, as reference, by white vertical dashed lines.

In the spectrum as function of multiples of ω_A (panel a) one can see that the centers of the harmonics do shift to energies larger than $n_p\omega_A$, as the pulse duration decreases. In fact, the energies of the harmonics follow the analytical predictions for $n_p\omega_E$ (green solid lines). As expected, the shift is as larger as larger the harmonic number. In contrast, in the HHG spectrum obtained as multiples of ω_E (panel b) the centers of the harmonics remain at the same energy, i.e. $n_p\omega_E$ (green solid lines), as the pulse duration decreases. This confirms the importance of the shift between the central frequencies of the vector potential and the electric field in nonlinear processes driven by ultrashort pulses. Furthermore, the HHG results confirm that the central frequency of the electric field ω_E is the physical relevant quantity for the interpretation of light induced processes. Consequently, if in a numerical simulation or theoretical analysis the vector potential is set via Eq. (3.46) it is necessary to consider the frequency shift between ω_A and ω_E to avoid a misinterpretation of the results. Our analytical estimates of the frequency shift in Eq. (3.43) and Eq. (3.49) provide formulas to obtain ω_A from the physically relevant ω_E .

We have shown that the definition of the electric field of a laser pulse via the derivative of the vector potential, which guarantees that both quantities vanish at the beginning and end of the pulse, implies that the central frequencies of the spectral distributions of the vector potential and electric field do not coincide.

In our analysis we have derived an analytical estimate of the frequency shift, which shows that the shift mainly depends on the number of cycles in the pulse and becomes most relevant for few-cycle pulses. Utilizing results of numerical simulations and first-order perturbation theory we have

analyzed how the frequency shift affects excitation, ionization and high harmonic generation induced by short laser pulses. The effect is found to be most noticeable in nonlinear strong-field processes since the frequency shift scales with the number of photons involved. Both, numerical results and predictions based on first-order perturbation theory agree well with each other and confirm that the central frequency of the electric field is the physically relevant quantity for the interpretation of the light induced processes. Thus, the shift should be taken into account when setting the central frequency of the vector potential in numerical simulations to avoid potential misinterpretation of the theoretical results, specifically when compared to experimental data. Eq. (3.43) and Eq. (3.49) provide formulas to obtain ω_A from the physically relevant ω_E .

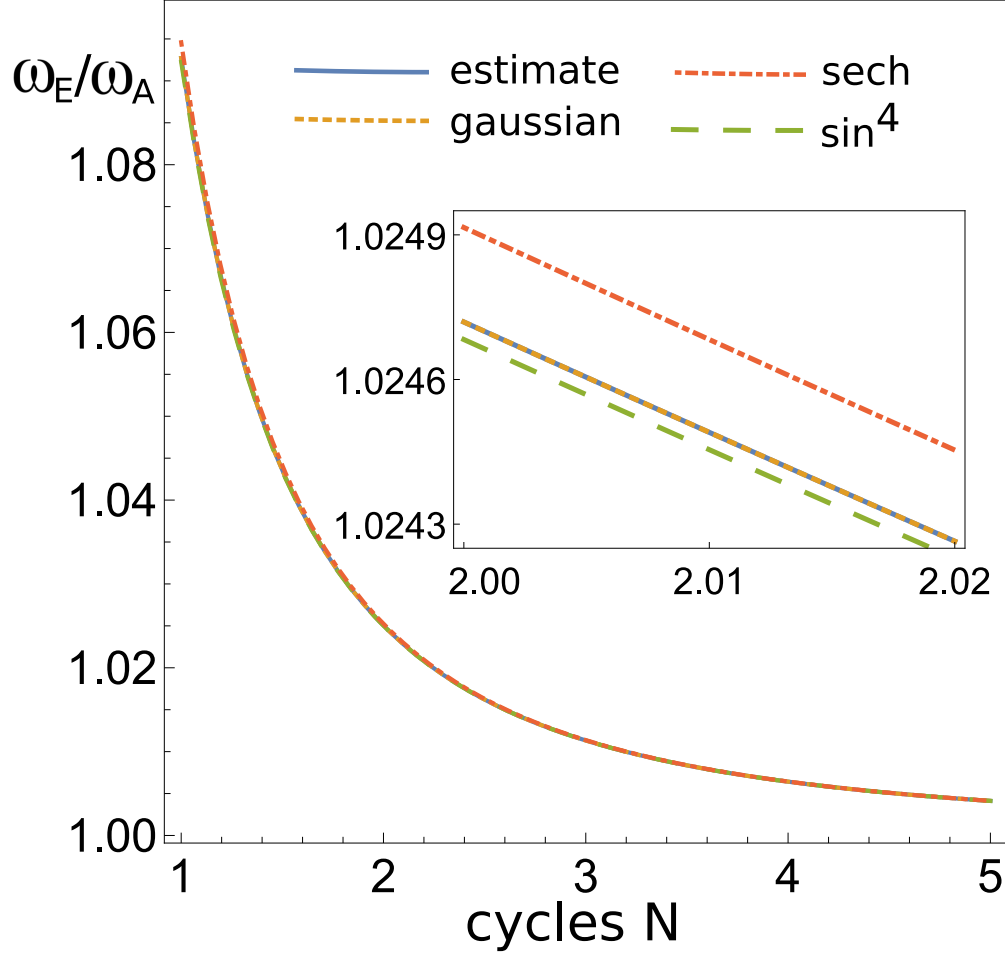


Figure 3.6: (Color online) Ratio ω_E/ω_A as a function of the normalized number of cycles N defined in Eq. (3.44). The numerical results were calculated by maximizing $\tilde{E}(\omega)$ for Gaussian (dotted line), sech (dashed-dotted line), and \sin^4 (dashed line) envelopes and are compared with the simple analytic estimate (solid line) given in Eq. (3.43). The inset reveals a slight dependence on envelope shape, which can be attributed to the correction term in Eq. (3.43).

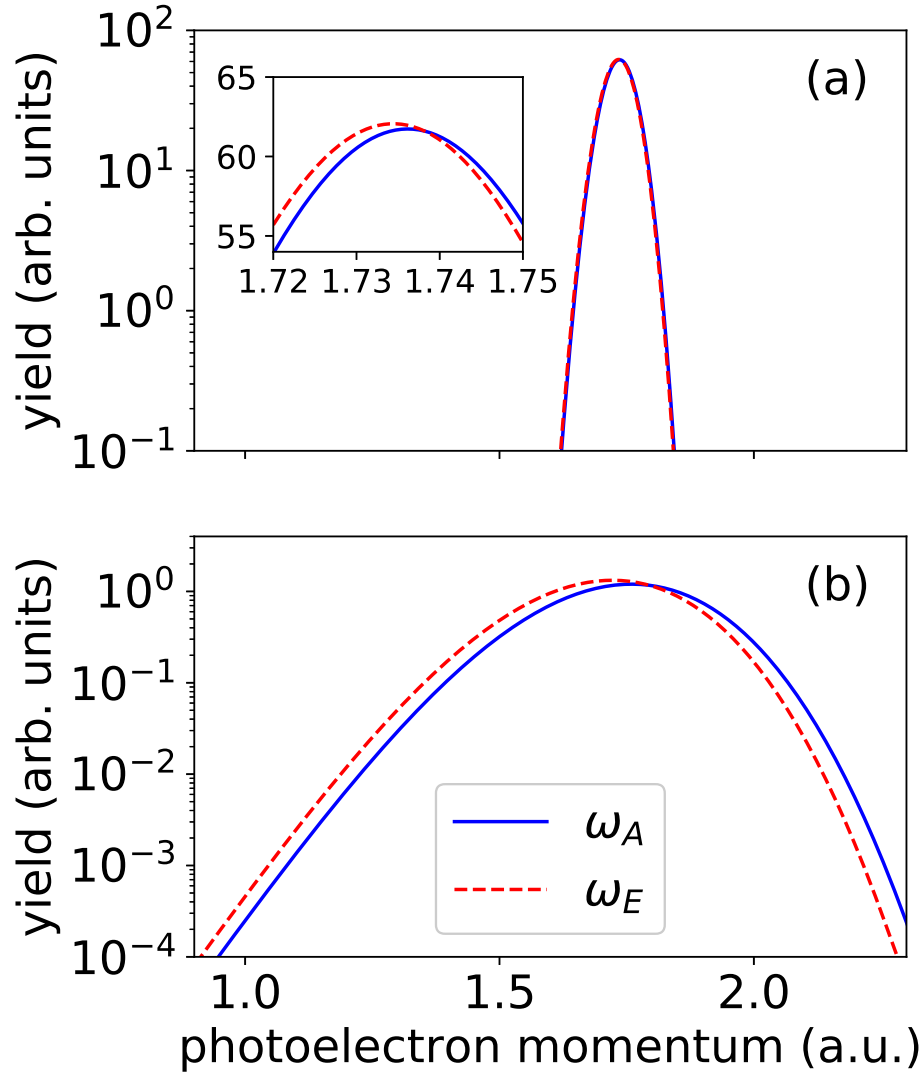


Figure 3.7: (Color online) Photoelectron spectra $P(k)$ as function of photoelectron momentum obtained for interaction of hydrogen atom with laser pulses at central frequencies $\omega_A = 2$ (dashed line) and $\omega_E = 2$ (solid line) and duration of (a) 10 cycles and (b) 2 cycles FWHM.

Figure 3.8: (Color online) Population in $2p$ state following one-photon excitation of hydrogen atom with a laser pulse as a function of ω_A (left) and ω_E (right) for different pulse lengths at peak intensity 10^{12} W/cm². Each line represents results obtained for a fixed pulse duration in terms of $\tau_1 = 405$ as. The results from time-dependent Schrödinger equation (TDSE) calculations (a,b) and predictions within first-order perturbation theory (PT) (c,d) are in excellent agreement. The vertical line marks the energy difference between $2p$ and initial $1s$ state. The green dots indicate the maximum excited state population for each pulse duration.

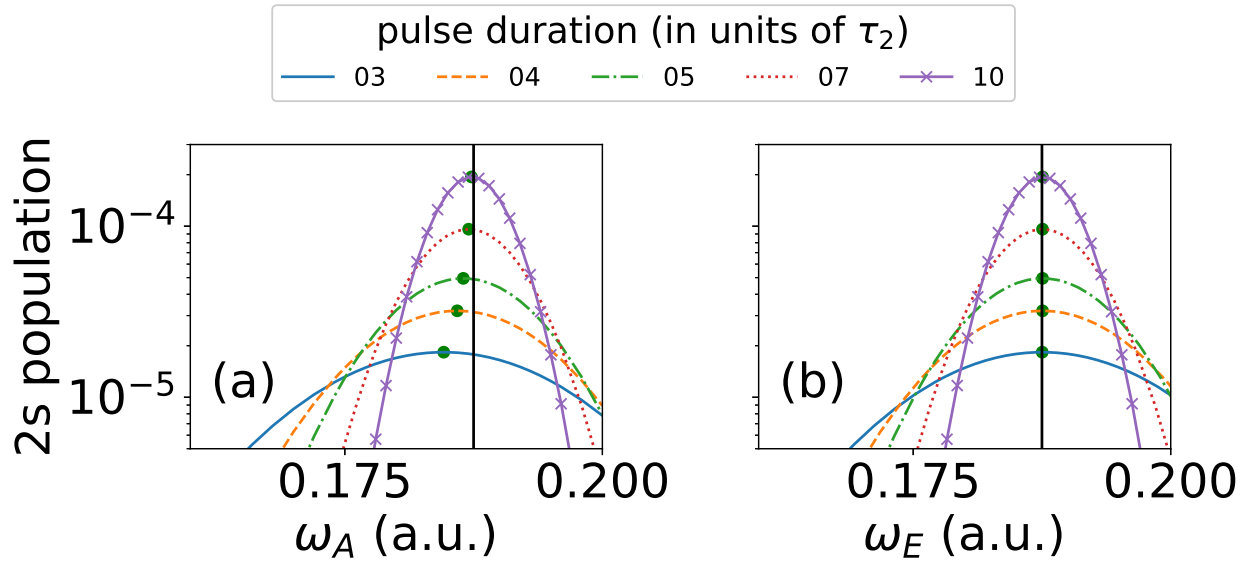


Figure 3.9: (Color online) Numerical results for population in $2s$ state following 2-photon excitation with $\tau_2 = 811$ as. The vertical line marks half of the energy gap between $1s$ and $2s$ representing the resonance condition for the two photon process. Other parameters are the same as in Fig. 3.8.

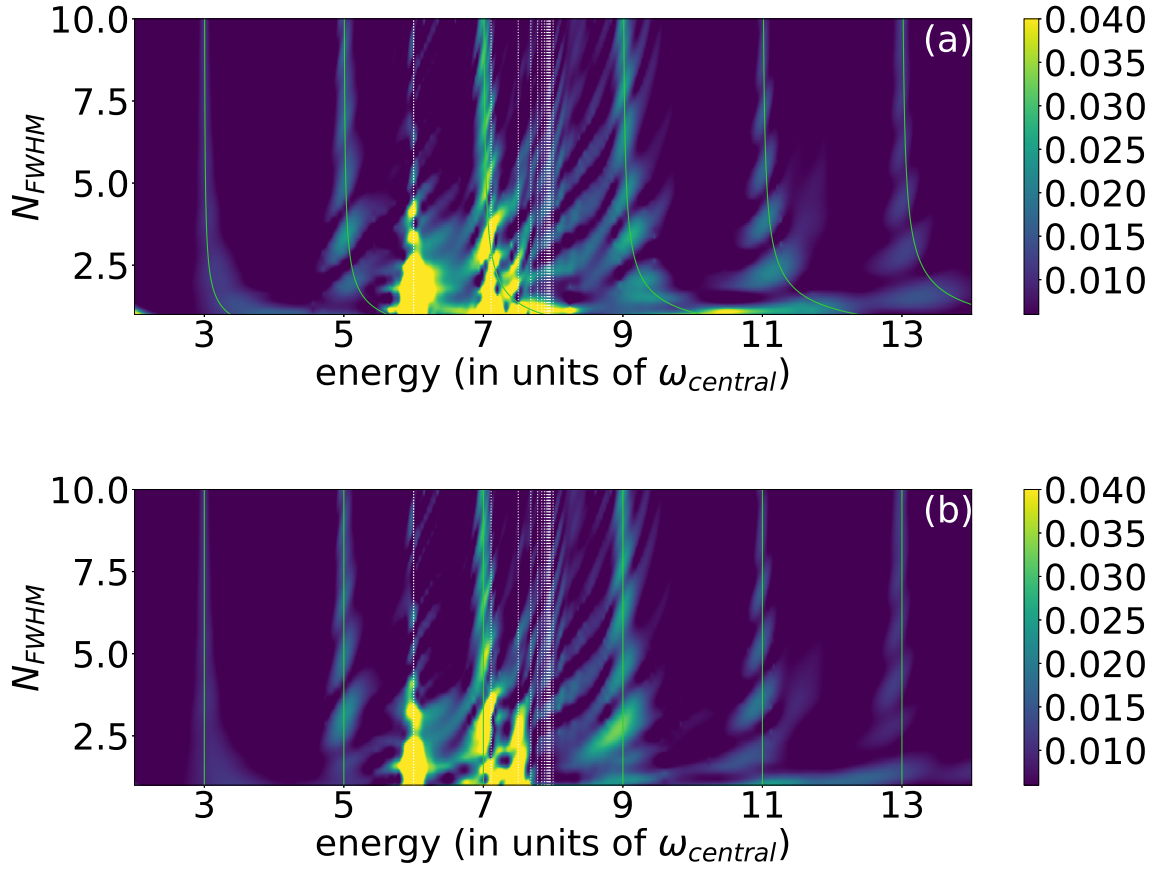


Figure 3.10: (Color online) HHG spectrum at driver wavelength 730 nm ($\omega_{\text{central}} = 0.0625$ a.u.) vs. number of cycles N_{FWHM} . In the upper plot the central frequency $\omega_A = \omega_{\text{central}}$ while in the lower panel $\omega_E = \omega_{\text{central}}$. The vertical white dashed lines mark field-free transition energies between excited states and the ground state, while the green solid lines mark the harmonic energies $n_p \omega_E$ with respect to the central frequency of the electric field.

Chapter 4

Imaging attosecond wave packet dynamics with photoelectrons

Ultrabright light sources such as free-electron lasers [69] and table-top laser systems based on high-order harmonic generation [58, 11] deliver high-intensity pulses of few- or sub-femtosecond duration. Nowadays, laser pulses with a duration of a few tens of attoseconds have been achieved experimentally [83, 10]. Isolated attosecond pulses or trains of attosecond pulses have been generated from the vacuum ultraviolet to the soft X-ray wavelength regime and the polarization of such pulses can nowadays be controlled. This recent progress in ultrafast laser pulse technology makes it possible to probe, steer and control the dynamics of electrons in atoms, molecules and solids [76, 55, 7, 80, 61, 56]. To name a few examples, the time-resolved measurement of the electron emission in the photoelectric effect has been realized [8, 67, 42, 72, 37]. Using an isolated attosecond pulse or a train of extreme-ultraviolet attosecond pulses to ionize an atom along with an infrared laser field interferograms have been measured to obtain information about phases of electron wavepackets, an important milestone towards reconstructing the wavefunctions of atoms [63, 47]. By extracting the phase and amplitude via application of photoelectron spectroscopy recently the birth of a photoelectron through a Fano resonance has been observed on the attosecond time scale [25].

Probing atoms and molecules in their ground or excited states with ultrashort laser pulses opens a new regime where several linear and nonlinear ionization pathways compete and interfere [36, 45, 24, 14, 31, 5, 78, 74]. For example, it has been shown how the competition between resonant and nonresonant pathways depends on the pulse width [36]. An important observable

are photoelectron angular distributions (PAD), which are measured by detecting the probability for emission of the electron from the target in different directions. Since PADs are determined by the amplitudes and phases of the partial waves of all pathways contributing to the emission, they are practical means to identify the different contributing pathways. A characteristic signature of such interferences are asymmetries in the emission of the photoelectron [81]. In the simple case of photoionization from a single state, anisotropy and asymmetry parameters have been used in the past to identify and analyze interesting physical effects. A significant circular dichroism via the asymmetry in the forward-backward electron emission from bromocamphor molecules induced by circularly polarized light has been identified [6]. Observation of the breakdown of the symmetry in the photoelectron emission of argon has been shown in the region of the Cooper minimum [35]. Interferences between resonant and non-resonant pathways [36] or direct and autoionizing channels [12] can be identified via anisotropy and asymmetry parameters. Other examples can be found in double photoionization [46] or molecular vibrations and chirality [21] and applications range from studies of coherent control [60] to the characterization of ultrashort laser pulses [9].

In this chapter, I examine the photoangular distributions (PAD) produced when atoms are ionized by few photon processes induced by ultrashort pulses through the lens of imaging attosecond dynamics. In Sec. 4.1 I present the impact of the increased bandwidth of these short pulses the PAD for a two-photon process including intensity and pulse jitter studies. Sec. 4.2, I present a set of generalized asymmetry parameters (GAPs) that extend the standard front back asymmetry parameter to allow for studying interference of states with differing magnetic quantum numbers that are produced with circular and elliptically polarized laser pulses including a discussion of linear and circular probe pulses. Finally, I look at the time dependent ionization Helium atom in a $1s - 2p_1$ and design tools capable of reconstructing dynamics that repeat over 200 attosecond period in Sec. 4.3

4.1 Short pulse effect in helium

The production of extreme-ultraviolet (EUV) pulses using high harmonic generation (HHG) and free-electron lasers (FEL) has led to a resurgence of multiphoton ionization studies in the perturbative intensity regime recently [?, ?, ?, ?, ?, ?, ?, ?, ?, ?, ?, ?, ?, ?, ?, ?]. Along with experimental techniques, such as velocity map imaging [?, ?] or cold target recoil ion momentum spectroscopy [?], the detection of angle-resolved emission of the photoelectron following few-photon ionization of atomic and molecular targets has become possible [?]. Photoelectron angular distributions (PAD) are determined by the amplitudes and phases of the partial waves of all pathways contributing to the emission at a given energy into a given solid angle. PADs and related anisotropy parameters are therefore useful observables to obtain quantitative insights in the relative strength of the different pathways and their competition. This has been demonstrated in the past for the competition between resonant and non-resonant two-photon ionization pathways [?, ?, ?] and for one- and two-photon ionization channels [?, ?, ?]

Two-photon ionization of atoms, specifically the helium atom, have been studied in theory and experiment in the past, first concerning total ionization yields [?, ?, ?, ?, ?, ?, ?] and, more recently, with a focus on photoelectron angular distributions [?, ?, ?, ?]. It has been shown, that the PADs strongly depend on the pulse duration or, equivalently, the spectral width of the EUV pulses. Initially, theoretical studies by Ishikawa and Ueda revealed that the competition between resonant and nonresonant pathways depends on the pulse width [?, ?]. Changes in the PADs for 1 - 21 fs pulses at photon energies below the first ionization energy were characterized by the even anisotropy parameters β_2 and β_4 . Via these parameters the relative phase between the s - and d -wave packets for the photoelectron emission can be determined. Related experimental work at the SPring-8 Compact SASE Source test accelerator verified the co-presence of the two pathways [?]. Very recently, Boll et al. extended these studies, covered a much wider photon energy range and explored the impact of radial and angular electron correlation [?]. They showed that in the low-energy regime a single-active-electron picture is valid while at higher energies in the regime of

autoionizing states angular correlations play a major role for the understanding of the PADs.

The ongoing quest in shortening pulses at extreme- and deep-ultraviolet wavelengths towards the single-cycle regime in duration are achieved via large spectral widths. Such broadband energy pulses give rise to competition between one- and two-photon (as well as three-photon) ionization processes for emission at a given energy. As mentioned in Ref. [?], in helium atom this leads to the additional interference of the s - and d -wave packets due to two-photon absorption with a p -wave packet from single photon absorption. In this work, we study the transition regime between single photon ionization and two-photon absorption. We first show how in this regime the PADs quickly change over a small window of pulse duration, about 1 cycle in full width at half maximum (FWHM). The variation is reflected in the anisotropy parameters β_i ($i = 1, 2, 3$ and 4), which show the transition as well as the interference between the ionization pathways. The dependence on pulse duration, photon energy as well as photoelectron energy is studied. We further consider how variation of pulse parameters, such as the carrier-envelope-phase (CEP), the peak intensity, and the partial coherence of FEL pulses, do impact the anisotropy parameters. Finally, we briefly study at which intensities three-photon ionization, which occurs for these large bandwidth pulses as well, may become observable. In order to accurately account for the different pulse parameters, we have performed simulations based on the time-dependent Schrödinger equation. Since a recent study has shown that for pulses with central photon frequency below the first ionization potential of the helium atom the single active electron (SAE) picture remains valid [?], we have used a SAE potential for our numerical simulations.

We solve the time dependent Schrödinger equation for the interaction of a electron in a spherically symmetric single-active-electron (SAE) potential with the electric field \mathbf{E} of a linearly polarized laser pulse (along the \hat{z} -direction) in dipole approximation and length gauge (we use Hartree atomic units $e = m_e = \hbar = 1$):

$$i \frac{\partial}{\partial t} \Psi(\mathbf{r}, t) = \left[-\frac{\nabla^2}{2} - \mathbf{E}(t) \cdot \mathbf{z} + V(r) \right] \Psi(\mathbf{r}, t). \quad (4.1)$$

The wavefunction Ψ is expanded in spherical harmonics up to $l_{max} = 20$ with $m = 0$ due to the

symmetry of the problem. The radius is discretized using fourth order finite difference method with a grid spacing of 0.05 a.u. and a maximum radius of 300 a.u. We utilized the exterior complex scaling method on the outer 30 a.u. of the grid. The wavefunction is propagated in time using the Crank-Nicolson method with a time step of 0.01 a.u. In test calculations the numerical code was compared against results from a previously used 2D cylindrical code [?], results from time-dependent perturbation theory in the appropriate intensity and frequency regimes, as well as results reported in the literature [?]. Quantitative agreement was achieved.

In our work we consider ionization of helium atom with pulses at central photon energies below the first ionization potential. In a recent study [?] it has been shown that in this photon energy regime the SAE picture remains valid. We therefore utilize a SAE potential for helium atom

$$V(r) = -\frac{1}{r} - \frac{e^{-2.0329r}}{r} - 0.3953e^{-6.1805r}. \quad (4.2)$$

Our numerical simulations have been performed for laser pulses with central frequencies at or near to the energy difference between the field-free $1s$ and $2p$ state of the helium atom. In our SAE model of helium the ground state energy is -0.944 a.u., while the $2p$ energy is -0.128 a.u.

To ensure that the electric field integrates to zero [?], we set the vector potential as

$$A(t) = A_0 \exp \left(-\ln(2) \left(\frac{2(t-\tau_0)}{T} \right)^2 \right) \times \sin(w_A(t-\tau_0) + \phi) \quad (4.3)$$

with $A_0 = \frac{c\sqrt{I_0}}{\omega_A}$, $T = \frac{2\pi N}{\omega_A}$, c is the speed of light, I_0 the peak intensity, N the number of cycles in the pulse, ω_A denotes the central frequency of the vector potential, and ϕ is the carrier-to-envelope phase. The electric field is then obtained as

$$E(t) = -\frac{1}{c} \frac{\partial}{\partial t} A(t). \quad (4.4)$$

The central frequencies of the spectral distributions of the vector potential, ω_A , and the electric field, ω_E , can differ significantly for an ultrashort laser pulse [?]. In the presentation of the results below we state the physically relevant central frequency ω_E , in the simulations ω_A is determined such that ω_E matches the reported central frequency [?].

As result of our ab-initio numerical calculations we obtain the wavefunction at the end of the interaction with the laser pulse. Via projection on continuum states we can then determine the ionization probability as well as photoelectron energy and angular distributions. If more than one pathway, here, e.g., one- and two-photon ionization, contribute to the emission of the photoelectron at a given energy in a given direction, our numerical simulations do not allow for the separate the respective probabilities for each channel easily. This is in contrast to calculations based on perturbation theory, in which the amplitude for each pathway is evaluated and can be analyzed separately. In order to analyze the dominant pathways for photoemission as functions of intensity, photoelectron energy and pulse duration, we therefore determine anisotropy parameters (β -parameters), which provide quantitative insights in the different pathways involved as well as the interference between them [?, ?, ?].

It has been shown [?] that the photoelectron angular distribution for an isotropic target is given by:

$$P(E, \theta) = \frac{\sigma(E)}{4\pi} \left[1 + \sum_{j=1}^n \beta_j(E) P_j(\cos(\theta)) \right] \quad (4.5)$$

where θ is the angle of electron emission with respect to the polarization direction of the laser field, while $\sigma(E)$ is the ionization probability at E and P_j are the Legendre polynomials. The anisotropy parameters β_j depend on the amplitudes of the different pathways leading to emission of the photoelectron (for explicit expressions, see [?]). For combinations of one- and two-photon ionization processes, that will be the focus of this work, contributions from the first four β_j -parameters are expected. The contributions related to the odd polynomials indicate interference between partial waves resulting from one- and two-photon absorption. We also note that the impact of three-photon ionization, that we will briefly consider below, is expected to show up in the anisotropy parameter β_5 and higher order parameters.

We have determined the anisotropy parameters in our calculations using Equation (4.5) as follows. At the end of the simulations of the time-dependent Schrödinger equation we obtained the photoelectron angular distribution at a given momentum k by projecting the wavefunction onto the

Figure 4.1: Schematic representation of one- (a), two- (b), and three-photon (c) ionization in an ultrashort pulse. The Gaussian distribution shows the spectral width of the ultrashort pulse centered about the energy of the $2p$ -state. The red arrows represent the photon absorption pathways, and the black lines depict some of the resonant structure of the helium atom.

field-free continuum states on the numerical grid. The numerically obtained PAD has been then projected onto the j -th Legendre polynomial P_j ($j = 1, \dots, 5$) and the results have been normalized using the total ionization probability σ .

Following a general discussion of the processes involved in subsection 3.1, we present PADs and related anisotropy parameters for pulses having a Gaussian envelope. The results are analyzed, in view of a competition between one- and two-photon ionization, as a function of pulse duration, central frequency and peak intensity in subsection 3.2. Fluctuations of the carrier-envelope-phase, the peak intensity and the partial coherence of FEL pulses are studied in subsection 3.3.

To first illustrate the impact of the one-, two- and three-photon ionization pathways on the emission of the photoelectron in ultrashort laser pulses, let us consider an emission induced by a pulse with central frequency ω_0 tuned to the $1s - 2p$ energy gap. The broad energy spectrum of an ultrashort Gaussian pulse is schematically depicted in the panels of Figure 4.1 centered about the energy of the $2p$ -state. Absorption of two photons by an electron in the ground state at the central frequency ω_0 (c.f., Figure 4.1(b)) will lead to its emission at energy $E = 2\omega_0 - |E_{1s}|$. If the bandwidth of the pulse is broad enough (i.e., the pulse duration is sufficiently short) ionization of a photoelectron with the same photoelectron energy can occur via absorption of one photon with energy $2\omega_0$ (c.f., Figure 4.1(a)) or via absorption of three photons with energy $\frac{2}{3}\omega_0$ (c.f., Figure 4.1(c)). We note that besides the two-photon and three-photon pathways with absorption of photons of equal energies, there exist more such pathways to a final photoelectron energy E for absorption of photons with unequal energy as long as the sum of the photon energies is equal to $2\omega_E$.

The occurrence of the one- and three-photon processes requires a broad spectral bandwidth of the pulse. That means, for long pulses we expect that only the two-photon ionization process is

Figure 4.2: Photoelectron angular distributions for helium atom ionized by laser pulses at central photon energy $\omega_0 = 22.2$ eV, peak intensity $I_0 = 10^{11}$ W/cm², carrier-to-envelope phase $\phi = 0$ and three different pulse durations: $N = 0.6$ FWHM cycles (0.112 fs, left column), $N = 1.2$ FWHM cycles (0.224 fs, middle column) and $N = 1.8$ FWHM cycles (0.335 fs, right column). Angular distributions are obtained for three values of photoelectron energy $E = 1.45(2\omega_0 - |E_{1s}|) = 1.0$ a.u. (top row), $E = 2\omega_0 - |E_{1s}| = 0.687$ a.u. (middle row), and $E = 0.58(2\omega_0 - |E_{1s}|) = 0.4$ a.u. (bottom row), where E_{1s} is the energy of the $1s$ state in the SAE potential.

present. If the pulse is shortened to a few optical cycles, both the one- and three-photon channels become effective, since the probability of photon absorption at energies away from the central frequency increases. In the perturbative intensity regime the probability for a n -photon process scales as I^n , where I is the intensity of the pulse. We therefore expect that at a given ultrashort pulse duration at low intensities the one-photon process dominates over the two-photon process in an ultrashort laser pulse. As the intensity increases, first the two-photon process should then become dominant, before at significant high intensities contributions from the three-photon process will become detectable. In the present paper, we mainly study the transition from one- to two-photon processes, while the influence of the three-photon process will be given minor attention.

In Figure 4.2 we present examples of PADs that show the transition from single photon ionization, illustrated by the p -wave character of the distribution (panels (d, g, h)), to an emission following two-photon absorption, highlighted by the dominating d -wave character in the PAD (panels (b, c, f)). The results are obtained for ionization by a laser pulse at a central photon energy $\omega_0 = 22$ eV, which corresponds to the energy difference between the $1s$ - and $2p$ -states in the single-active-electron potential for helium used in the calculations, peak intensity $I_0 = 10^{11}$ W/cm² and carrier-to-envelope phase $\phi = 0$. At a given photoelectron energy, the transition occurs for a variation of the pulse duration, e.g. at $E = 2\omega_0 - |E_{1s}| = 0.687$ a.u. from 0.112 fs to 0.335 fs (middle row). Conversely, for a fixed pulse duration, the transition is seen for increase of the photoelectron energy, e.g. at $\tau = 0.224$ fs from 0.4 a.u. to 1.0 a.u. (middle column). In the transition regime the PADs exhibit the interference between the one- and two-photon ionization processes.

Further insights in the transition between the two processes can be found via the cross section

Figure 4.3: Cross section $\sigma(E)$ as a function of peak intensity for photoelectron emission at energy $E = 2\omega_0 - I_p = 18.7$ eV in 0.5-cycle (one-photon process dominates), 1.0-cycle (transition regime), and 1.5-cycle (two-photon process dominates). Central photon energy $\omega_0 = |E_{2p} - E_{1s}| = 22.2$ eV and carrier-to-envelope phase $\phi = 0$

$\sigma(E)$ and the first four anisotropy parameters β_i ($i = 1, \dots, 4$). In Figure 4.3 the results for the cross section are shown as function of peak intensity at fixed photon and photoelectron energies. The cross section for a 0.5 cycle pulse has a slope of one corresponding to the dominance of one photon ionization over the whole intensity regime. In contrast, the cross section obtained for the 1.5 cycle pulse is dominated by the two photon process due to the reduced bandwidth of the pulse. In the data for the 1-cycle pulse the transition from the one- to the two-photon process is seen to occur near 10^{12} W/cm².

In Figure 4.4 the results for the β -parameters are shown as function of pulse duration and peak intensity at fixed photon and photoelectron energies. The even β -parameters show the transition from dominant one-photon ionization ($\beta_2 > 0$, $\beta_4 \approx 0$) to dominant two-photon ionization ($\beta_2 \approx 0$, $\beta_4 > 0$), while the odd β -parameters exhibit the regime of interference between the two processes ($\beta_1 < 0$ and $\beta_3 < 0$ for $\phi = 0$). The latter peak where the magnitudes of the two transition amplitudes coincide. At a given peak intensity the interference regime extends over a change of pulse duration of about 0.5 cycles at FWHM. For a fixed pulse duration, the interference regime extends over a variation of peak intensity by a factor of 2-5. The results are therefore rather stable with respect to intensity fluctuations of the pulse. The impact of other potential pulse fluctuations in the experiment on the β -parameters will be discussed in subsection ??.

The transition probabilities of the one- and two-photon processes, σ_1 and σ_2 , scale linearly and quadratically with intensity. Assuming that the two-photon ionization process involves predominantly the absorption of photons at equal energies, the peak intensity at maximum interference can be estimated as $I_{infer} \propto D^{(1)}(E)f(\Omega)/(D^{(2)}(E)f^2(\omega))$, where $D^{(i)}(E)$ is the square of the transition dipole moments for the one- and two-photon process, f is the spectral distribution of the pulse and $\Omega = 2\omega = E + |E_{1s}|$. Since $\omega = \omega_0$ for the results in Figure 4.4, $f(\omega) = f(\omega_0) = 1$ and

Figure 4.4: Parameters β_1 (a) to β_4 (d) as function of pulse duration (FWHM) and peak intensity. Central photon energy $\omega_0 = |E_{2p} - E_{1s}| = 22.2$ eV, carrier-to-envelope phase $\phi = 0$ and photoelectron energy $E = 2\omega_0 - I_p = 18.7$ eV.

$I_{infer} \propto f(\Omega)$. Thus, we expect that the interference between the two processes requires a larger spectral bandwidth, i.e. shorter pulse duration, the larger the peak intensity of the pulse. The results in Figure 4.4 confirm this expectation.

Next, we consider how the transition between the two pathways depends on the photoelectron energy and the central photon frequency at a given peak intensity $I_0 = 10^{11}$ W/cm² and carrier-to-envelope phase $\phi = 0$. To this end, we show in the Figure 4.5 the anisotropy parameters β_1 (left column) and β_2 (right column) as a function of photoelectron energy and pulse duration for central frequencies below (top row), on (middle row) and above (bottom row) resonance with the $1s - 2p$ transition in the helium single-active-electron potential. We restrict ourselves to β_1 and β_2 since the higher order β -parameters contain equivalent information (see Figure 4.4). Also shown in Figure 4.5 is the photoelectron energy $E = 2\omega_0 - I_p$, corresponding to a two-photon transition at the central frequency ω_0 .

The comparison shows that the transition regime depends on the central frequency, since the regime shifts for a given pulse duration to larger photoelectron energies as the central frequencies increases (from bottom to top). At a given central frequency, the pulse duration, at which the transition between the one- and two-photon ionization pathways occurs, increases as the photoelectron energy decreases. Qualitatively, this dependence can be understood using the relation $I_{infer} \propto D^{(1)}(E)f(\Omega)/(D^{(2)}(E)f^2(\omega))$. For photoelectron energies larger than $E = 2\omega_0 - I_p$ (dashed line), both ω and Ω are larger than the central frequency. Consequently, at large photoelectron energies a broader spectral distribution (shorter pulse duration) is required for the same value of $f(\Omega)/f^2(\omega)$ than at photoelectron energies below $E = 2\omega_0 - I_p$ (dashed line), where $\omega < \omega_0$ while $\Omega > \omega_0$.

In the limit of short pulses and high intensities, both the one- and three-photon processes can

Figure 4.5: Anisotropy parameters β_1 (left) and β_2 (right) as function of pulse duration and photoelectron energy E for central frequencies $\omega_0 = 1.1|E_{1s} - E_{2p}|$ (top row), $\omega_0 = |E_{1s} - E_{2p}|$ (middle row) and $\omega_0 = 0.9|E_{1s} - E_{2p}|$ (bottom row) at peak intensity of 10^{11} W/cm² and $\phi = 0$. In each panel the dashed line corresponds to $E = 2\omega_0 - I_p$.

interfere since the three-photon process scales with I^3 . The results for the anisotropy parameter β_5 in Figure 4.6 confirm this expectation. At a photoelectron energy of $2\omega_0 - |E_{1s}|$ (panel (a)) a peak intensity of about 10^{14} W/cm² and a rather large spectral bandwidth is required to facilitate the three-photon process with significant probability since the corresponding photon energies are smaller than the central frequency. The distribution over photoelectron energy (panel (b)) shows that the impact of the three-photon ionization process is indeed more visible at energies near $E = 3\omega_0 - |E_{1s}|$.

For the discussion in the previous subsection we have considered results obtained at fixed pulse parameters. The results in Figures 4.4 and 4.5 show that the transition regime occurs over a rather small window of pulse duration while it appears to be rather stable for variations of the peak intensity up to half an order of magnitude. The photon energies in the extreme ultraviolet can be nowadays generated using high-order harmonics or free electron lasers. In view of the technical difficulties to control the carrier-to-envelope (CEP) of ultrashort pulses as well as the fluctuating pulse shapes in the self-amplified spontaneous emission (SASE) mode of free electron lasers, we have studied the impact of these variations on the anisotropy parameters.

To study the dependence on the CEP we have averaged the results about a given value ϕ_0 using a Gaussian distribution of width α as:

$$\beta_j^{(\alpha)}(\phi_0) = \frac{\sum_i \exp\left[-\frac{1}{2}\left(\frac{|\phi_i - \phi_0|}{2\pi\alpha}\right)^2\right] \sigma(\phi_i) \beta_j(\phi_i)}{\sum_i \exp\left[-\frac{1}{2}\left(\frac{|\phi_i - \phi_0|}{2\pi\alpha}\right)^2\right] \sigma(\phi_i)}, \quad (4.6)$$

where $\sigma(\phi_i)$ is the total ionization probability at CEP ϕ_i . The results for averages with (b) $\alpha = 0.2$ and (c) $\alpha = 0.4$ are compared in Figure 4.7 with the unaveraged results (panel (a)). As expected, the odd β -parameters, which reflect the interference between the one- and two-photon processes, strongly depend on CEP, while the even parameters are independent of it. Thus, the transition

Figure 4.6: Anisotropy parameter β_5 (a) as function of pulse duration and peak intensity at central frequency $\omega_0 = |E_{1s} - E_{2p}|$ and photoelectron energy $2\omega_0 - |E_{1s}|$ and (b) as function of pulse duration and photoelectron energy at central frequency $\omega_0 = 0.9|E_{1s} - E_{2p}|$ and peak intensity of 10^{13} W/cm². The dotted lines correspond to $E = 2\omega_0 - I_p$ and $E = 3\omega_0 - I_p$. The other parameters are as in Figures 4.4 and 4.5, respectively.

from one-photon to two-photon ionization can be observed via β_2 and β_4 even in pulses without CEP stabilization. Although the odd parameters depend on CEP, the corresponding results appear to be indicative for the transition up to fluctuations of about $\pi/2$.

We have further studied the impact of fluctuations of temporal FEL laser pulse shapes [?]. We note that current FEL technology does not provide the bandwidth required to generate pulses down to the one- or two-cycle limit at the photon energies considered here. We may still attempt to give some theoretical insights concerning the robustness of the signal against the major fluctuations present in an FEL pulse. To this end, we have applied a partial coherence method, which has been used before to model longer FEL pulses [?]. We note that future technological progress towards generation of ultrashort FEL pulses in the EUV regime may necessitate to extent the current approach.

To generate the FEL pulses used in the numerical simulations, the spectrum of a vector potential with Gaussian envelope corresponding to peak intensity I_0 and FWHM pulse duration τ_0 is used as an input. Each spectral component is then multiplied with a random phase factor and an inverse Fourier transform is taken producing $A'(t)$, which is then normalized and windowed in time to give:

$$A_{FEL}(t) = A_0 f(t) \frac{\text{Re}[A'(t)]}{\max |\text{Re}[A'(t)]|} \quad (4.7)$$

where A_0 is given below Equation (4.3) and $f(t)$ represents the envelope, here a Gaussian envelope. The electric field of the FEL pulse is then obtained using Equation (4.4). The resulting pulse simulates the partially coherent nature of the SASE pulses produced by an FEL. The average of results from numerical simulations over an increasing number of shots is expected to resemble results similar to those produced during an FEL beam-time. Here, the β -parameters are calculated

Figure 4.7: Anisotropy parameters β_1 (solid line), β_2 (dashed line), β_3 (dotted line) and β_4 (dashed-dotted line) as function of carrier-envelope-phase. The results averaged using a Gaussian distribution for the CEP (c.f., Eq. (4.6)) with widths of (b) $\alpha = 0.2$ (in units of 2π) and (c) $\alpha = 0.4$ are compared with the unaveraged results (a). Peak intensity: 10^{11} W/cm², central frequency: $\omega_0 = |E_{1s} - E_{2p}|$, pulse duration: 1.2 FWHM cycles and photoelectron energy $2\omega_0 - |E_{1s}|$.

using a weighted average

$$\beta_j^{FEL}(E) = \frac{\sum_i^{N_{shots}} \sigma_i(E) \beta_{j,i}(E)}{\sum_i^{N_{shots}} \sigma_i(E)}, \quad (4.8)$$

to account for the photoelectron yield shot to shot.

In Figure 4.8 we compare the results for β_1^{FEL} (left) and β_2^{FEL} (right) as function of photoelectron energy and pulse duration of the Gaussian window used in modeling the FEL pulses, averaged over 10 (panels (c, d)) and 200 (panels (e, f)) FEL shots for each pulse length (i.e., 6,200 calculations in total) with the exemplary results from a single shot (panels (a,b)). A robust distribution for β_2^{FEL} emerges as the number of shots increases, clearly showing the transition from a one- to a two-photon process (the same conclusion holds for β_4^{FEL} , not shown). However, the interference in the photoelectron angular distributions cannot be determined via FEL laser pulses, since the results for β_1^{FEL} and β_3^{FEL} (not shown) average to zero in the transition regime. We note that the generated FEL pulses are not transform-limited and the pulse duration of the Gaussian window used in modeling the pulses does not correspond to that of Gaussian pulses used in the previous subsection ???. Comparing the data presented in Figure 4.8(f) with those in Figure 4.5(d) we estimate that the effective pulse duration of a bandwidth-limited Gaussian pulse with a spectrum corresponding to the average spectrum of the generated FEL pulses is about 0.6 times shorter than that of the Gaussian window.

In this work we have provided theoretical results, obtained from numerical solutions of the time-dependent Schrödinger equation, for the competition between one-photon and two-photon ionization in an ultrashort extreme-ultraviolet laser pulse. We have shown that the transition between the two processes can be observed in the photoelectron angular distributions and the related anisotropy parameters β_i ($i = 1, \dots, 4$) as function of pulse duration, peak intensity, central

Figure 4.8: Anisotropy parameters β_1 (left) and β_2 (right) as function of pulse duration of the Gaussian window used in modeling the FEL pulses and photoelectron energy averaged over 10 (middle row) and 200 (bottom row) partially incoherent free electron pulses as compared to a single shot result (top row). Peak intensity of the Gaussian window: $I_0 = 10^{11}$ W/cm² and central frequency of the spectral distribution $\omega_0 = |E_{1s} - E_{2p}|$.

photon frequency and photoelectron energy distribution. While the even β -parameters exhibit the transition via a change from zero to a finite value, the odd parameters indicate the interference regime. At given photon and photoelectron energies this regime extends over about 0.5 FWHM cycles in duration and a variation by a factor of 2-5 in peak intensity. The impact of three-photon ionization, which becomes available at these broadband pulses as well, is seen at high intensities and large photoelectron energies. Finally, we have considered typical variations in the CEP of ultrashort pulses, e.g. as produced in high harmonic generation, and fluctuating pulse shapes in free-electron laser pulses. It is found that the transition between one- and two-photon ionization can be observed via the even β -parameters in FEL pulses and pulses without CEP stabilization.

4.2 Generalized asymmetry parameters

Introduction

Ultrabright light sources such as free-electron lasers [69] and table-top laser systems based on high-order harmonic generation [58, 11] deliver high-intensity pulses of few- or sub-femtosecond duration. Nowadays, laser pulses with a duration of a few tens of attoseconds have been achieved experimentally [83, 10]. Isolated attosecond pulses or trains of attosecond pulses have been generated from the vacuum ultraviolet to the soft X-ray wavelength regime and the polarization of such pulses can nowadays be controlled. This recent progress in ultrafast laser pulse technology makes it possible to probe, steer and control the dynamics of electrons in atoms, molecules and solids [76, 55, 7, 80, 61, 56]. To name a few examples, the time-resolved measurement of the electron emission in the photoelectric effect has been realized [8, 67, 42, 72, 37]. Using an isolated attosecond pulse or a train of extreme-ultraviolet attosecond pulses to ionize an atom along with

an infrared laser field interferograms have been measured to obtain information about phases of electron wavepackets, an important milestone towards reconstructing the wavefunctions of atoms [63, 47]. By extracting the phase and amplitude via application of photoelectron spectroscopy recently the birth of a photoelectron through a Fano resonance has been observed on the attosecond time scale [25].

Probing atoms and molecules in their ground or excited states with ultrashort laser pulses opens a new regime where several linear and nonlinear ionization pathways compete and interfere [36, 45, 24, 14, 31, 5, 78, 74]. For example, it has been shown how the competition between resonant and nonresonant pathways depends on the pulse width [36]. An important observable are photoelectron angular distributions (PAD), which are measured by detecting the probability for emission of the electron from the target in different directions. Since PADs are determined by the amplitudes and phases of the partial waves of all pathways contributing to the emission, they are practical means to identify the different contributing pathways. A characteristic signature of such interferences are asymmetries in the emission of the photoelectron [81]. In the simple case of photoionization from a single state, anisotropy and asymmetry parameters have been used in the past to identify and analyze interesting physical effects. A significant circular dichroism via the asymmetry in the forward-backward electron emission from bromocamphor molecules induced by circularly polarized light has been identified [6]. Observation of the breakdown of the symmetry in the photoelectron emission of argon has been shown in the region of the Cooper minimum [35]. Interferences between resonant and non-resonant pathways [36] or direct and autoionizing channels [12] can be identified via anisotropy and asymmetry parameters. Other examples can be found in double photoionization [46] or molecular vibrations and chirality [21] and applications range from studies of coherent control [60] to the characterization of ultrashort laser pulses [9].

While studies of quantum systems in a single state are important, very interesting physics arises from the systems in superposition states. Nowadays the most prominent example of a two-level quantum mechanical system is a qubit with its important applications in quantum computation and quantum simulations [66]. Yet, also the internal motion of quantum mechanical systems,

whether it is rotational, vibrational or electronic, is determined via superposition states. In ultrafast science the observation and resolution of such dynamics and, hence, the observation of atoms or molecules in superposition states has always played a central role. Currently, it is the superposition of atomic or molecular electronic states and the related attosecond electron dynamics that is the focus of studies in the field [23, 47, 32, 79]. Perhaps the simplest case of such dynamics is a helium atom in a superposition of $1s$ and $2p_1$ state which results in a wavepacket rotating in a plane around the nucleus with a period of ~ 200 attoseconds. The dynamics in such quantum systems in superposition states can be probed via ionization with an ultrashort laser pulse. Unlike for the ionization of a quantum system prepared in a single state, e.g. the ground state, conventional anisotropy and asymmetry parameters fail to provide comprehensive tools for the analysis of photoionization from atomic superposition states. For example, the simplest case of a competition between one- and two-photon ionization processes can be analyzed using asymmetry parameters if the atom is prepared in the ground state [36, 45, 24, 14, 31, 5, 78, 74]. In contrast, these analysis tools are either not applicable or do not provide a straightforward interpretation for the same processes if the atom is in the superposition of two states. Thus, an extension of the toolbox for the characterization of the states and the identification of competing pathways is desirable. In this paper, we propose a new set of generalized asymmetry parameters which are sensitive to interference effects in the photoionization of atomic systems in superposition states. As we will show these new parameters can be used to identify the interplay of competing linear and nonlinear pathways at low and high intensities, as well as at ultrashort pulse durations. The application and relevance of the parameters is tested using state-of-the-art numerical solutions of the time-dependent Schrödinger equation. Our method provides a new approach to the analysis of experiments dedicated to resolving attosecond electron dynamics.

Generalized asymmetry parameters

We consider a prototypical example in ultrafast science and, more general, in atomic physics, which is schematically shown in Fig. 4.9. An atom in a superposition of two quantum states with

different magnetic quantum numbers m , say the ground (g) and an excited (e) state is probed via ionization by an ultrashort linearly polarized laser pulse. The photoelectron emission is induced by a pulse with central frequency ω tuned to the energy gap of the two states. The broad energy spectrum of an ultrashort Gaussian pulse is schematically depicted in the panels of Fig. 4.9 centered about the energy of the excited state. There are three competing pathways leading to photoelectron emission with energy $2\omega - |E_g|$, where E_g is the ground state energy of the atom: (a) absorption of one photon at ω from the excited state, (b) absorption of two photons with sum frequency 2ω from the ground state and (c) absorption of one photon at 2ω from the ground state. While the ionization from the excited state (a) is the dominant pathway at low peak intensities and long pulse duration, the transitions from the ground state will interfere at higher peak intensities (two-photon process, (b)) and if the bandwidth of the pulse is broad enough (i.e., the pulse duration is sufficiently short, (c)). The exemplary results obtained from the solutions of the time-dependent Schrödinger equation in Fig. 4.9 for the interaction of neon atom, prepared in the superposition of $2p_{-1}$ - and $3d_2$ -states (d) or prepared in the same superposition but including additionally ionization from the $2p_0$ and $2p_1$ ground states (e), with a linearly polarized laser pulse show that the photoelectron angular distributions (PADs) vary significantly as function of pulse duration and peak intensity. The forward-backward asymmetry, often used in the past, cannot be applied to identify the impact of the different pathways in these PADs. Therefore, a new set of asymmetry parameters is needed for photoionization from superposition states with ultrashort laser pulses.

4.2.1 *

Definition

We start by expanding the PAD as a coherent sum of spherical harmonics, assuming the atom is ionized by a linearly polarized pulse aligned along the z -axis as

$$P(\theta, \phi) = \left| \sum_{\ell} C_{\ell}^{m_g} Y_{\ell}^{m_g}(\theta, \phi) + C_{\ell}^{m_e} Y_{\ell}^{m_e}(\theta, \phi) \right|^2 \quad (4.9)$$

where m_g (m_e) are the magnetic quantum numbers of the ground (excited) state in the superpo-

sition, C_ℓ^m is the complex amplitude and $Y_\ell^m(\theta, \phi)$ is the spherical harmonic. The asymmetry in the PADs due to the interference between different channels is related to the relative phase and amplitude of the spherical harmonics. For each spherical harmonic, the sign of the phase is symmetric (asymmetric) across the xy -plane when $\ell + m$ is even (odd), while in the xy -plane the phase is proportional to $e^{im\phi}$.

In the xy -plane there are regions of destructive and constructive interference between the transition amplitudes from the ground and excited state, as illustrated on the left of Fig. 4.10. The regions can be labeled by

$$c_i = \left\lfloor \frac{(\phi - \phi_0)\Delta m}{\pi} \right\rfloor \quad (4.10)$$

where $\lfloor \cdot \rfloor$ is the floor function, ϕ_0 is a reference angle, and $\Delta m = |m_g - m_e|$ ($\Delta m = 3$ in Fig. 4.10, [1]). Setting ϕ_0 at an angle where the interference switches from constructive to destructive, regions of destructive interference signal are labeled by even c_i while odd c_i denote regions of constructive interference. Next we define the following integrals:

$$I_\pm^{\text{even}} = \sum_{\text{even } c_i} \int P(\theta, \phi) d\Omega_{c_i}^\pm \quad (4.11)$$

$$I_\pm^{\text{odd}} = \sum_{\text{odd } c_i} \int P(\theta, \phi) d\Omega_{c_i}^\pm \quad (4.12)$$

where $d\Omega_{c_i}$ is the solid angle for the region c_i in the positive ($z > 0$) or negative ($z < 0$) hemisphere with respect to the xy -plane. In the example in Fig. 4.10 (left) each integral represents the total photoelectron signal in the regions of a specific color (dark blue, light blue, dark red, light red). We now define general asymmetry parameters (GAPs) that account for the relative difference in the regions of constructive and destructive interference:

$$A_p^{\Delta m} \equiv \begin{cases} \left| \frac{(I_+^{\text{even}} + I_-^{\text{even}}) - (I_+^{\text{odd}} + I_-^{\text{odd}})}{I_+^{\text{even}} + I_-^{\text{even}} + I_+^{\text{odd}} + I_-^{\text{odd}}} \right|_{\max(\phi_0)} & \text{even } \gamma \\ \left| \frac{(I_+^{\text{even}} + I_-^{\text{odd}}) - (I_+^{\text{odd}} + I_-^{\text{even}})}{I_+^{\text{even}} + I_-^{\text{even}} + I_+^{\text{odd}} + I_-^{\text{odd}}} \right|_{\max(\phi_0)} & \text{odd } \gamma \end{cases} \quad (4.13)$$

where $\gamma = \ell_e + m_e + \ell_g + m_g + N_p$ with ℓ_g (ℓ_e) are the quantum numbers of the ground (excited) state in the superposition, and $p = (\gamma \bmod 2)$ is the parity of γ . Each parameter $A_p^{\Delta m}$ is related to

a certain total number of absorbed photons, $N_p = N_g + N_e$, where N_g (N_e) is the number of photons absorbed in the transition from the ground (excited) state. We note that GAPs cannot only be defined for ionization of superposition states with a linearly polarized laser pulse along the z -axis, but the definition can be extended, for example, to ionization with a circularly polarized ionizing laser pulse in the xy -plane. In that case $\gamma = \ell_e + m_e + \ell_g + m_g$, the number of photons is not included as both ℓ and m change by 1 for each photon absorbed. Using $\Delta m = |(m_g \pm N_{pg}) - (m_e \pm N_{pe})|$ for right (+) and left (-) handed circular polarized probe pulses, processes with different number of photons involved can be studied by analyzing the signals with different Δm . Here, in the further discussion and applications we however focus on the case of a linearly polarized probe pulse.

To exemplify the significance of the asymmetry parameters we consider the ionization of Ne atom, initially prepared in the $2p_{-1} - 3d_2$ superposition (i.e., $\ell_g = 1$, $m_g = -1$, $\ell_e = 2$, $m_e = 2$; and, hence, $\ell_g + m_g + \ell_e + m_e = 4$), by an ultrashort intense laser pulse. As discussed at the outset, we expect interferences between two kind of pathways depending on the peak intensity and the pulse duration. For an ultrashort pulse at low intensities one-photon transitions from the ground (Fig. 4.9(c), $N_g = 1$) and the excited states (Fig. 4.9(a), $N_e = 1$) will interfere, with $N_p = N_g + N_e = 2$, $\gamma = 6$ and $p = 0$. An exemplary PAD, obtained via numerical TDSE solution in the relevant intensity and pulse duration regimes, is shown at the top of the right column in Fig. 4.10. For even γ the corresponding parameter A_0^3 relates to the difference between the total photoelectron signals in the dark red and light blue shaded regions, as depicted at the top of the middle column of Fig. 4.10. Comparison with the PAD shows that this difference indeed accounts for the asymmetry in the PAD induced by the interference of the transition amplitudes for the one-photon processes from the ground and the excited states. In contrast, due to the dependence of multiphoton transition amplitudes on the intensity of the pulse at longer pulse duration and higher intensities it is expected that the one-photon transition from the excited state (Fig. 4.9(a), $N_e = 1$) interferes with the two-photon absorption from the ground state (Fig. 4.9(b), $N_g = 2$), giving rise to $N_p = 3$, $\gamma = 7$ and $p = 1$ for ionization of $\text{Ne}(2p_{-1} - 3d_2)$. The regions relevant in the calculation of the asymmetry parameter A_1^3 and the corresponding exemplary PAD for the Ne

atom are presented in the bottom row of Fig. 4.10. The comparison indicates the significance of the asymmetry parameter A_1^3 for the detection of the interference at high intensities.

4.2.2 *

Application via numerical simulations

For the application of the GAPs we have considered certain superpositions of two atomic states which are first prepared by a pump pulse and then probed by a linearly polarized pulse at a set time delay such that the relative phase between the two states is determined. In the calculations we have therefore simulated the interaction with the probe pulse only by using numerical solutions of the time-dependent Schrödinger equation (TDSE) for the interaction of a electron in a single-active-electron (SAE) potential with the electric field \mathbf{E} of a linearly polarized laser pulse (aligned along the quantization \hat{z} -axis) in dipole approximation and length gauge (we use Hartree atomic units $e = m_e = \hbar = 1$):

$$i \frac{\partial}{\partial t} \Psi(\mathbf{r}, t) = \left[-\frac{\nabla^2}{2} - \mathbf{E}(t) \cdot \mathbf{z} + V(r) \right] \Psi(\mathbf{r}, t). \quad (4.14)$$

To ensure that the electric field integrates to zero [9], we set the vector potential as: with $A_0 = \frac{c\sqrt{I_0}}{\omega_A}$, $T = \frac{2\pi N}{\omega_A}$, c is the speed of light, I_0 the peak intensity, N the number of cycles in the pulse, φ is the carrier-to-envelope phase (CEP) and ω_A denotes the central frequency of the vector potential which has been frequency corrected [75] to produce an electric field with a central frequency ω . The present calculations are performed utilizing single active electron potentials for He atom and Ne atom [62] with the electron initially prepared in a superposition of the ground and an excited state. The TDSE has been solved by expanding the wavefunction in spherical harmonics (up to $\ell_{max} = 50$ for all relevant m values), as described in [74]. The computations have been performed on a radial grid of 300 a.u. with a grid spacing of 0.05 a.u. using exterior complex scaling on the outer 15 a.u. of the grid. A time step of 0.05 a.u. has been used.

Results and discussion

For our applications we have considered individual superposition states in neon (Fig. 4.11) and realistic superposition states considering all possible initial m_g states of neon and helium atoms (Fig. 4.12). The central frequency of the applied electric field was set to the energy difference of the initially populated field-free states ($\omega_0 = |E_g - E_e|$). To analyze the relevance of both the short-pulse parameter $A_0^{\Delta m}$ and the high-intensity parameter $A_1^{\Delta m}$ calculations have been performed for one- and four-cycle probe pulses (FWHM pulse durations) as function of the peak intensity of the pulse. At the end of each simulation of the time-dependent Schrödinger equation we obtained the photoelectron angular distribution at a given momentum k (corresponding to a photoelectron energy of $E = 2\omega - |E_g|$) by projecting the wavefunction onto the field-free continuum states on the numerical grid. The asymmetry parameters $A_0^{\Delta m}$ and $A_1^{\Delta m}$ are then determined from the numerical PADs using Eq. (4.13).

To exemplify the application and provide basic insights in the relevance of the GAPs, we have first considered superpositions of individual sublevels in different shells of the neon atom as initial state. Fig. 4.11 shows results for the GAPs as a function of peak intensity for interaction of a neon atom, prepared in $(2p_{-1} - 3d_0)$ (a,d), $(2p_0 - 3d_1)$ (b,e), and $(2p_1 - 3d_2)$ (c,f) superpositions. For the results in the top row equal population in the two initial states has been considered, while for those in the bottom row populations, as produced via one-photon excitation by a 50 cycle, 10^{13} W/cm² right handed circularly polarized pump pulse, are used for the initial state (states with populations larger than 10^{-5} are considered, see figure caption for values). The central frequency of the ionizing probe laser pulse is tuned to the energy gap between the field-free ground and excited states.

Overall, except for the results in panel (a) which we will discuss below separately, the short-pulse parameter A_0^1 (solid lines) is large at low intensities and for the shorter of the two pulse durations. This is expected from our discussion above and confirms that the parameter is an indicator for the interference of the one-photon signal from the ground state and the one-photon signal from the excited state. Since both of these signals are first order in intensity, their relative

strengths and, hence, the A_0^1 parameter are independent of intensity at low intensities for a given initial superposition state. As the intensity increases, the relative amplitude of the two-photon ionization channel increases and finally dominates over the one-photon channel from the ground state. This trend is reflected in both the short-pulse and the high-intensity parameters. The increase in A_1^1 , resulting from the interference between the one-photon excited state signal and the two-photon ground state signal, shows in which intensity regime the two-photon signal starts to overtake the short pulse signal. Simultaneously with the increase of A_1^1 we observe a decrease of the A_0^1 signal, in agreement with our physical interpretation of the relevance of the different pathways. Parenthetically, we note the onset of an increase of the A_0^1 parameter at high peak intensities is likely due to pathways involving higher order processes with an even number of total photons.

While the general trends of the two parameters are similar in most of the cases, there is one exception where the details differ significantly. In the case of the $(2p_{-1} - 3d_0)/\sqrt{2}$ superposition (panel a), A_0^1 shows a different trend. It remains constant at low intensities before increasing at higher intensities. As the laser pulse and relative populations are fixed in the top row (a-c) of Fig. 4.11, the change in amplitude and shape of A_0^1 and A_1^1 are caused by changes in the cross-sections of the various states. We, therefore, attribute the different trend in the A_0^1 signal in panel (a) to be due to the dominance of the one-photon transition from the $3d_0$ state at all intensities, since $m = 0$ states are, in general, easier to ionize with a linearly polarized pulse than those with $|m| > 0$. This interpretation is further supported by the results in Fig. 4.11(d) for a superposition with much lower initial population in the $3d_0$ -state. Despite the difference in magnitude of transition amplitudes, now the interference between the one-photon pathways is effective and the general expected trend for the short-pulse parameter A_0^1 is present.

Comparison of the results in the two rows of Fig. 4.11 shows that the intensity at which the transitions in the parameters occur depends on the population in the two states in the initial superposition. Since in the bottom row the populations in the excited states are low, the relative magnitudes of the corresponding one-photon transition amplitudes from the excited states as compared to those from the ground state levels are weaker than for the equally populated superpositions

(top row). Therefore, we observe the impact of the two-photon pathway from the ground state at lower intensities in the results in the bottom row. Additionally, the A_1^1 signal becomes sensitive to changes in pulse length due to the weak signal from the excited state. Thus, the GAPs may also be useful to detect the population ratio in the superposition states. Here, we do not further analyze this feature, but focus on the more general application of the parameters to identify the presence of different ionization pathways.

So far, in Fig. 4.11 we considered simple albeit somehow artificial superposition states restricted to certain sublevels of two shells in the neon atom. Now, we extend our analysis to three different initial states as they can be generated with right-handed circularly polarized pump laser pulses: (a) one-photon excitation of helium atom to the $2p_1$ state leading to $(1s - 2p_1)/\sqrt{2}$ superposition, (b) three-photon excitation of neon atom to the $3d$ shell, leading to an initial state consisting of a superposition with equal population in $2p_{-1}$ and $3d_2$ along with populated $2p_0$, and $2p_1$ states (note, that the latter two $2p$ states cannot be excited by the absorption of three right-handed circularly polarized photons to the $3d$ shell), and (c) one-photon excitation of neon atom to the $3d$ shell leading to the combination of the three superposition states analyzed separately in the bottom row of Fig. 4.11. In Fig. 4.12, we present results for the GAPs of the corresponding calculations. The initial superpositions in case of the helium data (a) and the neon data in panel (b) consist of just one state in the excited shell and show the same general trends as those in the majority of the panels of Fig. 4.11 with the decrease of $A_0^{\Delta m}$ along with the increase of $A_1^{\Delta m}$ occurring in a certain intensity regime. The transitions in helium occur at a higher peak intensity due to the more tightly bound helium ground state, which is harder to ionize. The overall trends of the results in Fig. 4.12(c) for the more complex initial superposition, consisting of six states in the $2p$ - and the $3d$ -shell of neon. The one-cycle pulse data are similar to those discussed before, providing the same information about the impact of the two-photon transition from the ground state. However, the A_1^1 parameter, particularly at the longer pulse duration, shows an additional interference structure in the transition regime. It is likely that this is due to an interference between transitions originating from two excited states differing by $\Delta m = 1$, here between one-photon ionization signals from $3d_0$

and $3d_1$ as well as from $3d_1$ and $3d_2$. Although the number of absorbed photons in these transition is not 3, the resulting γ has the same parity as the signal from a $2p_m - 3d_{m+1}$ state.

The high-intensity asymmetry parameter $A_1^{\Delta m}$ is not only indicative of the general features concerning the interferences between the pathways discussed above, but also provides insights in more subtle aspects. In the top row of Fig. 4.11 the maximum of the asymmetry parameter $A_1^{\Delta m}$ occurs at the same intensity independent of the pulse duration. This is due to the fact that in the calculations the central frequency was set to the energy difference of the initially populated states. In this case the center of the photoelectron energy distributions due to the one-photon ionization from the excited state and the two-photon transition from the ground state nearly coincide[2]. If the frequency is detuned from the resonance, the position of maximum interference strongly depends on the pulse duration. Due to the larger spectral width of the pulse at shorter pulse duration, the interference between the channels becomes most effective at higher intensities than the longer pulse duration results, at which the photoelectron distributions from the two channels have less overlap. This effect is seen in the results in Fig. 4.13 for photoionization at a central frequency of 1.2 times the energy difference between the $1s$ - and $2p_1$ -states in helium atom.

Finally, it is important to consider variations in the laser parameters relevant for an application of the generalized asymmetry parameters in an experiment. Typically, the peak intensity of the applied laser pulse may vary from shot to shot as well as over the interaction volume. The results in Fig. 4.11 and Fig. 4.12 show that the two GAPs vary rather slowly as a function of peak intensity. Thus, we can expect that variations in intensity in an experiment will not impact the results significantly. Another parameter that is usually difficult to control is the CEP of a laser pulse, which typically may become most important for ultrashort pulses. In the present study the high-intensity A_1^1 parameter is independent of variations in CEP. To study the dependence on the CEP for the short-pulse low-intensity asymmetry parameter A_0^1 we have obtained results as a function of the CEP and averaged the results about a given value φ_0 using a Gaussian distribution

of width α (in units of 2π) as:

$$A_p^{\Delta m}(I, T; \alpha) = \frac{\sum_i \exp \left[-\frac{1}{2} \left(\frac{|\varphi_i - \varphi_0|}{2\pi\alpha} \right)^2 \right] \sigma(\varphi_i) A_p^{\Delta m}(\varphi_i, I, T)}{\sum_i \exp \left[-\frac{1}{2} \left(\frac{|\varphi_i - \varphi_0|}{2\pi\alpha} \right)^2 \right] \sigma(\varphi_i)}, \quad (4.15)$$

where $\sigma(\varphi_i)$ is the total ionization probability at CEP φ_i . In the calculations we have assumed that the pump pulse (for the preparation of the initial state) has the same CEP as the probe pulse. The comparison of the results for different averages in Fig. 4.14 with the results for fixed CEP (solid line) shows that for He atom the short-pulse asymmetry parameter A_0^1 is indicative for the interference up to fluctuations of about $\pi/2$ in the CEP.

Summary

In summary, we have introduced a set of generalized asymmetry parameters (GAPs) which characterize the interference of linear and nonlinear pathways to ionization of atoms, prepared in superposition states, due to the interaction with a linearly polarized intense ultrashort laser pulse. These parameters may provide a new tool to analyze data in attosecond experiments. The relevance of the parameters is demonstrated via the results of numerical simulations of ionization of helium and neon atom. The impact of short pulse and nonlinear effects, as they arise in experiments with free-electron lasers and high-order harmonic generation, is shown. The dependence on the central frequency of the applied laser pulse and the impact of variations of laser parameters, such as the peak intensity and the carrier-to-envelope phase, are analyzed and discussed.

4.3 Wavefunction reconstruction method

The availability of attosecond light sources at wavelengths from the vacuum ultraviolet (VUV) and extreme ultraviolet (EUV) to the soft X-ray regime via the technologies of free electron lasers (FEL) [69] and high-order harmonic generation (HHG) [58, 11] has opened a new regime of ultrafast measurements in atomic and molecular physics. Laser pulses of duration as short as a few tens of attoseconds have been demonstrated experimentally [83, 10] and enabled the observation of electron dynamics (for recent reviews, see [76, 55, 7, 61, 82, 56]). One example is the time-resolved

measurement of the photoelectric effect in atoms and solids [8, 67, 42, 72, 37]. Electron emission from the target has been also temporally resolved for a transition of the electron into the continuum through excited state resonances [71, 65, 22], autoionizing states [39, 13, 3], Fano resonances [40, 44, 25, 12] and for correlated electron emission [57, 54, 50]. Electron wavepacket dynamics in superposition states of atoms and molecules has been another focus of attosecond time-resolved studies, either for single valence electron motion [23, 47, 32, 30, 41, 79, 43, 4, 26, 77, 59, 28] or correlated two-electron dynamics [33, 17, 52].

Recently, the application range of attosecond laser pulse technology has been extended by the capability to control the polarization of the emitted light in high-order harmonic generation and free electron lasers. The physical principle to produce circularly polarized high-order harmonics has been proposed and applied first two decades ago [15] while efficient phase matching in the EUV and soft X-ray regime [18, 16, 29] and the control of the polarization stage [34] has been demonstrated more recently. Similarly, free electron laser light with variable polarization has become available [70, 48]. The potential to control the polarization and helicity of light generated by HHG and FELs extends the range of accessible states and transition pathways during photon absorption. States with varying orbital angular momentum and magnetic quantum number can be excited during the interaction with the pulses. In turn, the helicity of the light pulses can be used to selectively prepare superpositions of states in atoms or molecules with a variety of combinations in the quantum numbers (principal, orbital angular momentum, magnetic) on an ultrafast time scale.

One of the simplest cases of a superposition of atomic states with different orbital angular momentum and magnetic quantum numbers is that of a helium atom in the $1s$ and $2p_1$ states. It results in an ultrafast electron dynamics given by a wavepacket rotating in a plane around the nucleus with a period of ~ 200 attoseconds. We study this dynamics via ionization with an ultrashort linearly polarized laser pulse as a function of time delay from the instant of preparation of the atomic superposition state. Furthermore, we analyze how the photoelectron angular distributions can be used to reconstruct the initial electronic wave packet. The concept is based on the idea to utilize quantum beating signals, where the imaged wave packet is interfered with a

reference wave, to reconstruct a wave function [53, 51, 47, 43, 59, 38]. Accounting for the phase accumulation, ionization cross sections, and characterization of the reference wave packet that is used in the measurement is a non-trivial task. In this work we present a method for circular wave packet reconstruction on the attosecond time scale that utilizes perturbation theory. Additionally, we perform a sensitivity study to show the impacts of noise produced in an experiment and the limits in peak laser intensity on the reconstruction method. Finally, we consider the extension of the method to the imaging of wave packets consisting of superpositions of more than two states.

The rest of the paper is organized as follows: In section ?? we first present and discuss the ionization scheme on which the reconstruction method is based. Then we briefly review the methods for the numerical solution of the time-dependent Schrödinger equation and the perturbation theory formalism used for the reconstruction algorithm. In section ?? we present the application of the method to the reconstruction of a circular wavepacket in helium atom. Aspects of the error analysis with respect to the accuracy of the observation of the PADs and the variation of the laser parameters will be presented. Furthermore, the impact of different pathways on the reconstruction process will be studied. Finally, we briefly discuss the extension of the method to superpositions of more than two states along with results for a specific three-state superposition. The paper ends with a brief summary. We use Hartree atomic units $e = m_e = \hbar = 1$ if not mentioned otherwise.

As prototypical example we consider a helium atom in a $1s - 2p_1$ superposition, which represents a circular wave packet rotating around the nucleus. Fig. 4.15(a) shows the dynamics via isosurfaces of the wave function (i.e., $|r\Psi|^2$) rotating in the $x - y$ plane on an attosecond time scale. To characterize the motion, and in turn reconstruct the wave function, we expand the initial wave function in the eigenbasis of stationary states and write the wave function at some time t as:

$$\Psi(\mathbf{r}, t) = a_0\psi_0(\mathbf{r}, t) + \sum_{j=1}^{N-1} a_j e^{i\theta_j} \psi_j(\mathbf{r}, t) \quad (4.16)$$

where a_j is a positive real number, θ_j is a relative phase, and $\{\psi_j = \Psi_{nlm}; j = 0, \dots, N - 1\}$ is the eigenstate basis. While the basis may contain an infinite number of eigenstates, for practical means in the numerical calculations and any application it has to be truncated at some finite number

N . Thus, the wave function depends on $N - 1$ phases and N amplitudes since the global phase is not a physically relevant quantity. In this framework, all time dependence is contained in the states $|\psi_j(t)\rangle$ and the initial wavefunction is completely reconstructed if all a_j and θ_j for $j \geq 1$ are obtained since a_0 is fixed by the normalization and we set the phase of ground state $|\psi_0\rangle$ to zero.

In the reconstruction scheme that we consider the electron dynamics is probed via ionization by an intense ultrashort laser pulse as a function of time delay from the instant of preparation of the atomic superposition states. In the scheme predictions of first- and second-order perturbation theory (PT) are used to determine the unknown phases and amplitudes from the photoelectron angular distributions (PADs). The latter may be determined in an experiment but in this theoretical study we utilize ab-initio numerical calculations. For the case of a helium atom in a $1s - 2p_1$ superposition, we apply a probe laser pulse linearly polarized along the x -axis and detect the photoelectron angular distribution in the $x - y$ plane as a function of the angle φ from the x -axis as shown in Fig. 4.15(b). The absorption of a photon will induce transitions with $\ell \rightarrow \ell \pm 1$ and $m \rightarrow m \pm 1$ due to the selection rules. The pathways from the ground (c) and the excited state (d) are shown in Fig. 4.15. The solid arrows represent the pathways for the transitions at the central frequency of the probe pulse. I_p is the ionization potential and the ovals indicate possible resonances. Since we analyze photoelectron emission induced by ultrashort pulses, we need to consider additional pathways due to the broad bandwidth of the pulse [74]. These pathways are the ionization from the ground state with a single photon and the two-photon transition from the excited state, which are represented by the dotted arrows in Fig. 4.15. Since states in the continuum with the same energy and quantum numbers can be reached via different pathways, the photoelectron angular distribution will change in both shape and yield as the relative amplitudes and phases of each signal varies.

In order to test the applicability and limits of the reconstruction method we use numerical solutions of the time-dependent Schrödinger equation (TDSE) as substitute for actual measurements of the photoelectron angular distributions. We consider the TDSE in length gauge and single-active

electron approximation:

$$i\frac{\partial}{\partial t}\Psi(\mathbf{r},t) = \left[-\frac{\nabla^2}{2} - \mathbf{E}(t) \cdot \mathbf{x} + V(r) \right] \Psi(\mathbf{r},t) , \quad (4.17)$$

where $V(r)$ is a single-active electron potential for helium atom given by [62]:

$$V(r) = -\frac{1}{r} - \frac{e^{-2.0329r}}{r} - 0.3953e^{-6.1805r} . \quad (4.18)$$

giving a ground state energy of -0.944409 a.u. and a $2p$ energy of -0.12847 a.u.

For the solution we have expanded $\Psi(\mathbf{r},t)$ in spherical harmonics up to $l_{max} = |m_{max}| = 20$ and discretized the radius using fourth order finite difference. The wavefunction has been propagated in time with a time step of 0.01 a.u., on a grid with spacing of 0.05 a.u., maximum radius of 300 a.u., and exterior complex scaling on the outer 30 a.u. of the grid utilizing the Crank-Nicolson method for time propagation. The numerical code has been tested against previously used codes as well as results from numerical calculations published in the literature [68].

To avoid unphysical effects in the numerical simulations we make sure that the electric field integrates to zero by setting the vector potential as [9]

$$A(t) = \begin{cases} A_0 \sin^2\left(\frac{\pi t}{T}\right) \sin\left(w_A\left(t - \frac{T}{2} + \tau_d\right)\right) : & 0 \leq t \leq T \\ 0 : & \text{else} \end{cases} \quad (4.19)$$

where $A_0 = \frac{c\sqrt{I}}{\omega_A}$, $T = \frac{2\pi N}{\omega_A}$, τ_d is the pulse delay, c is the speed of light, I is the peak intensity, N is the number of cycles in the pulse, and ω_A is the central frequency of the vector potential. ω_A is determined such that the spectral distribution of the E -field matches the given physical central frequency ω_E [75]. The E -field is obtained by

$$E(t) = -\frac{1}{c} \frac{\partial}{\partial t} A(t) . \quad (4.20)$$

Once the wavefunction has been propagated to the end of the pulse we have obtained the photoelectron angular distribution by projecting onto numerical continuum states. For an arbitrary radial potential $V(r)$ we propagate the radial Schrodinger equations for a given ℓ from $r = 0$ to

r_{max} . Boundary conditions and scattering phase shifts are accounted for via setting $\phi_{k,l}(r=0) = 0$ and using the asymptotic solution to the Coulomb wave functions

$$\phi_{kl}(r \gg 1) \rightarrow \sin \left[kr - \frac{l\pi}{2} + \frac{Z}{k} \ln(2kr) + \delta_{kl} \right]. \quad (4.21)$$

To normalize the amplitude at $r = r_{max}$ we set

$$\mathcal{N} = \left[\frac{1}{\sqrt{|\phi_{kl}(r)|^2 + \left| \frac{\phi'_{kl}(r)}{(k + \frac{Z}{kr})} \right|^2}} \right]_{r=r_{max}} \quad (4.22)$$

and determine the phase shift δ_{kl} by

$$\delta_{kl} = \left[\arg \left(\frac{i\phi_{kl}(r) + \frac{\phi'_{kl}(r)}{(k + \frac{Z}{kr})}}{(2kr)^{iZ/k}} \right) - kr + \frac{l\pi}{2} \right]_{r=r_{max}}. \quad (4.23)$$

The photoelectron angular distribution is then obtained as

$$P_{\text{TDSE}}(k, \theta, \phi) \propto \left| \sum_{l,m} Y_{l,m}(\theta, \phi) \int e^{-i\delta_{kl}} (i)^l \phi_{kl}^*(r) \Psi(\mathbf{r}, t) dr \right|^2. \quad (4.24)$$

The PT results are then used to obtain a residual

$$R(\mathbf{a}) = \sum_{k,\phi,\tau} \left| \frac{P_{\text{TDSE}}}{\sum_{k,\phi,\tau} |P_{\text{TDSE}}|} - \frac{P_{\text{PT}}(\mathbf{a})}{\sum_{k,\phi,\tau} |P_{\text{PT}}(\mathbf{a})|} \right|^2 \quad (4.25)$$

where P_{TDSE} and P_{PT} are the TDSE and PT photoelectron distributions for all utilized final momenta, time delays, and detection angles. The state vector \mathbf{a} that minimizes $R(\mathbf{a})$ gives the reconstructed wavefunction. The normalization maintains the relative yields at each final momentum.

In Fig. 4.16 we show how the photoelectron angular distribution varies as a function of time delay between the instant of preparation of the atomic superposition states and the center of the probe pulse. Comparison of the TDSE results for a two-cycle (left column) and a ten-cycle (right column) laser pulse at three peak intensities ranging from 10^{10} W/cm² (bottom row) over 10^{12} W/cm² (middle row) to 10^{14} (top row) W/cm² is shown. In these calculations the photon energy

ω_E has been set to the energy difference between the initially equally populated field-free $1s$ and $2p_1$ states in helium atom $(|1s\rangle + |2p_1\rangle)/\sqrt{2}$. The angular distribution is taken at photoelectron energy $E = 2\omega_E - I_p$, where ω_E is the central photon energy and I_p is the ionization energy.

At the lowest intensity (Fig. 4.16, bottom row) we observe that the two-cycle signal varies significantly which is due to the interference between the one-photon ionization channels from the excited state and the ground state. The pathway from the ground state provides a significant contribution to the electron emission due to the broadband spectrum of the ultrashort two-cycle pulse [74, 73]. Thus, as the time delay varies, the relative phase of the ground and excited states changes producing a quantum beating. In contrast for the longer ten-cycle pulse the spectrum of the pulse is more narrow. Consequently, the contribution from the one-photon pathway from the ground state is much smaller and, hence, the PAD for the ten-cycle pulse at the lowest intensity shows minimal variation as a function of time delay since it is dominated by the ionization of the excited state.

As the intensity is increased, the relative contribution of the two-photon ionization pathway from the ground state increases since the power dependence of the signals scales with the number of photons absorbed. Since this channel depends on the absorption of photons at the central energy the significance of the contribution does not depend on the pulse duration. As a result, we observe that at the largest intensity considered in Fig. 4.16 (top row) that both the two- and the ten-cycle PADs vary strongly as function of the time delay, indicating the interference between the one-photon ionization from the excited state and the two-photon ionization from the ground state.

To demonstrate the reconstruction method the errors in reconstructing the phase and amplitude of the superposition state $(|1s\rangle + |2p_1\rangle)/\sqrt{2}$ in helium atom as a function of peak intensity are shown in Fig. 4.17. The reconstruction is based on PADs taken for 20 time delays over one period of quantum beating $\tau = 2\pi/|E_{2p_1} - E_{1s}|$. A comparison is shown between results in which either the full PAD in the $x - y$ plane via signals at 6,285 equally spaced angles (a) or only the signals in the forward-backward direction along the polarization axis of the probe pulse (b) is used. The phases and amplitudes have been determined by minimizing $R(\mathbf{a})$, Eq. (4.25). The final results for

$R(\mathbf{a})$ as a function of peak intensity are shown in the insets of Fig. 4.17.

The results in panel (a) show that if the full $x - y$ plane and 20 time samples are used, the reconstruction method reproduces the initial state up to peak laser intensities of about 10^{13} W/cm². The increase of the errors at intensities larger than 10^{13} W/cm² indicates that higher-order processes not described by the first- and second-order PT method begin to contribute leading to the breakdown of the present reconstruction method. For a two-state superposition just two amplitudes and the relative phase have to be determined. Using the full PAD with several thousand signals is oversampling for the reconstruction method. We therefore limit the signal used for the reconstruction to the forward-backward direction along the polarization direction. The corresponding reconstruction (b) does not change the results for the absolute error as function of intensity up to the breakdown at about 10^{13} W/cm².

The reconstruction depends on the effective interference of at least two amplitudes to have a quantum beating. In the full reconstruction we consider the contributions from four pathways (one- and two-photon transitions from ground and excited states). It is interesting to ask which pathways contributes effectively besides the one-photon transition from the excited state. To study this question, we have deliberately neglected individual amplitudes in the reconstruction. The results of these calculations are shown in Fig. 4.18 for the reconstruction based on the full $x - y$ plane and 20 time samples.

For the results in Fig. 4.18a we utilized all amplitudes except the two-photon signal from the excited state. At intensities less than 10^{13} W/cm², the reconstruction matches the full data (Fig. 4.17(a)). At higher intensities, the two-cycle results deviate which agrees with the expectation that the two-photon signal from the excited state should have the largest impact at ultrashort pulse durations and high intensities.

Next, we have removed the one-photon signal from the ground state and the two-photon signal from the excited state from the reconstruction. The transition amplitudes are expected to be effective in broad bandwidth pulses or for ultrashort pulse durations. In agreement with this expectation the reconstruction errors in Fig. 4.18b match the full five- and ten-cycle data almost

perfectly. The two-cycle data, however, deviates from the full results and those in Fig. 4.18(a) at 10^{10} W/cm² and above 10^{13} W/cm², showing the influence of the two ultrashort pulse pathways. At the lowest intensity it is the one-photon signal from the ground state that provides a dominant contribution to the PAD, leading to the deviation at 10^{10} W/cm². At intensities above 10^{13} W/cm², the additional exclusion of the one-photon signal leads to a better reconstruction than for the full data and when the two-photon pathway from the excited state is neglected. This can indicate that inadvertently the two ultrashort amplitudes have an opposite effect on the reconstruction or that an even higher-order amplitude is more dominant than the lower-order processes.

We have also studied how the reconstruction depends on the number of PAD samples over time. To this end, we present in Fig. 4.19 the errors in amplitude and phase based on a reconstruction using just two PADs over one period of quantum beating $\tau = 2\pi/|E_{2p_1} - E_{1s}|$. If the full PAD in the $x - y$ plane is used (panel (a)) the reconstruction method remains successful over the same intensity regime as before. However, when the available signals are limited to the forward-backward direction and only two time delays are used as samples (panel (b)), the data are insufficient for a one-to-one mapping between the initial state and the obtained photoelectron signal and the reconstruction fails at nearly all peak laser intensities. This is due to the fact that for just two time samples the normalization leads to a greater chance that multiple values for amplitudes and the relative phase produce a given signal.

For the reconstruction in Figs. 4.17 and 4.19 we have used results from TDSE calculations up to machine precision. Detectors in experiment do not operate with the same precision and we have therefore studied how less accurate data may impact the success of the reconstruction. To this end, we have deliberately added random noise at a certain percentage level of the maximum signal in the PADs to the TDSE data. In Fig. 4.20 we show the results for the reconstruction with added noise at the (a) 1% and (b) 10% level using the signals from the full $x - y$ plane and 20 time samples. It is seen that an accuracy of detection at the 1% level is sufficient to reconstruct the wavefunction with the same error as in the full calculation with TDSE data at machine precision (Fig. 4.17(a)). Similar results and conclusions have been obtained for the other cases presented

in Figs. 4.17 and 4.19. We expect that this limit for the detection accuracy can be achieved in a photoelectron measurement.

So far, we have considered a special case with equal population in the two states and the central frequency tuned to the energy difference between the two states. We will now study deviations from this special case. First, we consider a laser pulse detuned from the energy difference between the two equally populated states. We have calculated the photoelectron distribution at $E = \omega_E - |E_e|$, where E_e is the energy of the excited $2p_1$ -state. Given a sufficiently broad spectral range, i.e. sufficiently short pulse, the one-photon ground state signal (peaking at about $E = \omega_E - |E_g|$) at low intensities will interfere with the excited state signal creating the same quantum beating as before allowing for the reconstruction process to work. In Fig. 4.21 we show the reconstruction results for a laser with central frequency of $\omega_E = 0.8\omega_0$ (a) and $\omega_E = 1.2\omega_0$ (b). There are slightly larger errors in the $\omega_E = 0.8\omega_0$ results, the superposition however has been still successfully reconstructed at intensities up to 10^{13} W/cm² in the same way as in the resonant case.

To show that the reconstruction works for a two-state superposition with arbitrary unknown amplitudes and phases, we have performed a ‘blindfold’ of the states randomly. The random values were held unknown and were only accessed to obtain the final error at the end of the reconstruction procedure. The results for this ‘blindfold’ experiment in Fig. 4.22 show that the reconstruction is successful leading to the same low errors as in the other cases studied.

We have further considered variations in the laser parameters relevant for an application of the reconstruction method in an experiment. Typically, the peak intensity of the applied laser pulse may vary from shot to shot as well as over the interaction volume. Another parameter that is usually difficult to control is the carrier-to-envelope phase (CEP) of a laser pulse, specifically for ultrashort pulses. To study the impact on the reconstruction, CEP (Fig. 4.23(a)), peak intensity (Fig. 4.23(b)), and both CEP and peak intensity (Fig. 4.23(c)) have been varied randomly within a certain percentage in the TDSE results. The results in Fig. 4.23 show that the reconstruction method still works well up to 10% variation in both parameters before significant errors occur.

Finally, we briefly consider the extension of the reconstruction method to a superposition of

more than two states. The ionization scheme shown in Fig. 4.18 can be applied to each excited state in the superposition separately, taking the waves generated via one- and two-photon transitions from the ground state as reference. For the reconstruction measurement of a PAD at separate energies for each excited state in the superposition is required. Using PT results residuals $R(\mathbf{a})$ (Eq. 4.25), taking into account both final momenta to reconstruct the wavefunction as before.

To test the extension of the method we have considered the helium atom in the $(|1s\rangle + |2p_1\rangle + |3p_1\rangle)/\sqrt{3}$ superposition. Applying a probe laser pulse at central photon energy tuned halfway between the $|2p_1\rangle$ - and $|3p_1\rangle$ -state and measurement of PADs at both $E = \omega - |E_{2p}|$ and $E = \omega - |E_{3p}|$. The results of the reconstruction, based on PADs in the full $x - y$ -plane taken at 20 time delays, are shown as function of peak intensity for different pulse durations in Fig. 4.24. The results show that a similar degree of accuracy in the reconstruction as for the two-state superposition is achieved within the same intensity limits. The example indicates that the present method may be extended to even more complex wavepackets and electron dynamics.

Extension of the reconstruction method to more complex superpositions will require attention to the interference with the ground state signal and the increased dimensionality of the minimization space. Since the minimization process appears to be convex, a standard minimization algorithm, like conjugate gradient, may be sufficient for an efficient reconstruction. For each additional state in the interference scheme, the signal at the photoelectron energy chosen must include interference with at least one other state. This can be achieved if all transitions from the excited states interfere with that from the ground state by using a short pulse. If only longer pulses are available, coupling over many pairs of states reduces the required bandwidth for a reconstruction. Finally, due to the selection rules some initial states do not generate a signal in the xy -plane. In this case it may be required to utilize a full 4π -PAD for reconstruction of the corresponding superposition.

We have studied a method to reconstruct a wavepacket in an atom, consisting of a superposition of states, based on the measurement of photoelectron angular distributions as a function of time delay with respect to the preparation of the wavepacket. The concept utilizes quantum beating signals due to interferences between the one-photon transition from the excited state with reference

to one- and two-photon transitions from the ground state as well as two-photon transition from the excited state. For the reconstruction results from first- and second-order perturbation theory for the PADs are used to determine the phases and amplitudes of the states in the superposition via a minimization process.

The method has been analyzed via application to the superposition of the ground and one or two excited states in helium atom. The corresponding wavepackets represent charge migrations on the attosecond time scale in form of ring currents around the helium core. PADs are simulated via solutions of the time-dependent Schrödinger equation in the single-active-electron approximation. It is shown that the method can be applied for resonant and off-resonant central photon energies. Via an error analysis of the reconstruction method accurate reconstruction has been demonstrated up to peak intensities of 10^{13} W/cm² and pulse durations of ten cycles. The impact of the ultrashort pathways (one-photon transition from the ground state and two-photon transition from the excited state) as reference signals at the different intensities and pulse durations has been analyzed. Furthermore, our work has shown that the reconstruction requires an accuracy of the PAD measurement of about 1% of the maximum signal and stabilization of the peak intensity and carrier-to-envelope phase up to a variation of 10%. Finally, we have discussed the extension of the concept to a superposition of more than two states. Results have been presented for a specific three-state superposition in helium atom, showing a similar level of accuracy as for the two-state superposition.

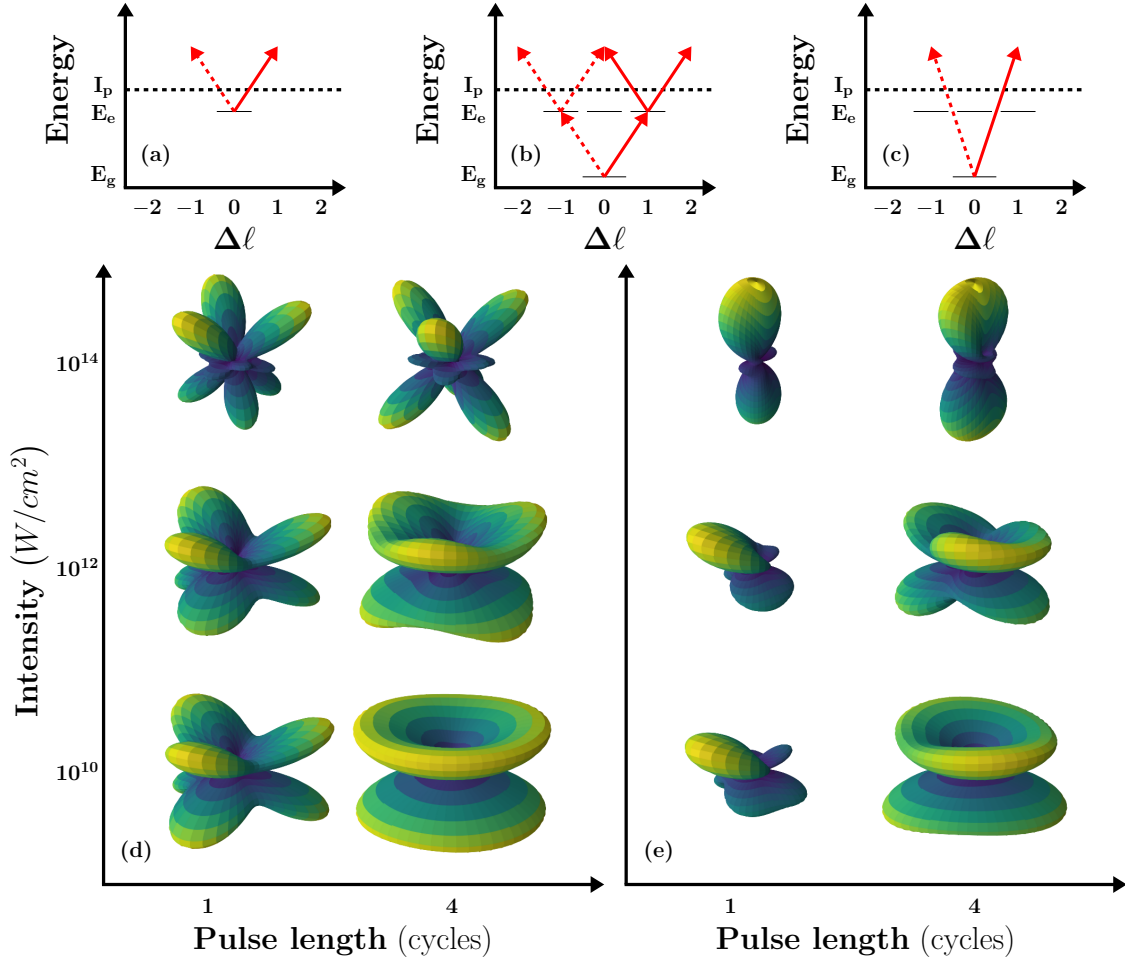


Figure 4.9: (a-c): Ionization pathways effective in different intensity and pulse length regimes. (d) Photoelectron angular distributions for ionization of neon atom, prepared in $2p_{-1} - 3d_2$ superposition, as function of intensity and pulse length. (e) The same as (d) including additionally ionization from the $2p_0$ and $2p_1$ states.

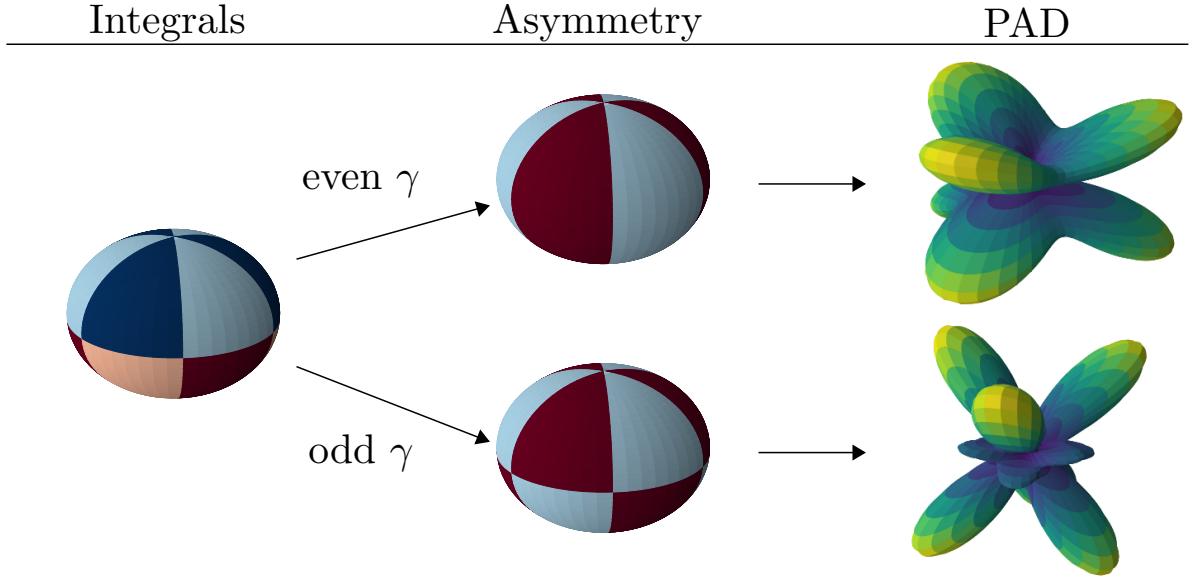


Figure 4.10: Conceptual illustration of GAPs (for $\Delta m = 3$). Left: Integrals $I_{\pm}^{even/odd}$, Eqs. (3,4), are defined over regions of constructive and destructive interference, indicated by different colors (dark blue, light blue, dark red, light red), in xy -plane. Middle: GAPs are constructed based on the parity of the parameter $\gamma = l_e + m_e + l_g + m_g + N_p$ from the integrals over the regions denoted by a certain color (light blue, dark red). Right: Exemplary PADs displaying the asymmetry captured by the parameters for even and odd γ .

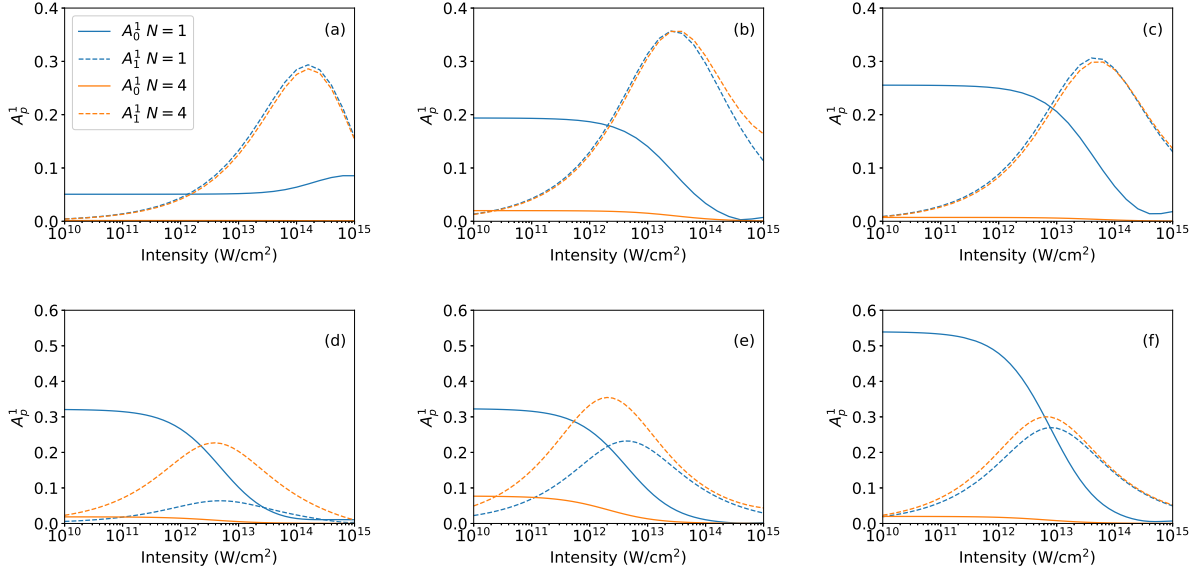


Figure 4.11: Generalized asymmetry parameters A_0^1 (solid lines) and A_1^1 (dashed lines) as function of intensity for ionization of superpositions of $2p_{-1} - 3d_0$ (a), $2p_0 - 3d_1$ (b), and $2p_1 - 3d_2$ (c) in neon atom with initial populations of 0.5 for each state (top row). Results in bottom row for superpositions with populations of $P_{2p_{-1}} = 0.98, P_{3d_0} = 0.02, P_{4s_0} = 0.00057$ (d), $P_{2p_0} = 0.94, P_{3d_1} = 0.06$ (e), and $P_{2p_1} = 0.88, P_{3d_2} = 0.12$ (f). Results have been obtained for one-cycle (blue lines) and four-cycle (orange lines) pulses at photoelectron energy $E = 2\omega - I_p$.

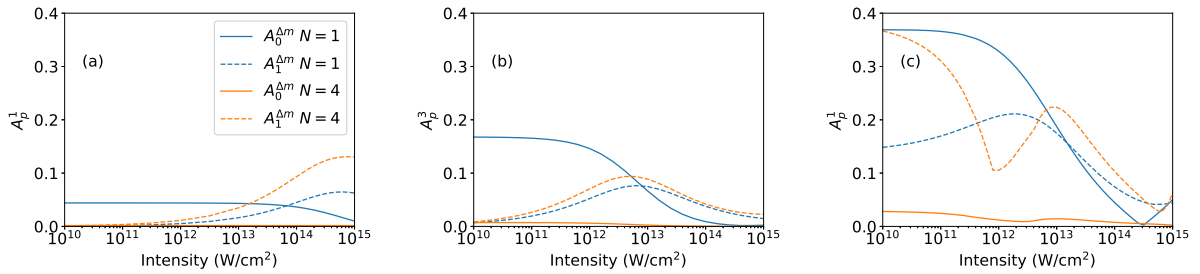


Figure 4.12: Same as Fig. 4.11 but for superpositions generated by a right-handed circularly polarized pulse via one-photon transition in helium atom (a), three-photon transition in neon atom (b), and one-photon transition in neon atom (c) (for details see text).

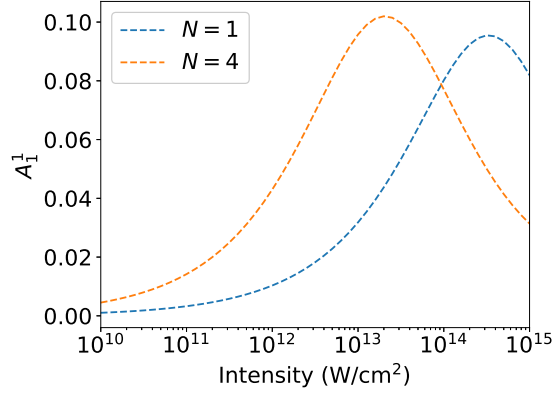


Figure 4.13: Asymmetry parameter A_1^1 for ionization of helium atom ($1s-2p_1$) with one- and four-cycle pulses at central frequency $\omega = 1.2\omega_0$.

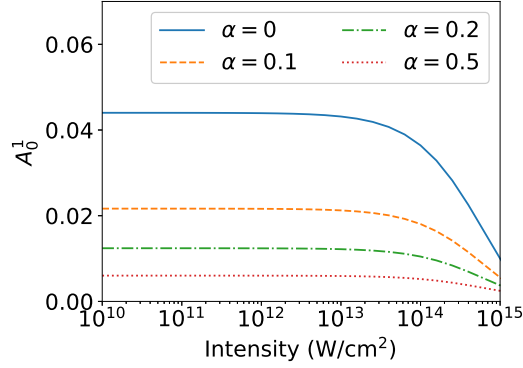


Figure 4.14: Asymmetry parameter A_0^1 for ionization of helium atom ($1s-2p_1$) with one-cycle pulses at central frequency ω_0 . Results of averages over different Gaussian distributions of CEP with width α are compared with those at fixed CEP ($\alpha = 0$, solid line).

Figure 4.15: (a) Isosurfaces of the $1s - 2p_1$ wave function ($|r\Psi|^2$ is shown) evolving in time. (b) Ionization scheme in the $x - y$ plane. The laser polarization along the x -axis is depicted in red, the direction of the ionized electron is shown in orange, and the charge migration is shown in yellow. Selection rules for ground state signal (c) and excited state signal (d). The solid lines illustrate the transitions of photons absorbed at the central frequency and the dashed lines show the pathways for short pulse effect due to the large bandwidth of an ultrashort pulse.

Figure 4.16: Results of TDSE calculations for photoelectron angular distributions as a function of time delay for ionization of $1s - 2p_1$ superposition with ultrashort two-cycle (left column) and ten-cycle (right column) laser pulse with peak intensities of 10^{14} W/cm² (top row), 10^{12} W/cm² (middle row), and 10^{10} W/cm² (bottom row).

Figure 4.17: Errors in amplitude (solid lines with symbols) and phase (dashed lines with symbols) for two-state reconstruction using PADs generated with laser pulses at two, five and ten cycle pulse duration. In the insets the residual $R(\mathbf{a})$ is shown. The reconstruction is based on PADs at 20 time samples ($\Delta t = \tau/20$) using PADs in the full $x - y$ plane (a) and photoelectron signals in forward-backward direction (b).

Figure 4.18: Same as Fig. 4.17(a) but neglecting (a) only the two-photon transition from the excited state and (b) both the one-photon transition from the ground state and the two-photon amplitude from the excited state in the reconstruction.

Figure 4.19: Same as Fig. 4.17 but based on PADs at just two time delays ($\Delta t = \tau/2$).

Figure 4.20: Same as Fig. 4.17(a) but with accuracy of PADs limited to (a) 1% and (b) 10% of maximum value.

Figure 4.21: Same as Fig. 4.17 but for ionization at a detuned photon frequency of $\omega = 0.8\omega_0$ (a) and $\omega = 1.2\omega_0$ (b). Reconstruction is based on full PADs in $x - y$ plane at 20 time delays.

Figure 4.22: Same as Fig. 4.17 but for an arbitrary unknown two-state superposition. Reconstruction is based on full PADs in $x - y$ plane at 20 time delays.

Figure 4.23: Same as Fig. 4.17 but at peak intensities of 10^{11} W/cm² (blue lines) and 10^{13} W/cm² (orange lines) and pulse duration of 2 cycles. Results are shown as a function of variation of (a) carrier-to-envelope phase, (b) peak intensity and (c) both carrier-to-envelope phase and peak intensity. Reconstruction is based on full PADs in $x - y$ plane at 20 time delays.

Figure 4.24: Same as Fig. 4.17(a) but for the superposition $(|1s\rangle + |2p_1\rangle + |3p_1\rangle)/\sqrt{3}$ in the helium atom.

Chapter 5

Rydberg state excitations induced by intense IR radiation

Fundamental processes in strong-field atomic physics are above-threshold ionization (ATI), high harmonic generation (HHG) and non-sequential double ionization. These highly nonlinear processes are induced by the absorption of multiple photons from the laser field, which in the limit of a large photon number can also be described as a tunneling process. Excitation of the atom is known to play an important role in each of the processes. It has been initially observed via resonant enhancement in the population of excited states [?, ?] and structures in the energy spectrum [?, ?, ?] and in energy-resolved angular distributions [?] of photoelectrons. These resonance effects have been explained by multiphoton absorption through Rydberg states, which are AC-Stark shifted in the presence of a laser field. More recently, significant excitation of atoms has also been observed in the tunneling regime and described by the frustrated tunneling ionization model .

The latter observation has renewed the general interest in the mechanisms leading to the population of excited (Rydberg) states during the interaction of an atom with an intense laser pulse (most recently, e.g., in Refs. [?, ?]). The important role of Rydberg states in various strong-field ionization processes and harmonic generation has been discussed. For example, resonant enhancement of below-threshold harmonics [?, ?, ?], emission from excited states via free induction decay [?, ?], high harmonic emission through ionization from excited states and recombination to the ground state [?, ?] have been predicted and observed.

Recent theoretical studies of the excitation mechanism in strong fields mainly consider the

distribution of the population as a function of the principal quantum number of the excited states [?, ?, ?, ?, ?]. It was shown that the modulation of the excitation probability is related to the channel closing effect [?, ?, ?, ?]. The latter phenomenon occurs at threshold intensities at which the absorption of one more photon is needed to ionize the atom due to the shift of the ionization threshold by the ponderomotive energy. The interpretation that an increase in excitation can be understood as result of the shift of the first ATI peak below the ionization threshold [?, ?] is in agreement with the explanation of earlier experimental results (e.g., [?, ?, ?]) via the resonance enhanced population of AC-Stark shifted excited states.

Theoretical analysis of the angular momentum distribution in the populated Rydberg states is less advanced. Predictions of Floquet theory for a monochromatic laser field [?] and results of numerical calculations for laser pulses with a trapezoidal envelope [?] yield that the angular momentum of the excited Rydberg states has the same parity as $N_p - 1$, where N_p is the minimum number of photons needed to ionize the atom. Furthermore, the angular quantum number of the states with the largest population in numerical calculations [?, ?, ?] agrees well with semiclassical estimations [?], initially performed for low-energy angular resolved photoelectron distributions.

In this chapter I present excitation results for linearly polarized laser pulses using selection rules to predict the parity of the angular momentum quantum number of the populated excited states (Sec. 5.1). Then I discuss excitation induced by bi-circular IR laser pulses and interpret the results in the multiphoton picture (Sec. 5.2).

5.1 Linear polarization

In this work we extend the previous analysis by considering excitation in laser pulses with sine squared and Gaussian envelopes. This gives us the opportunity to study if the parity of the populated angular momentum states in such pulses agrees with the selection rules obtained for monochromatic fields and how the results depend on the pulse length at low and high intensities. In the second part we investigate how the population of angular momentum states leaves its footprints in the radiation generated via transitions from the excited states to the ground state. For our studies

we make use of results of numerical solutions of the time-dependent Schrödinger equation (TDSE) for the interaction of the hydrogen atom with an intense linearly polarized laser pulse.

We are solving the time-dependent Schrödinger equation (TDSE) for the interaction of an atom with a linearly polarized intense laser pulse in the velocity gauge (Eq. 3.3) for the Hydrogen atom ($V_{SAE}(r) = -1/r$). The code utilized cylindrical coordinates and second order finite difference. In all calculations presented below we used a grid ranging up to $\rho = 750$ a.u. and $z = \pm 750$ a.u. with a grid spacing of $\Delta = 0.1$ a.u. in both directions and a time step of $\Delta t = 0.15$ a.u. We use the outer 37.5 a.u. of the grid in both directions for the ECS potential. This grid can easily fit bound states up to $n = 14$ within the real portion of the grid.

We study the angular momentum distribution in Rydberg states of the hydrogen atom. To this end, we consider processes during which these states are shifted into resonance with multiphoton absorption from the initial ground state of the atom (with energy E_i). Assuming that the energy shift of high lying excited states under the influence of an intense laser field is approximately equal to the ponderomotive shift [?] and the shift occurs instantaneously during the pulse [?], the intensity for a N_p photon process to resonantly excite approximately with an excited state with energy E_n is given by:

$$I = 4\omega_E^2(N_p\omega_E + E_i - E_n). \quad (5.1)$$

In our calculations we have considered peak intensities such that the $n = 8$ states are in resonance at central frequency ω_E , corresponding to a wavelength of 800 nm, with $N_p = 10, 11, \dots 15$ photon processes. Since we study the interaction with laser pulses, instead of monochromatic fields, more than one manifold of states can be resonantly excited. For example, the bandwidth of a 20 cycle sine squared pulse at 800 nm covers all excited states $n \gtrsim 6$ within the same N_p photon process. We further note that in the present cases, the $n = 3$ and $n = 2$ states are approximately resonant via $N_p - 1$ and $N_p - 2$ photon processes, respectively, assuming that the energy shift of these states equals the ponderomotive energy as well.

However, we observe that the contrast between the population in even and odd states is

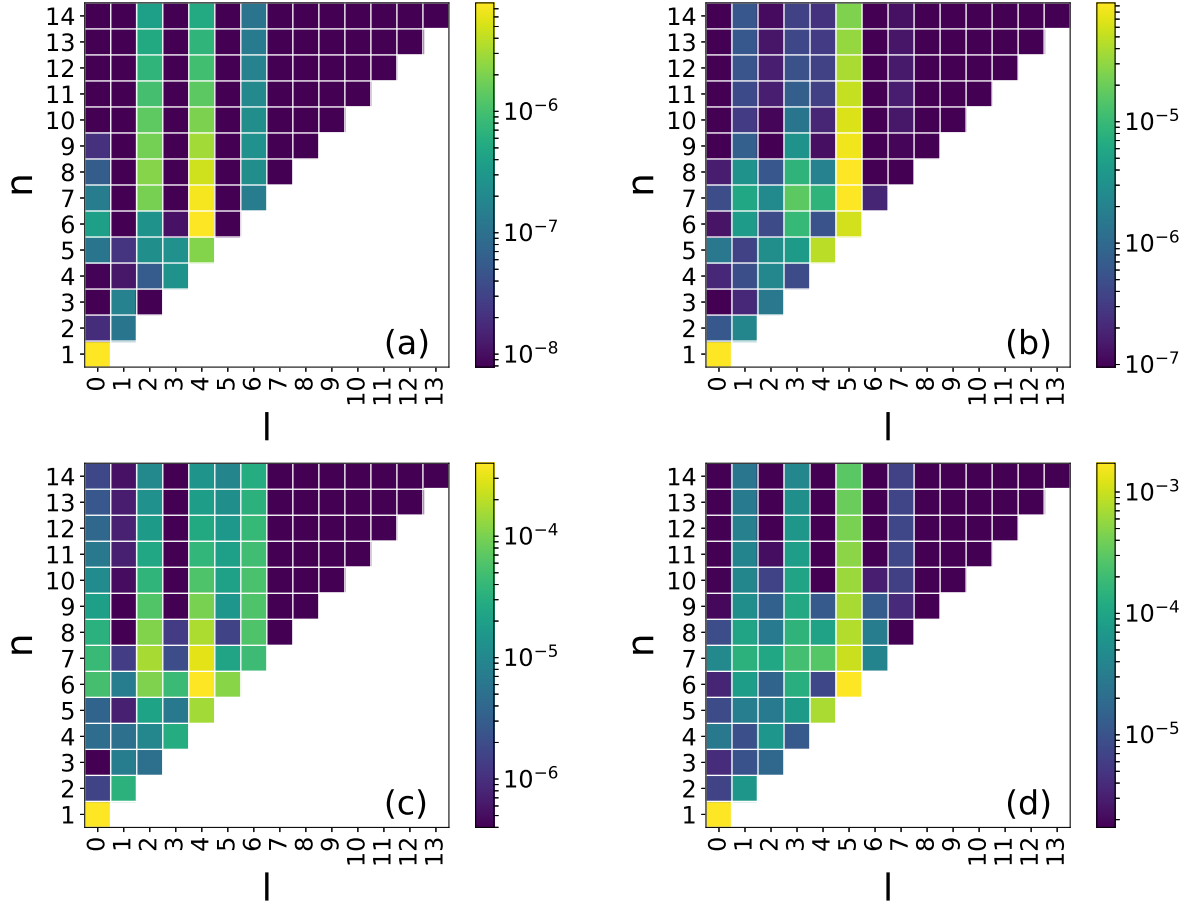


Figure 5.1: Excited state distribution as function of n (vertical axis) and l (horizontal axis) at the end of 20 cycle pulses with sin squared envelope and peak intensities: (a) $I_0 = 3.4 \times 10^{13} \text{ W/cm}^2$, (b) $I_0 = 6.0 \times 10^{13} \text{ W/cm}^2$, (c) $I_0 = 8.6 \times 10^{13} \text{ W/cm}^2$, and (d) $I_0 = 1.12 \times 10^{14} \text{ W/cm}^2$. Left (right) column corresponds to cases in which the Rydberg states are resonant with an even (odd) number of photons.

stronger at lower intensities. We will further discuss this aspect in subsection 5.1.1.

The results also show that for an odd parity process (right column) predominantly one angular momentum state ($l = 5$) is populated. This is in agreement with the results presented by Li et al. [?], who conjectured that electrons in the low angular momentum states more easily absorb additional photons resulting in suppression of population in these states due to ionization. However, our results for even parity processes exhibit a pattern, alternating in l , showing that both low and high angular momentum states, except for the s -states, remain populated at the end of the pulse.

We therefore put forward an alternative explanation. To this end, in Fig. 5.3 we show the

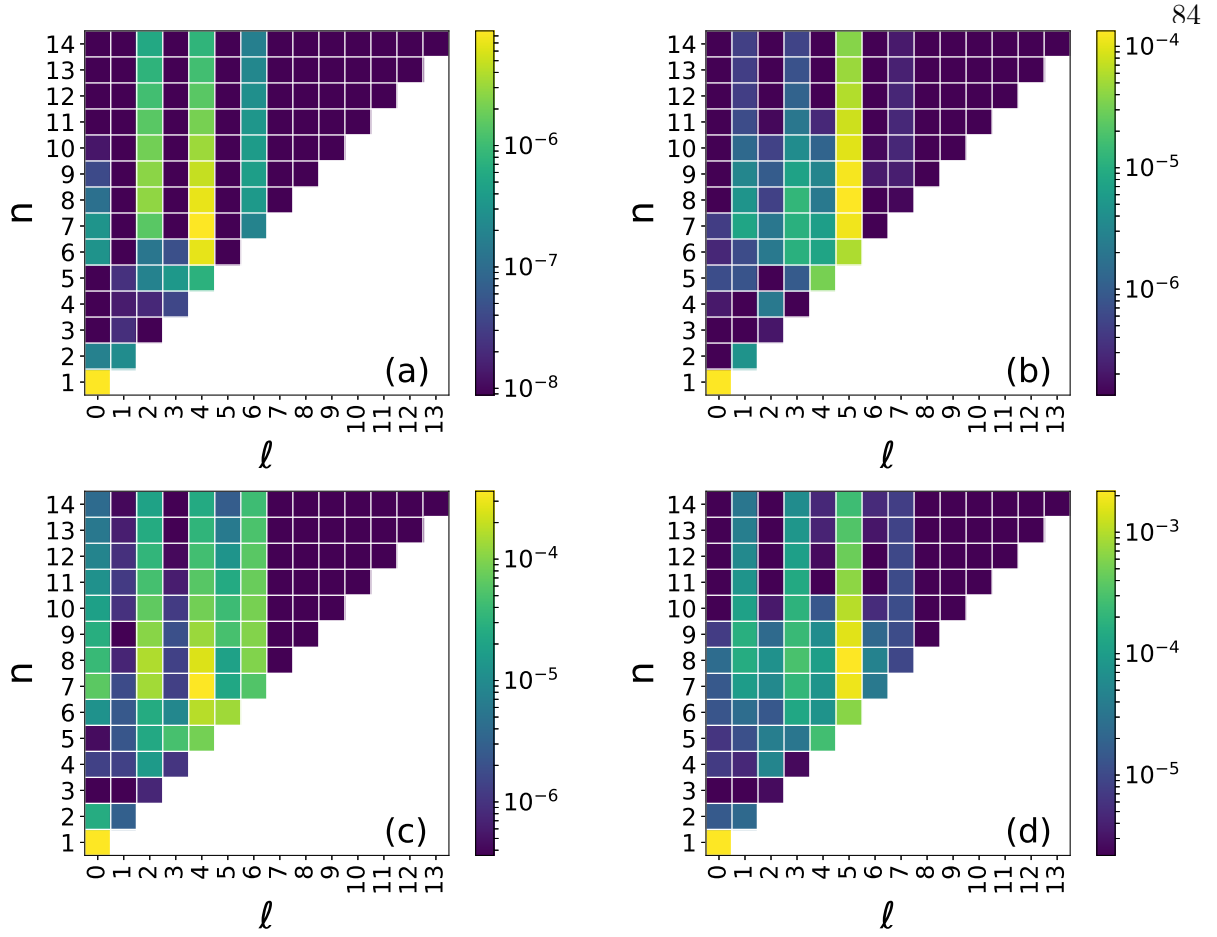


Figure 5.2: Same as Fig. 5.1 but for pulses with Gaussian envelope and 14 cycles FWHM. The pulse duration approximately matches that for the sine-squared pulses in Fig. 5.1 at FWHM.

various pathways leading to a resonant population in the $n = 8$ (and the other Rydberg) states for absorption of an even (top panel) or an odd (bottom panel) number of photons, termed by N_p . Starting from the $1s$ ground state, the absorption of successive photons proceeds through virtual states (depicted via empty green squares in Fig. 5.3), following the selection rule $\Delta l = \pm 1$. As mentioned above, for the hydrogen atom and a pulse at a central wavelength of 800 nm the (shifted) $n = 3$ and $n = 2$ states are approximately resonant via $N_p - 1$ and $N_p - 2$ photon processes, as shown in Fig. 5.3 (real states are depicted by yellow squares labeled with quantum number nl). Assuming that the resonant transitions to lower lying energy levels cause a trapping of population in these states, further absorption from these states will be suppressed. Such suppressed

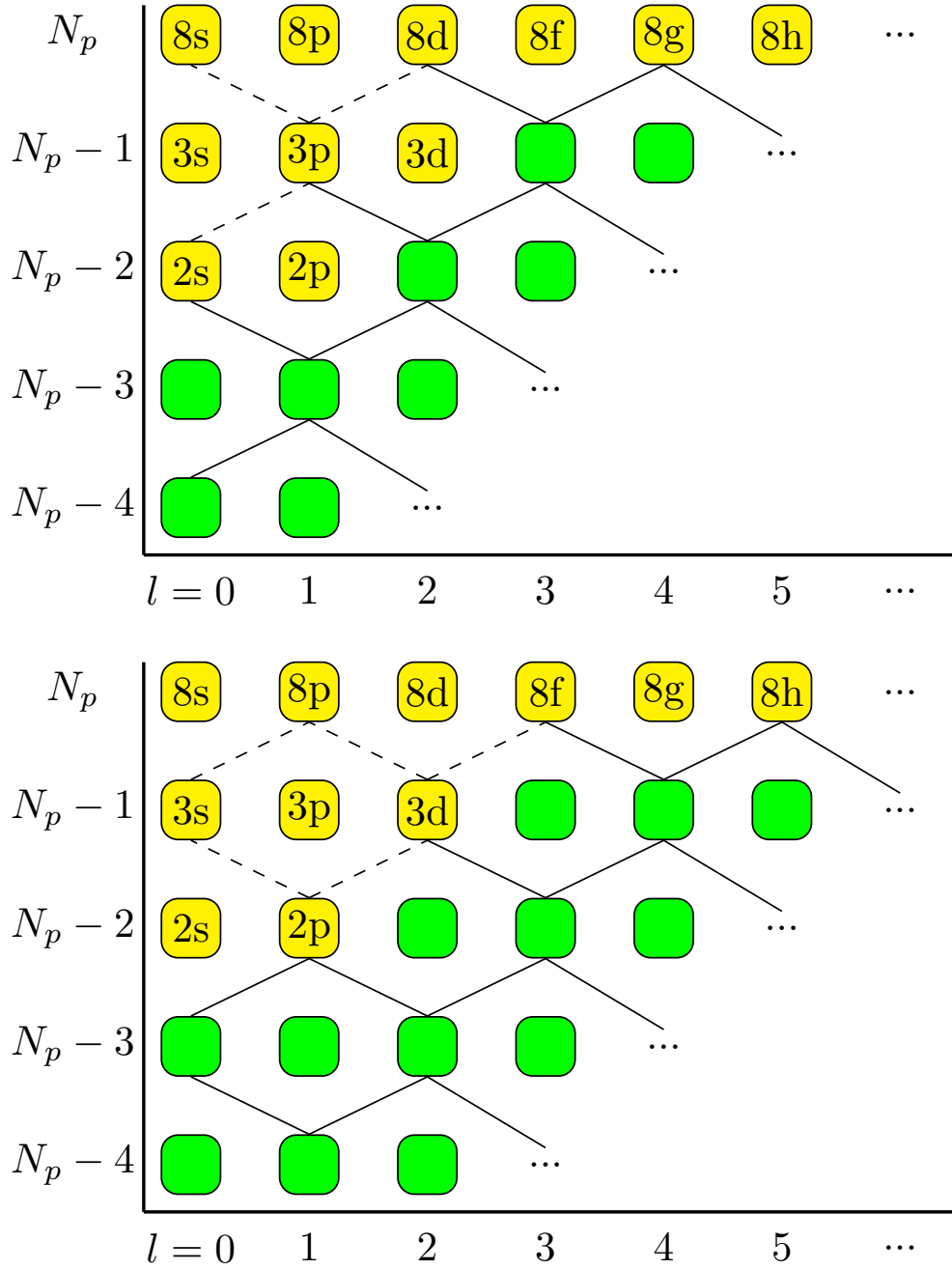


Figure 5.3: The absorption pathways in an even (odd) photon process in the top (bottom) panel. Green squares represent virtual states with energy $N\omega$ above the ground state and angular momentum l . The yellow squares represent real states labeled by the quantum numbers. Solid lines refer to open pathways while dashed lines represent pathways which are suppressed due to population trapping in a lower excited state.

pathways are denoted by dashed lines in Fig. 5.3, while other (open) pathways are represented by

solid lines. Following the pathways, we see that in the manifold of the Rydberg levels for an even number photon process (top panel) the $l = 2$ state is partially and the $l = 4, 6, \dots$ states are fully accessible, while the $l = 0$ (s -state) should be suppressed, which is in agreement with the pattern, alternating in l , that we observe in Figs. 5.1 and 5.2 (left columns). In contrast, for an odd number photon process (bottom panel) the pathways to the $l = 1$ states are strongly and those to the $l = 3$ states are partially suppressed, making the states with $l = 5$ state the first fully accessible states among the Rydberg levels, in agreement with the results presented in Figs. 5.1 & 5.2 (right columns).

5.1.1 Short vs. long pulses and CEP effects

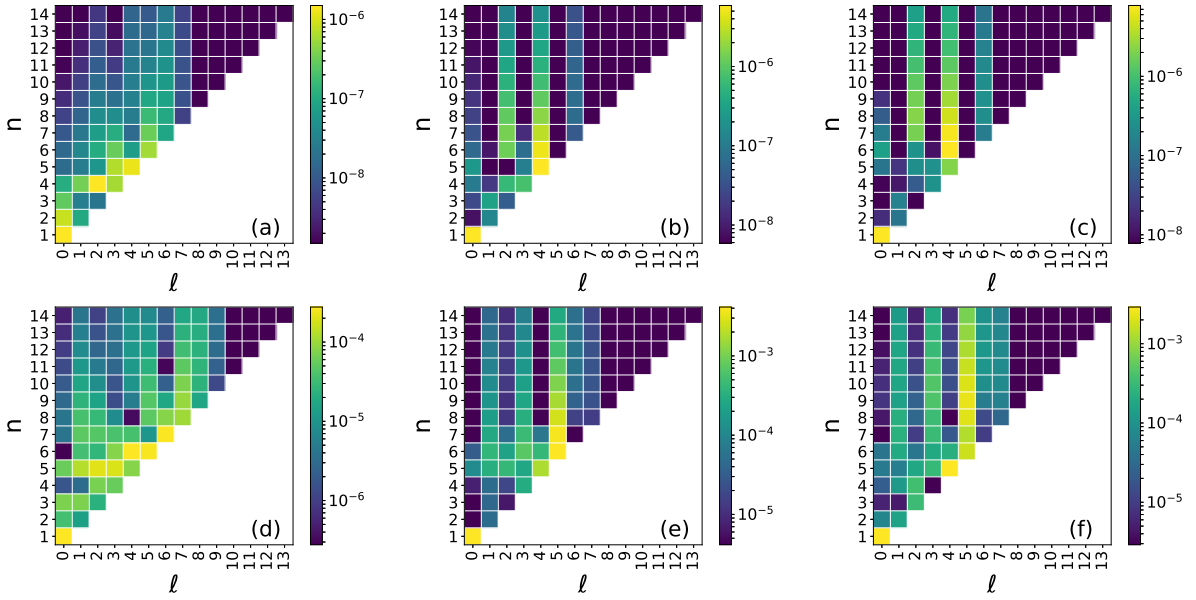


Figure 5.4: Excited state distribution as function of l (horizontal axis) and n (vertical axis) at the end of 2 cycle (panels on left), 10 cycle (panels in middle), and 20 cycle (panels on right) pulses, at low peak intensity $I_0 = 3.4 \times 10^{13} \text{ W/cm}^2$ (top row), and high peak intensity $I_0 = 1.64 \times 10^{14} \text{ W/cm}^2$ (bottom row).

The time-frequency uncertainty relation yields that a pulse spectrum broadens as the number of optical cycles decreases. Consequently, in an ultrashort pulse an excited state can be reached via absorption of different number of photons. Due to this mix of even and odd number of photon

processes one may expect that in such pulses a separation in population of odd vs. even angular momentum quantum states cannot be achieved. This is confirmed by the results of our numerical calculations at low and high intensities, shown in Fig. 5.4(a) and (d). For a 2 cycle pulse there is a smooth distribution over the lower angular momentum states for each principal quantum number at low (3.4×10^{13} W/cm², panel (a)) and high (1.64×10^{14} W/cm², panel (d)) peak intensity.

In contrast, the narrowing of the energy spectrum as pulse duration increases does not necessarily lead to an increase of the population in the angular momentum states of one parity over the other. For the low intensity 10-photon resonant process (3.4×10^{13} W/cm², Fig. 5.4, upper row) we observe in the numerical results that Rydberg states with a well defined angular momentum parity are predominantly populated when the pulse duration is increased to 10 and 20 cycles. On the other hand, at the higher intensity (1.64×10^{14} W/cm², Fig. 5.4, lower row) we observe some contrast between the population in the angular momentum states of different parity for the 10 cycle pulse (panel (e)), while the differences in the population of the different channels further blurs when the duration is increased to 20 cycles (panel (f)).

Within the interpretation of resonant excitation the loss of the parity effect for long pulses with high peak intensities can be understood as follows. At the higher peak intensity, the highly excited states are shifted into resonance for 10-14 photon processes over the rising and trailing parts of the pulse, before they are resonantly excited with a 15 photon process at the peak intensity. Although the excitation probability raises with an increase of the intensity during the pulse, the time intervals over which the states are in resonance with a certain photon-order process increase with the pulse length. Thus, there is a significant excitation of the Rydberg states due to the absorption of odd as well as even numbers of photons in a pulse at high peak intensity and long duration.

Furthermore, excitation channels driven by absorption of different numbers of photons with the same parity may interfere, leading to the enhancement or suppression of population in certain angular momentum states and the loss of the parity effect. Interference effects in excitation have been studied extensively in the few-photon regime. Among others, it has been shown that the

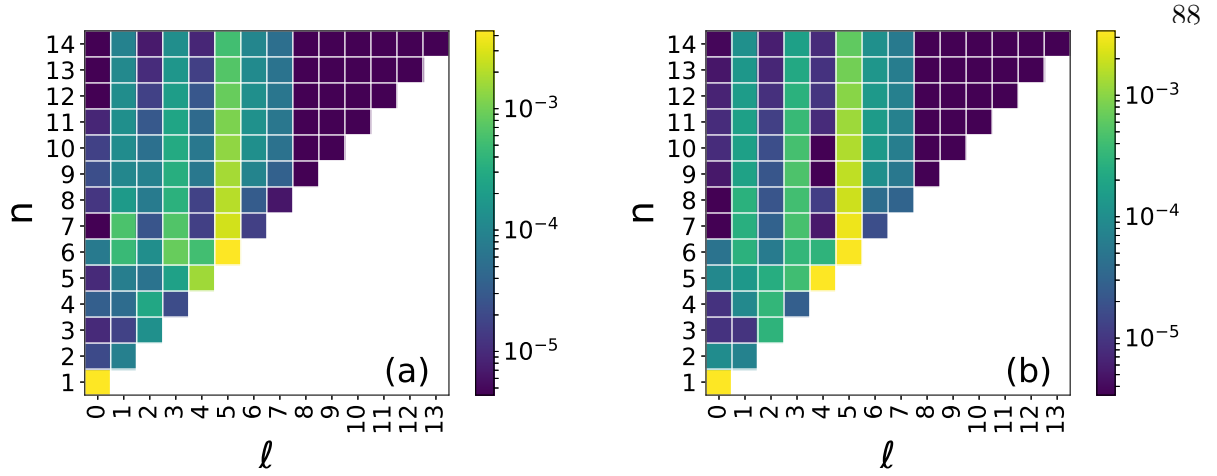


Figure 5.5: Population of excited states from a 20 cycle pulse with peak intensity of $I_0 = 1.64 \times 10^{14}$ W/cm² and CEP of $\phi_A = 0.204\pi$ (a) and $\phi_A = 0.882\pi$ (b)

excitation probabilities can be controlled via the carrier envelope phase (CEP) of the pulse, even in the long pulse limit (e.g., [?, ?]). We observe in the results presented in Fig. 5.5 that the population distribution in the angular momentum states driven by the present more complex multiphoton processes indeed changes significantly with variation of the CEP at high intensities, indicative of potential interference effects.

However, we note that there may exist alternative explanations for the loss of the parity effect in the distribution at long pulses with high peak intensity. For example, in the tunneling regime the mechanism of frustrated ionization has been explored [?]. According to that mechanism highly excited states are populated during the trailing edge of the pulse by deceleration of the electron over many laser cycles and electron recapturing once the laser pulse ceases. Since excited states of any angular momentum can be populated during the recapturing, the loss of the parity effect for long pulses at intensities in the tunneling regime is consistent with the frustrated ionization mechanism as well.

It has recently been discussed [?, ?, ?] that the population of excited Rydberg states leads to the emission of radiation due to the transition from the excited states into the ground state, which can be observed in the below-threshold part of high harmonic spectra. In the case of atomic

hydrogen such emission is associated with an excitation of the np states. In view of the parity effect in the excitation of the Rydberg states according to the absorption of an even or odd number of photons, we expect that the emission may be enhanced or suppressed in certain intensity regimes.

To allow for the separation between the field induced and field free radiation we have calculated the high harmonic spectrum from the dipole acceleration $a(t)$ such that

$$f_{HHG}(\omega; t_f) \propto \int_{-\infty}^{t_f} a(t') e^{-i\omega t'} dt'. \quad (5.2)$$

In Fig. 5.6 we present the radiation spectrum in the region of the 7th and 9th harmonics produced by a 20 cycle, sin squared, 800 nm pulse at intensities (a) $I_0 = 3.4 \times 10^{13}$ W/cm², (b) $I_0 = 6.0 \times 10^{13}$ W/cm², and (c) $I_0 = 1.64 \times 10^{14}$ W/cm². In each panel the red dashed line shows the spectrum generated during the pulse ($t_f = \tau$) while the black solid line includes free propagation after the pulse has ended ($t_f = 2\tau$). The difference between the two spectra exhibits the radiation related to the transitions from the populated excited np states at the end of the pulse to the ground state, which has previously been identified in both experiment [?] and macroscopic simulations [?, ?].

Comparison of the spectra obtained at the two intensities clearly exhibits the expected difference in the features related to the parity effect in the population of the Rydberg states. At an intensity of 3.4×10^{13} W/cm² (Fig. 5.6a), the (shifted) Rydberg energy levels are resonantly excited with a 10 photon process leading to population of the even angular momentum states (c.f., Fig. ??(a)). Consequently, the spectrum is free of line emission from the almost unpopulated Rydberg p -states while we find a strong line corresponding to the strongly populated $3p$ state, which is near resonant with a 9 photon process. In contrast, by shifting the states by the energy of an additional photon, at an intensity of 6.0×10^{13} W/cm² (Fig. 5.6(b)) we observe a rich line emission spectrum just below the 9th harmonic line emissions from the np -states, that are resonantly populated by a 11 photon process (Fig. ??(b)). We note that the $6p$ and $7p$ states are the most populated np states and as a result have the strongest emission lines. On the other hand the line corresponding to the $3p$ state, which cannot be populated by absorption of 10 photons, is strongly

photoelectron momentum distributions [?, ?, ?, ?, ?, ?, ?, ?, ?, ?, ?, ?, ?, ?, ?, ?, ?, ?, ?], double ionization [?, ?, ?, ?, ?, ?, ?] and other strong-field processes [?, ?, ?] driven by bichromatic circularly polarized laser pulses has been performed. One interesting aspect in these kind of strong-field interactions is the control of ionization via the helicity of the applied bichromatic pulses [?, ?, ?]. Such studies complement related work on the dependence of the ionization rate by one-color circularly pulse on the relative helicity between the pulse and the electron in the atomic orbital [?, ?, ?, ?, ?, ?, ?, ?, ?, ?, ?, ?, ?, ?, ?, ?].

For bichromatic circularly polarized laser pulses it has been observed that the probability to ionize an atom is significantly enhanced if the two fields are counter-rotating as compared to co-rotating fields [?]. The experimental observations were interpreted as due to the increased density of excited states accessible for resonant enhanced multiphoton ionization in the case counter-rotating fields. Results of numerical solutions of the time-dependent Schrödinger equation in Ref. [?] did confirm a close relation between the ratios of total excitation and ionization probabilities for counter-rotating and co-rotating circularly polarized laser pulses. However, the results for excitation of the atom were not further resolved by distributions over the quantum numbers (principal, angular momentum, magnetic). Such analysis potentially can shed further light on the role of excited states in the pathways to ionization since excitation in a resonant multiphoton process should rely on the spin-angular momentum selection rules for the absorption of circularly polarized photons ($\Delta l = \pm 1$ and $\Delta m = \pm 1$).

More generally, analysis of the role of strong-field excitation has recently experienced a renaissance [?, ?, ?, ?] following earlier work [?, ?, ?]. Concerning the distribution in the excited states with respect to the quantum numbers studies for the interaction of atoms with linearly polarized pulses have been performed only. Theoretical studies have considered the distribution of the population as a function of the principal and/or the angular momentum quantum number [?, ?, ?, ?, ?, ?]. In applications of Floquet theory for a monochromatic laser field [?] and numerical calculations for laser pulses with trapezoidal [?] and Gaussian or sin-squared envelopes [?] it has been analyzed how the parity of the populated angular momentum states in such pulses relates to

the selection rules for linearly polarized pulses. In view of the recent experimental observations discussed above, we extend these studies to interaction of atoms with bichromatic circularly polarized laser pulses. Such study provides the interesting opportunity to not only resolve the excited state distribution with respect to the principal or angular orbital momentum quantum number, but in particular to consider the role of the magnetic quantum number as well. For our studies we make use of results of numerical solutions of the time-dependent Schrödinger equation (TDSE) for the interaction of the hydrogen atom with intense bichromatic circularly polarized laser pulses.

The paper is organized as follows: In section ?? we briefly summarize the standard methods used to solve the time-dependent Schrödinger equation for the interaction of hydrogen atom with bicircular laser pulses. The results of the numerical calculations are then presented and analyzed in section ??, first for co-rotating and then for counter-rotating pulses. In section ?? we summarize the insights gained into the excitation pathways in bircircular pulses.

The time-dependent Schrödinger equation for the interaction of a electron in the potential of the hydrogen atom with a superposition of two circularly polarized intense laser pulses in dipole approximation and velocity gauge is given by (we use Hartree atomic units $e = m_e = \hbar = 1$):

$$i\frac{\partial}{\partial t}\Psi(\mathbf{r},t) = \left[-\frac{\nabla^2}{2} - \frac{-i\mathbf{A}(t) \cdot \nabla}{c} - \frac{1}{r} \right] \Psi(\mathbf{r},t). \quad (5.3)$$

where $\mathbf{A}(t)$ is the vector potential of the two laser pulses. The wavefunction Ψ is expanded in spherical harmonics up to $l_{max} = 45$ and $m_{max} = 45$. The radius is discretized using fourth order finite difference method with a grid spacing of 0.1 a.u. and a maximum radius of 750 a.u. with exterior complex scaling on the outer 38 a.u. of the grid. The wavefunction is propagated in time using the Crank-Nicolson method with a time step of 0.05 a.u. The choice of gauge was based on the faster convergence of calculations in the velocity gauge for expansions of the wavefunction in spherical harmonics [?, ?].

The interaction with the bicircular laser pulse is implemented via the total vector potential as:

$$\mathbf{A}(t) = \mathbf{A}_\omega(t) + \mathbf{A}_{2\omega}(t) \quad (5.4)$$

where

$$\begin{aligned} \mathbf{A}_\Omega(t) = & A_{0,\Omega} \sin^2 \left(\frac{\pi t}{\tau_\Omega} \right) \\ & \times [\sin(\Omega t) \hat{\mathbf{x}} + \epsilon_\Omega \cos(\Omega t) \hat{\mathbf{y}}] \end{aligned} \quad (5.5)$$

for $\Omega = \omega$ and 2ω , respectively. $A_{0,\Omega} = \frac{c\sqrt{I_\Omega}}{\Omega}$, $\tau_\Omega = \frac{2\pi N_\Omega}{\Omega}$, and c is the speed of light, where I_Ω is the peak intensity and N_Ω denotes the number of cycles. $\epsilon_\Omega = \pm 1$ denotes the helicity of the fundamental and 2nd harmonic pulse, respectively.

We have performed numerical calculations for the interaction of hydrogen atom with co- and counter-rotating bicircular pulses operating at the central wavelengths of 800 nm and 400 nm. Intensities of the two pulses were varied to study the distribution in the excited states as function of all quantum numbers, principal, angular momentum and magnetic. For the results presented below we have used pulses with the same pulse duration in time.

In this section we present the results for the distributions, first for the co-rotating and then for the counter-rotating case, which provide insights into selection rules and excitation pathways in bichromatic multiphoton processes.

5.2.1 Excitation with co-rotating pulses

Selection rules for (single-)photon absorption from circularly polarized light are given by $\Delta l = \pm 1$ and $\Delta m = \pm 1$, where the change in the magnetic quantum number is positive (negative) if the helicity of the light is right- (left-)handed. Extending the concept to multiphoton absorption, the simultaneous change in both quantum numbers puts distinct constraints on the parity and helicity of the accessible excited states in the atoms upon absorption of multiple photons. Specifically, it is expected that states in which ℓ and m are either both even or both odd are being populated during the interaction with the field. This selection holds for the interaction with a single circularly polarized pulse as well as for the case of a superposition of two (or more) of such fields, independent of the relative helicity of the two pulses.

In Fig. 5.7 we show examples of the population in the excited states of hydrogen atom

as a function of n and ℓ for various m values at the end of the interaction with bichromatic co-rotating left-handed circularly polarized pulses. The results clearly confirm the expected population distribution in states with either odd or even parity for a given value of m according to the selection rules upon multiphoton absorption. The present results have been obtained for interaction with equal peak intensities $I_{400} = I_{800} = 5 \times 10^{13} \text{ W/cm}^2$.

Due to the correlation in changes of m and ℓ the observed pattern is independent of total peak intensity, ratio of peak intensities and pulse duration, as long as the dipole approximation holds. In the present study we have verified this up to intensities of $1 \times 10^{14} \text{ W/cm}^2$. This is different from the case of linear polarization [?], where selective population concerning the parity of the populated excited states is observed for long pulses and low peak intensities only. In that case the restriction to a given m -channel and a broad energy spectrum (for short pulse durations) or a significant Stark shift of the excited states (at high peak intensities) leads to a mixing of population over the states with odd and even orbital angular momentum quantum numbers.

In co-rotating bicircular laser pulses all the photons have the same spin (either $+1$ or -1), consequently the magnetic quantum number always changes either by $\Delta m = +1$ or by $\Delta m = -1$ upon absorption of each photon. For our studies we have chosen left-handed helicity for both pulses and, hence, only excited states with negative m can be populated upon absorption of photons from the ground state with $m = 0$ (c.f., Fig. 5.8). Therefore, as already mentioned in Ref. [?], only Rydberg states with high orbital angular quantum number ℓ are accessible. For example, for excitation of Rydberg states (with $n \geq 4$) in the hydrogen atom, the absorption of at least 4 photons in laser field at 400 nm or at least 8 photons at 800 nm is required. Thus, Rydberg states with $\ell < 4$ (and $m > -4$) cannot be populated just via photon absorption alone.

Accordingly, the angular momentum distribution in the Rydberg states is controlled via the relative intensity of the two fields at the fundamental and second harmonic frequency. This is demonstrated in Fig. 5.9, where the excited state distribution as a function of ℓ , summed for $n \geq 4$ and all m , is shown. For large ratio of $I_{400}/I_{800} = 10$ (panel (a)) the distribution is centered, as expected, about $\ell = 4$. As the intensity ratio decreases, high orbital angular momentum states get

increasingly populated due to the impact of the laser pulse at 800 nm.

Another interesting feature in Fig. 5.9 is that the population in angular momentum states with $\ell < 4$ increases significantly when the intensities of the two pulses are similar. Further insight can be gained by the distribution over the magnetic quantum number, which is displayed in Fig. 5.10(c) for the case of equal intensities. It is clearly seen that Rydberg states with magnetic quantum numbers between $m = 0$ and $m = -3$ are populated. In view of the number of photons needed to reach the Rydberg levels, the population in these states cannot be explained by absorption of photons only.

Instead, we propose the following mechanism: Initially, Rydberg states with $\ell \geq 4$ are populated via the absorption pathways shown in Fig. 5.8. Then a redistribution of population occurs via Raman-type Λ -transitions (c.f., [?, ?]). In the present bichromatic laser field the Λ -process leads to a change in the magnetic quantum number, if photons from both fields are involved. For the absorption of one 400 nm photon and emission of two 800 nm photons the magnetic quantum number between initial and final state changes by $\Delta m = +1$.

The order of absorption and emission may vary, i.e., the redistribution process can either proceed via the continuum (absorption first, Fig. 5.10(a)) or via a lower excited state (emission first, Fig. 5.10(b)). A larger change in m is achieved either via a sequence of these Λ -processes or by higher order processes (e.g., absorption of two 400 nm photons followed by emission of four 800 nm photons leading to $\Delta m = +2$). We note that similarly the absorption of two photons at 800 nm and the emission of a 400 nm photon will lead to a change of $\Delta m = -1$ in the present set-up and, hence, contribute to population of states with higher ℓ and m .

Our interpretation is further supported by the results in Fig. 5.11, which shows how the population in states of certain quantum numbers for (a) $\ell = 2$ and (b) $\ell = 3$ changes as function of the relative intensity of the two pulses. It is clearly seen that the population in these quantum states, which are not accessible via direct absorption of photons from the ground state, increases as the intensity of the pulse at 800 nm increases. Thus, these results provide further indications that the presence of the redistribution process depends on the impact of both pulses and its effectiveness

increases with increase of the total intensity, in agreement with our interpretation of a Λ -type process.

5.2.2 Excitation with counter-rotating pulses

As discussed in the previous subsection, the selection rules by which only states with ℓ and m either both even or both odd hold independent of the relative helicity of the two pulses. This is confirmed by the results that we obtained for the interaction with two counterrotating pulses at equal intensities and equal pulse duration presented in Fig. 5.12. Depending on whether m is even or odd, the distribution over the orbital angular momentum shows population in states with even or odd parity. As in the case of corotating pulses, the observed pattern is found independent of total peak intensity, ratio of peak intensities and pulse duration.

Since in counter-rotating bicircular laser pulses photons of the two fields have opposite spin, starting from the ground state with $m = 0$, excited states with both positive and negative magnetic quantum numbers can be populated. The absorption pathways for the set-up chosen in the present studies, namely right-handed helicity for the 800 nm pulse and left-handed helicity for the second harmonic, are shown in Fig. 5.13. As can be seen from the Figure, the magnetic quantum number reflects the difference between the number of 400 nm photons and that at 800 nm absorbed. Furthermore, it can be seen that for a given total photon energy absorbed states with magnetic quantum numbers separated by $\Delta m = \pm 3$ are populated.

These features are clearly present in the population distributions as function of m , summed over n and ℓ (top), and of n and m , summed over ℓ (bottom), in Fig. 5.14, which show the results for counter-rotating pulses of equal peak intensity. In the Rydberg manifold ($n \geq 4$) the highest populated m -states differ by $\Delta m = \pm 3$, other states show some but lower population as the manifold is AC-stark shifted during the interaction with the pulses. In view of the nonlinearity of multiphoton processes, it is likely that the states showing the largest probability are being populated near the peak of the pulses at which the highest total intensity is present. Overall, the strongest population is seen for states with negative magnetic quantum numbers, leading to the conclusion that it most

likely that either five (for excited states with $m = -5$) or two (for excited states with $m = -2$) more 800 nm photons with left-handed helicity than 400 nm photons with right-handed helicity are being absorbed.

The distributions in Fig. 5.14 do not extend much beyond $|m| = 5$, which is consistent with the results shown in Fig. 5.15 showing that there appears to be a highest orbital angular momentum number ℓ_{max} beyond which the population in the states drops off quickly. This is in agreement with previous studies for Rydberg state excitation [?, ?] and low energy angular momentum distributions [?]. In Ref. [?] a random walk analysis of the absorption pathways between the accessible quantum states is used to obtain the classical orbital angular momentum for a electron with zero energy in a laser field has been derived as $L = \sqrt{2Z\alpha_0}$ where Z is the charge of the residual ion and α_0 is the quiver radius. Relating classical orbital angular momentum and the orbital angular momentum quantum number by $\ell \approx L - 1/2$ we have estimated the maximum ℓ gained in the bicircular counter-rotating pulse. The estimates, shown by the solid red lines in Fig. 5.15, are in good agreement with the cut-offs seen in the numerical results. We note that the random walk analysis of Ref. [?] can be applied in the case of counter-rotating pulses, since in each absorption step $\Delta m = \pm 1$ and hence, in general, $\Delta \ell = \pm 1$ is possible. In contrast, for co-rotating pulses the changes in magnetic and angular quantum number are determined in each absorption step ($\Delta m = -1$, $\Delta \ell = +1$) and hence a random walk analysis is not applicable and a cut-off cannot be derived.

We have studied the distributions over the orbital angular momentum (ℓ) and magnetic (m) quantum numbers in Rydberg states due to the interaction with bichromatic circularly polarized laser pulses. Multiphoton selection rules lead to population of states in which ℓ and m are either both even or both odd, independent of relative helicity, peak intensity and pulse duration. In the case of co-rotating pulses the results show that the distribution over the magnetic quantum number can be controlled via the intensities of the two pulses. Furthermore, we propose that the states are populated via direct absorption from the ground state and via Λ -type transitions between Rydberg states of different ℓ and m , involving two photons at the fundamental wavelength and one photon at the second harmonic. For bicircular laser pulses with opposite helicities Rydberg states with

magnetic quantum numbers that differ by $\Delta m = \pm 3$ are predominantly populated. The pattern allows to gain insights into the relative number of photons absorbed from the two fields. The distribution is however restricted by the maximum orbital angular momentum quantum number that can be estimated by classical considerations.

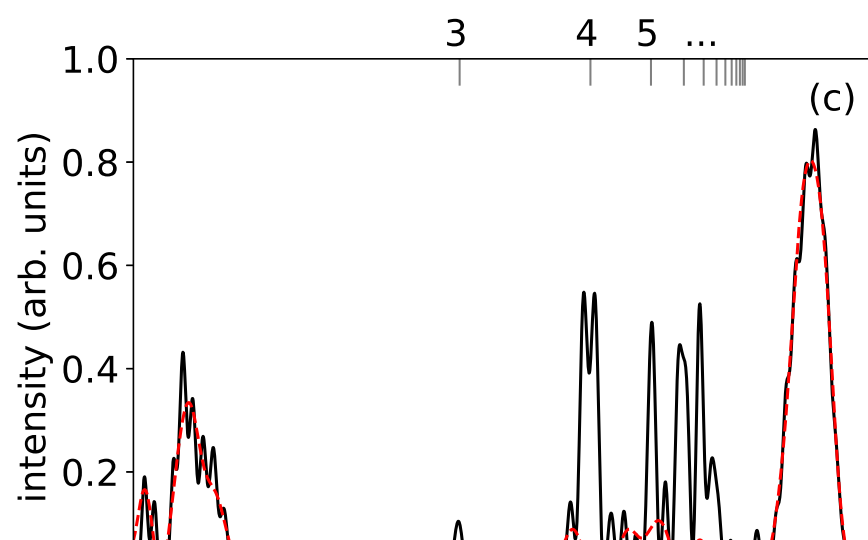
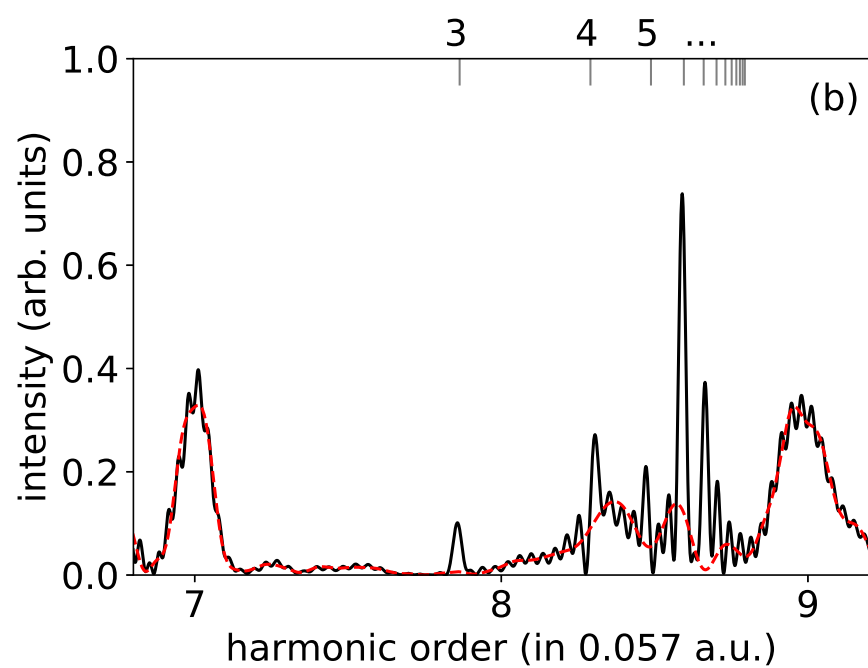
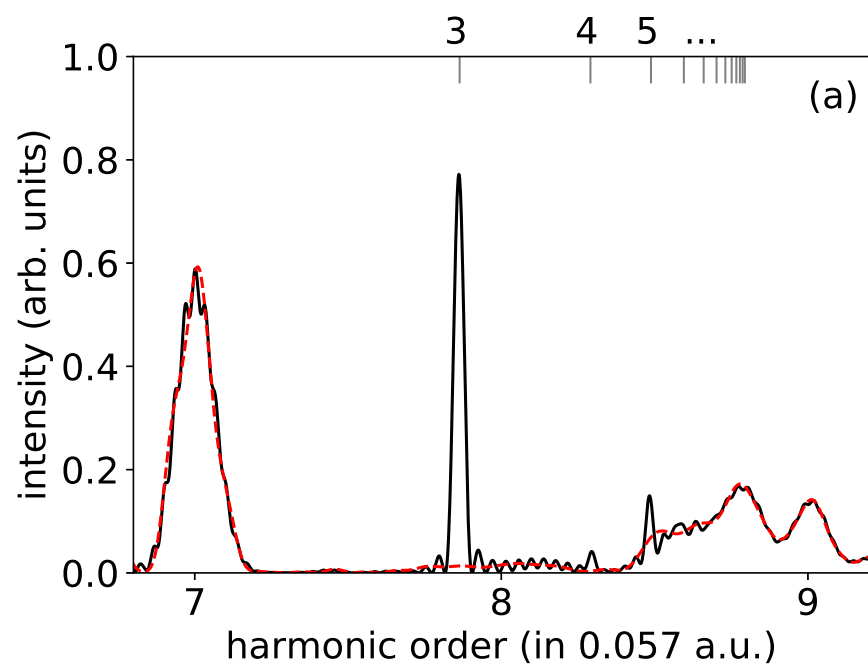


Figure 5.7: (Color online) Excited state distribution as function of n (vertical axis) and ℓ (horizontal axis) for (a) $m = -1$, (b) $m = -2$, (c) $m = -3$ and (d) $m = -4$ at the end of 20 (at 800 nm) cycle pulses (40 cycle at 400 nm) with sin squared envelope and total peak intensity of 1×10^{14} W/cm² for co-rotating laser pulses of equal intensity.

Figure 5.8: (Color online) Absorption pathways in co-rotating laser pulses at frequencies ω and 2ω starting from a $m = 0$ -state. Without lack of generalization it is assumed that both pulses have left-handed helicity. Absorption of a photon at frequency ω and at frequency 2ω is represented by a red and blue arrow, respectively. The numbers in the boxes denote the minimum number of photons to reach a certain level.

Figure 5.9: (Color online) Excited state distribution as function of orbital angular quantum number ℓ summed over $n \geq 4$ and m at (a) $I_{400} = 5 \times 10^{13}$ W/cm², $I_{800} = 5 \times 10^{12}$ W/cm², (b) $I_{400} = 5 \times 10^{13}$ W/cm², $I_{800} = 1 \times 10^{13}$ W/cm², (c) $I_{400} = 5 \times 10^{13}$ W/cm², $I_{800} = 5 \times 10^{13}$ W/cm², and and (d) $I_{400} = 1 \times 10^{13}$ W/cm², $I_{800} = 5 \times 10^{13}$ W/cm². Pulse durations: 20 cycles at 400 nm, 10 cycles at 800 nm.

Figure 5.10: (Color online) Excited state distribution as function of n (vertical axis) and m (horizontal axis) summed over ℓ . Laser parameters: 20 (800 nm) cycle pulses with sin squared envelope and total peak intensity of 1×10^{14} W/cm² for co-rotating laser pulses of equal intensity.

Figure 5.11: (Color online) Distribution in magnetic quantum states for (a) $\ell = 2$ and (b) $\ell = 3$ and different peak intensities of the 800 nm pulse. $I_{400} = 5 \times 10^{13}$ W/cm² and other parameters are as in Fig. 5.10.

Figure 5.12: (Color online) Same as Fig. 5.7 but for counterrotating laser pulses.

Figure 5.13: (Color online) Absorption pathways in counter-rotating laser pulses at frequencies ω and 2ω starting from a $m = 0$ -state. Without lack of generalization it is assumed that the pulses at frequency ω has left-handed helicity, while the second harmonic pulse has right-handed velocity. Other symbols as in Fig. 5.8.

Figure 5.14: (Color online) Excited state distributions as a function of m , summed over $n \geq 4$ and ℓ (top), and as a function of n and m , summed over ℓ (bottom), for the interaction with a left-handed circularly polarized laser pulse at 800 nm (20 cycles) and a right-handed circularly polarized laser pulse at 400 nm (40 cycles). Both pulses have the same peak intensity of 5×10^{13} W/cm².

Figure 5.15: (Color online) Orbital angular momentum distributions in excited states induced by counter-rotating laser pulses at 400 nm (20 cycles) and 800 nm (10 cycles) at peak intensities of (a) $I_{400} = 5 \times 10^{13}$ W/cm², $I_{800} = 5 \times 10^{12}$ W/cm², (b) $I_{400} = 5 \times 10^{12}$ W/cm², $I_{800} = 5 \times 10^{13}$ W/cm², and (c) $I_{400} = 5 \times 10^{13}$ W/cm², $I_{800} = 5 \times 10^{13}$ W/cm².

Chapter 6

Correlation effects in attosecond electron dynamics

6.1 Hyperspherical harmonics

Solving the TDSE for two active electrons is a computationally difficult task. A Naive approach would be to discretized the 6 spacial dimensions using finite difference. Finite difference would provide a straight forward solution and runs well on supercomputing systems, however, the size of the wavefunction scales like N^6 . Therefore if we were to use a typical grid of 1000 points in each dimension, the wavefunction would be 10^{18} points in size. Merely writing down the wavefunction in double precision floating point numbers would require 16 Exabytes of RAM, approximately 100 times more RAM than exists on the largest supercomputer in the world (Summit, OLCF). Instead, it is convent to choose a basis that greatly reduces the size of the problem. One common approach is to use bi-spherical harmonics. In this case, each electron is expanded in 3D spherical coordinates. The radius is discretized with finite difference, b-splines, FEDVR, or similar method, and the two angular coordinates are explained in the standard 3D spherical harmonics in the same way a single active electron code would do. When taking the tensor product of the two electrons, the electron-electron repulsion term is then expanded in spherical harmonics such that

$$\frac{1}{|\mathbf{r}_1 - \mathbf{r}_2|} = 4\pi \sum_{\ell=0}^{\infty} \sum_{m=-\ell}^{m=\ell} \frac{1}{2\ell+1} \frac{r_{<}^{\ell}}{r_{>}^{\ell+1}} Y_{\ell m}^*(\theta_1, \phi_1) Y_{\ell m}(\theta_2, \phi_2). \quad (6.1)$$

Resulting in a 6D space that can be used to solve the problem of two electrons in a molecular or atomic potential interacting with a laser.

In the bi-spherical codes, one must discretize two radii. As the grid increases in size, the code

likes N^2 . To circumvent this problem, I have implemented a code that contains a single hyper-radius (R) and five angles that are expanded in 6D hyperspherical harmonics. Therefore as the grid size is increased, the code scales like N and the number of spherical harmonics is controlled by the laser parameters. In the following section, I will describe the details to implementing two different “coordinate systems” that solve the two active electron problem. The first is through the use of Jacobi Coordinates, which allows for the finite mass of the nucleus to be accounted for. The second is making the infinite mass approximation for the nucleus allowing for the distance between the two electrons to be accessed more directly. The two problems can be solved with similar sized wavefunctions, however, the second method has a greatly reduced time in calculating matrix elements. This section is laid out \dots **TODO**

6.1.1 TDSE in hyperspherical coordinates

The TDSE

$$i\frac{\partial}{\partial t}\Psi = \hat{H}\Psi \quad (6.2)$$

with hamiltonian written in hyperspherical coordinates is

$$\hat{H} = -\frac{1}{2} \left[\frac{1}{R^5} \frac{\partial}{\partial R} \left(R^5 \frac{\partial}{\partial R} \right) - \frac{\hat{K}^2(\Omega_5)}{R^2} \right] + \frac{W(\Omega_5)}{R} \quad (6.3)$$

where $R = \sum_i x_i^2$ is the hyper radius with x_i being a Cartesian coordinate, \hat{K} as the angular momentum operator, Ω_5 is the solid angle in 6D (5 angles), and $V(\mathbf{R}) = W(\Omega_5)/R$ being the potential. I will use the hyperspherical harmonics such they contain two-3D sub spaces as described in Sec. 6.1.1.1. The resulting volume elements are

$$d\tau = R^5 dr d\Omega_i \quad (6.4)$$

$$d\Omega_i = \cos^2 \alpha \sin^2 \alpha d\alpha d\omega \quad (6.5)$$

$$d\omega = \sin \theta_{r_1} d\theta_{r_1} d\phi_{r_1} \sin \theta_{r_1} d\theta_{r_1} d\phi_{r_1} \quad (6.6)$$

where θ_i and ϕ_i denote the angles in the $i = r_1$ and $i = r_1$ sub coordinate systems and α is the angle produced by the right triangle with sides R , r_1 , and r_1 as shown in Fig. 6.1. r_1 and r_2 will be used

as the Jacobi Coordinates for finite mass nucleus is considered or the single electron coordinates when the infinite mass approximation is made.

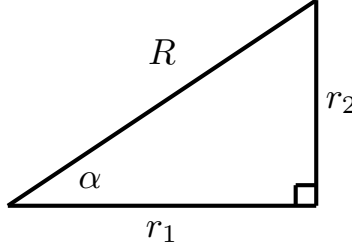


Figure 6.1: How the hyperradius (R) relates to the two single-electron sub coordinate systems (r_1 , r_2)

As with the 3D TDSE, it is beneficial to remove the first derivative in the radial equation. This is accomplished by making a substitution of $\Psi = \psi/R^{5/2}$ giving us a Hamiltonian

$$\hat{H} = -\frac{1}{2} \left[\frac{\partial^2}{\partial R^2} - \frac{\hat{K}^2(\Omega_5) + 15/4}{R^2} \right] + \frac{W(\Omega_5)}{R}. \quad (6.7)$$

The wavefunction can now be written as

$$\psi = \sum_{\mathbf{K}} U_{\mathbf{K}}(R) Y_{\mathbf{K}}(\Omega_5) \quad (6.8)$$

with $U_{\mathbf{K}}(R)$ being the hyperradial part of the wavefunction and $Y_{\mathbf{K}}(\Omega_5)$ being the 6D hyperspherical harmonics described in Sec. 6.1.1.1. Since hyperspherical harmonics are eigenfunctions of \hat{K}^2 with eigenvalue $K(K+4)$, the Hamiltonian becomes

$$\hat{H}_K = -\frac{1}{2} \left[\frac{\partial^2}{\partial R^2} - \frac{K(K+4) + 15/4}{R^2} \right] + \frac{W(\Omega_5)}{R}. \quad (6.9)$$

I solve this equation using finite difference to discretized the hyperradial function ($U_{\mathbf{K}}(R)$). By setting $W(\Omega_5) = 1$, the equation is the 6D hydrogen atom with an analytic solution that can be used to test the hyperadial portion of the code (see [?] for energy levels). The angular portion of the equations is then expanded in hyperspherical harmonics. The details of the expansion are the focus of the remainder of this section.

6.1.1.1 Hyperspherical Harmonic Definition

There are multiple ways to define hyperspherical harmonics in 6D. Since they are equivalent up to a unitary rotation, it is best to choose those that match the symmetry of the problem. In our case, we choose spherical harmonics that contain a hyperangle α that connects two-3D spaces as shown in Fig. 6.1. The 3D spaces belong to coordinates \mathbf{r}_1 and \mathbf{r}_2 with radii r_1 and r_2 respectively. These spaces will either represent a Jacobi Coordinate (Sec. 6.1.1.2) or the space of each electron (Sec. 6.1.1.3). The resulting 6D spherical harmonics are given by

$$Y_{K,L,M}^{\ell_{r_1},\ell_{r_2}}(\Omega_5) = N_{K,L,M}^{\ell_{r_1},\ell_{r_2}} P_n^{(\ell_{r_1}+1/2,\ell_{r_2}+1/2)}(\cos(2\alpha)) \cos^{\ell_{r_1}}(\alpha) \sin^{\ell_{r_2}}(\alpha) \quad (6.10)$$

$$\times \sum_{m_{r_1},m_{r_2}} \langle L, M | \ell_{r_1}, m_{r_1}, \ell_{r_2}, m_{r_2} \rangle \left[Y_{\ell_{r_1},m_{r_1}}(\hat{r}_1) \times Y_{\ell_{r_2},m_{r_2}}(\hat{r}_2) \right] \quad (6.11)$$

with

$$N_{K,L,M}^{\ell_{r_1},\ell_{r_2}} = \sqrt{\frac{2(K+2)(n!)\Gamma(n+\ell_{r_1}+\ell_{r_2}+2)}{\Gamma(n+\ell_{r_1}+3/2)\Gamma(n+\ell_{r_2}+3/2)}}. \quad (6.12)$$

where $P_n^{(\alpha,\beta)}$ is a Jacobi polynomial, $\langle L, M | \ell_{r_1}, m_x, \ell_{y_1}, m_y \rangle$ is a Clebsch–Gordan coefficient, Γ is a gamma function, $Y_{\ell_r,m_r}(\hat{r})$ is the standard 3D spherical harmonics, and Ω_5 is the 6D solid angle containing 5 angular dimensions. K , L , M , ℓ_{r_1} and ℓ_{r_2} are the quantum numbers with $K = 2n + \ell_{x_1} + \ell_{y_1}$ being the grand angular momentum, $\ell_{r_1} \geq 0$ and $\ell_{r_2} \geq 0$ being the angular momentum for the \mathbf{r}_1 and \mathbf{r}_2 coordinates respectively, $|\ell_{r_1} - \ell_{r_2}| \leq L \leq \ell_{r_1} + \ell_{r_2}$ and $-L \leq M \leq L$. For simplicity, we define $\mathbf{K} = \{K, L, M, \ell_{r_1}, \ell_{r_2}\}$ allowing for the simplified notation $Y_{\mathbf{K}}(\Omega_5)$.

The hyperspherical harmonics contain three parts, each depending on one free parameter α , \mathbf{r}_1 , and \mathbf{r}_2 . By defining

$$\tilde{P}_n^{\ell_{r_1},\ell_{r_2}}(\alpha) = N_{K,L,M}^{\ell_{r_1},\ell_{r_2}} P_n^{(\ell_{r_1}+1/2,\ell_{r_2}+1/2)}(\cos(2\alpha)) \cos^{\ell_{r_1}}(\alpha) \sin^{\ell_{r_2}}(\alpha) \quad (6.13)$$

hyperspherical harmonics become

$$Y_{K,L,M}^{\ell_{r_1},\ell_{r_2}}(\Omega_5) = \tilde{P}_n^{\ell_{r_1},\ell_{r_2}}(\alpha) \sum_{m_{r_1},m_{r_2}} \langle L, M | \ell_{r_1}, m_{r_1}, \ell_{r_2}, m_{r_2} \rangle \left[Y_{\ell_{r_1},m_{r_1}}(\hat{r}_1) \times Y_{\ell_{r_2},m_{r_2}}(\hat{r}_2) \right] \quad (6.14)$$

highlighting the three sections.

6.1.1.2 Jacobi Coordinates

Jacobi coordinates are often used for studying many body interactions. They are defined by choosing a particle and defining a relative coordinate between them. The next particle is defined by a coordinate connecting the center of mass of all the previous particles to the next particle. The result is a set of coordinates that has dimension $3(N - 1)$ assuming the exact location of the center of mass R_{cm} in space is irrelevant. For a three particle system, the center of mass is

$$\mathbf{R}_{cm} = m_1 \mathbf{r}_1 + m_2 \mathbf{r}_2 + m_3 \mathbf{r}_3 \quad (6.15)$$

and three convenient sets of Jacobi coordinates are

$$\mathbf{x}_1 = \left[\frac{m_2 + m_3}{m_1(m_2 + m_3)^2} \right]^{1/4} (\mathbf{r}_3 - \mathbf{r}_2); \quad \mathbf{y}_1 = \left[\frac{m_1(m_2 + m_3)^2}{m_2 + m_3} \right]^{1/4} \left(\mathbf{r}_1 - \frac{m_2 \mathbf{r}_2 + m_3 \mathbf{r}_3}{m_2 + m_3} \right) \quad (6.16)$$

$$\mathbf{x}_2 = \left[\frac{m_3 + m_1}{m_2(m_3 + m_1)^2} \right]^{1/4} (\mathbf{r}_1 - \mathbf{r}_3); \quad \mathbf{y}_2 = \left[\frac{m_2(m_3 + m_1)^2}{m_3 + m_1} \right]^{1/4} \left(\mathbf{r}_2 - \frac{m_3 \mathbf{r}_3 + m_1 \mathbf{r}_1}{m_3 + m_1} \right) \quad (6.17)$$

$$\mathbf{x}_3 = \left[\frac{m_1 + m_2}{m_3(m_1 + m_2)^2} \right]^{1/4} (\mathbf{r}_2 - \mathbf{r}_1); \quad \mathbf{y}_3 = \left[\frac{m_3(m_1 + m_2)^2}{m_1 + m_2} \right]^{1/4} \left(\mathbf{r}_3 - \frac{m_1 \mathbf{r}_1 + m_2 \mathbf{r}_2}{m_1 + m_2} \right). \quad (6.18)$$

The three coordinate systems are depicted in Fig. 6.2. For the Helium atom we place the nucleus as m_1 and the two electrons at m_2 and m_3 . Then we set $m_1 \rightarrow \infty$ and $m_2 = m_3 = m$. Now we define β_i with $i = 1, 2, 3$ such that

$$\mathbf{x}_1 = \beta_1 (\mathbf{r}_3 - \mathbf{r}_2); \quad \mathbf{y}_1 = \frac{1}{\beta_1} \left(\mathbf{r}_1 - \frac{\mathbf{r}_2 + \mathbf{r}_3}{2} \right) \quad (6.19)$$

$$\mathbf{x}_2 = \beta_2 (\mathbf{r}_1 - \mathbf{r}_3); \quad \mathbf{y}_2 = \frac{1}{\beta_2} \left(\mathbf{r}_2 - \frac{\mathbf{r}_3 + \mathbf{r}_1}{2} \right) \quad (6.20)$$

$$\mathbf{x}_3 = \beta_3 (\mathbf{r}_2 - \mathbf{r}_1); \quad \mathbf{y}_3 = \frac{1}{\beta_3} \left(\mathbf{r}_3 - \frac{\mathbf{r}_1 + \mathbf{r}_2}{2} \right) \quad (6.21)$$

Within the infinite mass approximation, $\beta_1 = 1/\sqrt{2}$ and $\beta_2 = \beta_3 = 1$. By applying a Raynal-Revai Coefficient (RRC) it is possible to transition between the three different coordinate systems. The transformation conserves the angular momentum quantum numbers K , L , and M of the hyperspherical harmonics.

The RRC coefficients for rotating between coordinate system i and j can be written explicitly

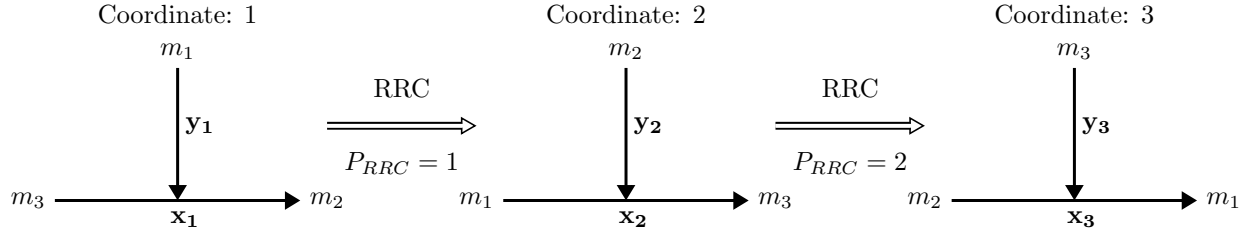


Figure 6.2: The Jacobi coordinates for three body interactions. Each coordinate can be obtained from the previous by utilizing a Raynal-Revai Coefficient

as

$$\begin{aligned}
\langle \ell_{x_j}, \ell_{y_j} | \ell_{x_i}, \ell_{y_i} \rangle_{K,L} = & \frac{(-1)^{n_i+n_j}}{\sqrt{C_{\ell_{x_j}\ell_{y_j}}^{n_j} C_{\ell_{x_i}\ell_{y_i}}^{n_i}}} \sum_{\lambda_1, \lambda_2, \lambda_3, \lambda_4} i^{\lambda_2 - \lambda_1 + \ell_{y_i} - \ell_{y_j}} \left[\prod_{k=1}^4 (2\lambda_k + 1) \right] \\
& \times \langle \lambda_1 0 \lambda_3 0 | \ell_{x_j} 0 \rangle \langle \lambda_2 0 \lambda_3 0 | \ell_{x_i} 0 \rangle \langle \lambda_2 0 \lambda_4 0 | \ell_{y_j} 0 \rangle \langle \lambda_1 0 \lambda_4 0 | \ell_{y_i} 0 \rangle \\
& \times \text{sgn}(a_{12})^{\lambda_1} \text{sgn}(a_{21})^{\lambda_2} \text{sgn}(a_{11})^{\lambda_3} \text{sgn}(a_{22})^{\lambda_4} \begin{bmatrix} \lambda_3 & \lambda_1 & \ell_{x_j} \\ \lambda_2 & \lambda_4 & \ell_{y_j} \\ \ell_{x_i} & \ell_{y_i} & L \end{bmatrix} \\
& \times \sum_{\nu, \mu} (-1)^\mu |a_{12}|^{2\mu + \lambda_1 + \lambda_2} |a_{12}|^{2\nu + \lambda_3 + \lambda_4} C_{\lambda_1 \lambda_2}^\mu C_{\lambda_3 \lambda_4}^\nu \quad (6.22)
\end{aligned}$$

where $\text{sgn}(a_{ij})$ is the sign of a_{ij} , the sum is restricted by $K = 2n_i + \ell_{x_i} + \ell_{y_i} = 2n_j + \ell_{x_j} + \ell_{y_j} = 2(\mu + \nu) + \lambda_1 + \lambda_2 + \lambda_3 + \lambda_4$, $\langle \lambda_1 0 \lambda_3 0 | \ell_{x_j} 0 \rangle$ is a Clebsch Gordan coefficient, $\begin{bmatrix} \lambda_3 & \lambda_1 & \ell_{x_j} \\ \lambda_2 & \lambda_4 & \ell_{y_j} \\ \ell_{x_i} & \ell_{y_i} & L \end{bmatrix}$ is a wigner 9j symbol, $C_{\alpha\beta}^\mu = \frac{(2\mu + \alpha + \beta + 1)!}{(\mu)!(\mu + \alpha + \beta + 1)!(2(\mu + \alpha) + 1)!(2(\mu + \beta) + 1)!}$, $a_{11} = \cos(\xi_{ki})$, $a_{22} = \cos(\xi_{ki})$, $a_{12} = \sin(\xi_{ki})$, and $a_{21} = -\sin(\xi_{ki})$ with $\xi_{ki} = \arctan((-1)^{P_{RRC}} \sqrt{M m_j / (m_i m_k)})$ where m_i is the mass of the i th particle, M is the total mass and P is the number of permutations of $m_1 \rightarrow m_2 \rightarrow m_3 \rightarrow m_1$ as shown in Fig. 6.2. As the value of K increases, RRC become extremely computationally expensive limiting the usefulness of this approach.

Should I include this?: Note that this formalism is subject to roundoff error for large values of K . When large K is utilized, a recursion relation version should be utilized (see S. N. Ershov. *Nuclei Theory* **79**, 694-702 (2016)).

Utilizing the Jacobi coordinates 1 in Fig. 6.2, the Helium potential becomes

$$V(\mathbf{R}) = \frac{1}{r_{23}} - \frac{Z}{r_{12}} - \frac{Z}{r_{13}} \quad (6.23)$$

which can be rewritten as

$$W(\Omega_5) = RV(\mathbf{R}) = \frac{\beta_1}{x_1} - \frac{Z}{|\beta_1 \hat{y}_1 + \hat{x}_1/(2\beta_1)|} - \frac{Z}{|\beta_1 \hat{y}_1 - \hat{x}_1/(2\beta_1)|}. \quad (6.24)$$

By using the hyperspherical harmonics defined in eq. 6.14, with $\mathbf{r}_1 = \mathbf{x}_1$ and $\mathbf{r}_2 = \mathbf{y}_1$, the first term is easy to calculate through a 1D integral over α written explicitly below. However, the next two terms would require a 5D integral which is expensive and numerically unstable if computed directly. Instead, we will exchange particles in the coordinate system to allow the \mathbf{x}_i Jacobi coordinate to correspond to the distance between the two interacting particles. The result is a 1D integral over α that is similar to the e^-e^- repulsion term. To achieve this, we utilize RRC (eq. 6.22) which allow us to write

$$Y_{K,L,M}^{\ell_{x_i}, \ell_{y_i}} = \sum_{\ell_{x_j}, \ell_{y_j}} \langle \ell_{x_j}, \ell_{y_j} | \ell_{x_i}, \ell_{y_i} \rangle_{K,L} Y_{K,L,M}^{\ell_{x_j}, \ell_{y_j}}(\Omega_{5_j}) \quad (6.25)$$

where Ω_{5_i} and Ω_{5_j} are the solid angles in the Jacobi coordinates labeled by i, j . We note that K , L and M are conserved in this rotation allowing us to remove any subscripts.

For practical reasons, we need to calculate the matrix elements $\langle \mathbf{K}' | V(R=1, \Omega_{5_i}) | \mathbf{K} \rangle = \langle \mathbf{K}' | W(\Omega_{5_i}) | \mathbf{K} \rangle$ as the term $1/R$ can be factored out of $V(R, \Omega_{5_i})$ removing its dependence on R . We can then store the results of $\langle \mathbf{K}' | W(\Omega_{5_i}) | \mathbf{K} \rangle$ in a hash table to be looked up when building the matrix. **TODO: Cite M. A. Kahn et. al. 8 469 (1999)**

The electron electron repulsion term of $W(\Omega_5)$ becomes

$$\begin{aligned} \langle K' \ell'_{x_1} \ell'_{y_1} L' M' | \frac{1}{\sqrt{2} \cos \alpha_1} | K \ell_{x_1} \ell_{y_1} L M \rangle &= \frac{1}{\sqrt{2}} \delta_{\ell'_{x_1}, \ell_{x_1}} \delta_{\ell'_{y_1}, \ell_{y_1}} \delta_{L', L} \delta_{M', M} \\ &\times \int_0^{\pi/2} \tilde{P}_{n'}^{\ell'_{x_1}, \ell'_{y_1}}(\alpha_1) \tilde{P}_n^{\ell_{x_1}, \ell_{y_1}}(\alpha_1) \sin^2(\alpha_1) \cos(\alpha_1) d\alpha_1 \end{aligned} \quad (6.26)$$

$$(6.27)$$

where the delta functions come from the integral over $d\omega$.

The coulomb potential for the m_3 electron of $W(\Omega_5)$ becomes

$$\langle K' \ell'_{x_1} \ell'_{y_1} L' M' | R \frac{-Z}{r_{13}} | K \ell_{x_1} \ell_{y_1} L M \rangle = \sum_{\ell_{x_2}, \ell_{y_2}} \langle \ell_{x_2}, \ell_{y_2} | \ell'_{x_1}, \ell'_{y_1} \rangle_{K', L'} \langle \ell_{x_2}, \ell_{y_2} | \ell_{x_1}, \ell_{y_1} \rangle_{K, L} \quad (6.28)$$

$$\times \langle K' \ell'_{x_2} \ell'_{y_2} L' M' | \frac{-Z}{\cos \alpha_2} | K \ell_{x_2} \ell_{y_2} L M \rangle \quad (6.29)$$

with $P_{RRC} = 1$ and

$$\begin{aligned} \langle K' \ell'_{x_2} \ell'_{y_2} L' M' | \frac{1}{\sqrt{2} \cos \alpha_2} | K \ell_{x_2} \ell_{y_2} L M \rangle &= \frac{1}{\sqrt{2}} \delta_{\ell'_{x_2}, \ell_{x_2}} \delta_{\ell'_{y_2}, \ell_{y_2}} \delta_{L', L} \delta_{M', M} \\ &\times \int_0^{\pi/2} \tilde{P}_{n'}^{\ell'_{x_2}, \ell'_{y_2}}(\alpha_2) \tilde{P}_n^{\ell_{x_2}, \ell_{y_2}}(\alpha_2) \sin^2(\alpha_2) \cos(\alpha_2) d\alpha_2 \end{aligned} \quad (6.30)$$

$$(6.31)$$

and the coulomb potential for the m_2 electron of $W(\Omega_5)$ becomes

$$\langle K' \ell'_{x_1} \ell'_{y_1} L' M' | R \frac{-Z}{r_{12}} | K \ell_{x_1} \ell_{y_1} L M \rangle = \sum_{\ell_{x_3}, \ell_{y_3}} \langle \ell_{x_3}, \ell_{y_3} | \ell'_{x_1}, \ell'_{y_1} \rangle_{K', L'} \langle \ell_{x_3}, \ell_{y_3} | \ell_{x_1}, \ell_{y_1} \rangle_{K, L} \quad (6.32)$$

$$\times \langle K' \ell'_{x_3} \ell'_{y_3} L' M' | \frac{-Z}{\cos \alpha_3} | K \ell_{x_3} \ell_{y_3} L M \rangle \quad (6.33)$$

with $P_{RRC} = 2$ and

$$\begin{aligned} \langle K' \ell'_{x_3} \ell'_{y_3} L' M' | \frac{1}{\sqrt{2} \cos \alpha_3} | K \ell_{x_3} \ell_{y_3} L M \rangle &= \frac{1}{\sqrt{2}} \delta_{\ell'_{x_3}, \ell_{x_3}} \delta_{\ell'_{y_3}, \ell_{y_3}} \delta_{L', L} \delta_{M', M} \\ &\times \int_0^{\pi/2} \tilde{P}_{n'}^{\ell'_{x_3}, \ell'_{y_3}}(\alpha_3) \tilde{P}_n^{\ell_{x_3}, \ell_{y_3}}(\alpha_3) \sin^2(\alpha_3) \cos(\alpha_3) d\alpha_3. \end{aligned} \quad (6.34)$$

$$(6.35)$$

Next, the laser potential for a linearly polarized laser aligned along the lab's z -axis needs to be calculated. The potential term is

$$V_{las}(\mathbf{R}) = -E_z z_2 - E_z z_3 = -2E_z \frac{z_2 + z_3}{2}. \quad (6.36)$$

where z_2 and z_3 are the z components of the two electrons and E_z is the magnitude of the z component of the electric field. Therefore the laser couples to the z component of the center of

mass of the two electrons namely

$$\mathbf{r}_{2e_{cm}} = \frac{\mathbf{r}_2 + \mathbf{r}_3}{2}. \quad (6.37)$$

Noticing that y_1 from Eq. 6.16 contains $\mathbf{r}_{2e_{cm}}$, the laser term only appears in the \hat{y}_1 spherical harmonics. Now we need to calculate the $V_{las}(\mathbf{R})$ matrix element such that

$$\langle K'\ell'_{x_1}\ell'_{y_1}L'M' | -2E_z z_{2e_{cm}} | K\ell_{x_1}\ell_{y_1}LM \rangle. \quad (6.38)$$

In the infinite mass approximation, $\mathbf{R}_{cm} = \mathbf{r}_i$ and therefore

$$z_{2e_{cm}} = \beta_1 \mathbf{y}_1 \cdot \hat{z}_{cm} \quad (6.39)$$

$$= \frac{y_1 \cos(\theta_{y_1})}{\sqrt{2}} \quad (6.40)$$

$$= 2\sqrt{\frac{\pi}{6}} y_1 Y_{1,0}(\hat{y}_1) \quad (6.41)$$

$$= 2\sqrt{\frac{\pi}{6}} R \sin(\alpha_1) Y_{1,0}(\hat{y}_1) \quad (6.42)$$

Plugging this in we obtain

$$\langle K'\ell'_{x_1}\ell'_{y_1}L'M' | -2E_z z_{2e_{cm}} | K\ell_{x_1}\ell_{y_1}LM \rangle = -2E_z \langle K'\ell'_{x_1}\ell'_{y_1}L'M' | 2\sqrt{\frac{\pi}{6}} R \sin(\alpha_1) Y_{1,0}(\hat{y}_1) | K\ell_{x_1}\ell_{y_1}LM \rangle \quad (6.43)$$

which becomes

$$\begin{aligned} \langle K'\ell'_{x_1}\ell'_{y_1}L'M' | -2E_z z_{2e_{cm}} | K\ell_{x_1}\ell_{y_1}LM \rangle &= -2E_z \delta_{\ell'_{x_1}\ell_{x_1}} \delta_{M'M} R \sqrt{\frac{(2\ell'_{y_1}+1)}{2(2\ell_{y_1}+1)}} \\ &\times \left[\int_0^{\pi/2} \tilde{P}_{n'}^{\ell'_{x_1}, \ell'_{y_1}}(\alpha_1) \tilde{P}_n^{\ell_{x_1}, \ell_{y_1}}(\alpha_1) \sin^3(\alpha_1) \cos^2(\alpha_1) d\alpha_1 \right] \\ &\times \sum_{m'_x, m'_y, m_x, m_y} \left[\langle \ell'_{y_1}, 0, 1, 0 | \ell_{y_1}, 0 \rangle \langle \ell'_{y_1}, m'_y, 1, 0 | \ell_{y_1}, m_y \rangle \right. \\ &\times \langle \ell'_{x_1}, m'_x, \ell'_{y_1}, m'_y | L', M' \rangle \langle \ell_{x_1}, m_x, \ell_{y_1}, m_y | L, M \rangle \left. \right] \end{aligned} \quad (6.44)$$

Since the M quantum number does not change and $M = 0$ for the ground state of He. Therefore the sum over m'_x, m'_y, m_x, m_y simplifies to a single sum over $-\min(L', L) \leq m \leq \min(L', L)$ with

$m'_x = m_x = -m$ and $m'_y = m_y = m$ as we get $\delta_{m'_y, m_y}$ from the second CGC, $\delta_{m'_x, -m'_y}$ (when $M' = 0$) from the third CGC, and $\delta_{m_x, -m_y}$ (when $M = 0$) from the forth CGC. If $M \neq 0$ is needed, a different simplification is required.

6.1.1.3 Electronic Coordinates

To remove the need for RRC due to their numerical complexity for high K values, we will use the nucleus as the origin and label the coordinates from the proton to the i th electron as \mathbf{r}_i where $i = 1, 2$. Therefore we have

$$r_1 = R \cos(\alpha) \quad (6.45)$$

$$r_2 = R \sin(\alpha) \quad (6.46)$$

and a solid angle

$$d\Omega_5 = \cos^2(\alpha) \sin^2(\alpha) d\alpha d\omega_{r_1} d\omega_{r_2}. \quad (6.47)$$

We will use spherical harmonics with labels $Y_{K,L,M}^{\ell_{r_1}, \ell_{r_2}}(\Omega_5)$ where ℓ_{r_i} is the spherical harmonic for the 3D space \mathbf{r}_i . The electron nucleus terms take the form $-Z/r_i$ and the matrix elements become

$$-\langle \Psi' | \frac{Z}{r_1} | \Psi \rangle = -\frac{Z}{R} \delta_{L', L} \delta_{M', M} \delta_{\ell'_{r_1}, \ell_{r_1}} \delta_{\ell'_{r_2}, \ell_{r_2}} \int_0^{\pi/2} \tilde{P}_{n'}^{\ell'_{r_1}, \ell'_{r_2}}(\alpha) \tilde{P}_n^{\ell_{r_1}, \ell_{r_2}}(\alpha) \sin^2(\alpha) \cos(\alpha) d\alpha \quad (6.48)$$

and

$$-\langle \Psi' | \frac{Z}{r_2} | \Psi \rangle = -\frac{Z}{R} \delta_{L', L} \delta_{M', M} \delta_{\ell'_{r_1}, \ell_{r_1}} \delta_{\ell'_{r_2}, \ell_{r_2}} \int_0^{\pi/2} \tilde{P}_{n'}^{\ell'_{r_1}, \ell'_{r_2}}(\alpha) \tilde{P}_n^{\ell_{r_1}, \ell_{r_2}}(\alpha) \sin(\alpha) \cos^2(\alpha) d\alpha. \quad (6.49)$$

Note that the $1/R$ can be factored out allowing the integral over α to be preformed once and stored in a lookup table to improve computational performance.

The electron-electron term is less strait forward. We start by remembering the jackson formula

$$\frac{1}{|\mathbf{r}_1 - \mathbf{r}_2|} = \sum_{\ell=0}^{\infty} \sum_{m=-\ell}^{\ell} \frac{4\pi}{2\ell+1} \frac{r_{<}^{\ell}}{r_{>}^{\ell+1}} Y_{\ell, m}^*(\hat{\mathbf{r}}_2) Y_{\ell, m}(\hat{\mathbf{r}}_1) \quad (6.50)$$

and then after a few hours of math you arrive at

$$\langle \Psi' | \frac{1}{|\mathbf{r}_1 - \mathbf{r}_2|} | \Psi \rangle = \frac{\delta_{L',L} \delta_{M',M}}{R} \sqrt{\frac{(2\ell'_{r_1} + 1)(2\ell'_{r_2} + 1)}{(2\ell_{r_1} + 1)(2\ell_{r_2} + 1)}} \quad (6.51)$$

$$\times \sum_{\ell=\max(|\ell_{r_1}-\ell_{r_2}|, |\ell'_{r_1}-\ell'_{r_2}|)}^{\min(|\ell_{r_1}+\ell_{r_2}|, |\ell'_{r_1}+\ell'_{r_2}|)} \langle \ell'_{r_1}, 0, \ell, 0 | \ell_{r_1}, 0 \rangle \langle \ell'_{r_2}, 0, \ell, 0 | \ell_{r_2}, 0 \rangle \quad (6.52)$$

$$\times \left[\int_0^{\pi/4} \tilde{P}_{n'}^{\ell'_{r_1}, \ell'_{r_2}}(\alpha) \tilde{P}_n^{\ell_{r_1}, \ell_{r_2}}(\alpha) \frac{\sin^{\ell+2}(\alpha)}{\cos^{\ell-1}(\alpha)} d\alpha + \int_{\pi/4}^{\pi/2} \tilde{P}_{n'}^{\ell'_{r_1}, \ell'_{r_2}}(\alpha) \tilde{P}_n^{\ell_{r_1}, \ell_{r_2}}(\alpha) \frac{\cos^{\ell+2}(\alpha)}{\sin^{\ell-1}(\alpha)} d\alpha \right] \quad (6.53)$$

$$\times \sum_{m'_{r_1}=-\ell'_{r_1}, m'_{r_2}=M'-m'_{r_1}}^{\ell'_{r_1}} \langle L', M' | \ell'_{r_1}, m'_{r_1}, \ell'_{r_2}, m'_{r_2} \rangle \quad (6.54)$$

$$\times \sum_{m_{r_1}=-\ell_{r_1}, m_{r_2}=M-m_{r_1}, m=m_{r_1}-m'_{r_1}}^{\ell_{r_1}} (-1)^m \langle L, M | \ell_{r_1}, m_{r_1}, \ell_{r_2}, m_{r_2} \rangle \quad (6.55)$$

$$\times \langle \ell'_{r_1}, m'_{r_1}, \ell, m | \ell_{r_1}, m_{r_1} \rangle \langle \ell'_{r_2}, m'_{r_2}, \ell, m | \ell_{r_2}, m_{r_2} \rangle \quad (6.56)$$

note the requirement for the last row adds $m = m_{r_1} - m'_{r_1}$ and $m = m'_{r_2} - m_{r_2}$ which gives the $\delta_{M',M}$ as well.

Finally, we need the laser operator

$$V_{las}(\mathbf{R}) = -E_z z_{r_1} - E_z z_{r_2}. \quad (6.57)$$

Since each electron has its own 3D space, it is easier to calculate the laser operator for each electron independently. It is then convent to define

$$V_{las}(\mathbf{r}_1) = -E_z z_{r_1} = -2E_z z_{r_2} \sqrt{\frac{\pi}{3}} R \sin(\alpha_1) Y_{1,0}(\hat{r}_1), \quad (6.58)$$

$$V_{las}(\mathbf{r}_2) = -E_z z_{r_2} = -2E_z z_{r_1} \sqrt{\frac{\pi}{3}} R \sin(\alpha_1) Y_{1,0}(\hat{r}_2), \quad (6.59)$$

$$V_{las}(\mathbf{R}) = V_{las}(\mathbf{r}_1) + V_{las}(\mathbf{r}_2). \quad (6.60)$$

The resulting matrix elements are

$$\langle \Psi' | V_{las}(\mathbf{r}_1) | \Psi \rangle = -E_z R \sqrt{\frac{(2\ell'_{r_1} + 1)}{(2\ell_{r_1} + 1)}} \delta_{L', L \pm 1} \delta_{M', M} \delta_{\ell'_{r_1}, \ell_{r_1} \pm 1} \delta_{\ell'_{r_2}, \ell_{r_2}} \langle \ell'_{r_1}, 0, 1, 0 | \ell_{r_1}, 0 \rangle \quad (6.61)$$

$$\times \int_0^{\pi/2} \tilde{P}_{n'}^{\ell'_{r_1}, \ell'_{r_2}}(\alpha) \tilde{P}_n^{\ell_{r_1}, \ell_{r_2}}(\alpha) \sin^3(\alpha) \cos^2(\alpha) d\alpha \quad (6.62)$$

$$\times \sum_{m_r = -\min[\ell'_{r_1}, \ell_{r_1}, \ell'_{r_2}, \ell_{r_2}]}^{\min[\ell'_{r_1}, \ell_{r_1}, \ell'_{r_2}, \ell_{r_2}]} \langle \ell'_{r_1}, m_r, 1, 0 | \ell_{r_1}, m_r \rangle \quad (6.63)$$

$$\times \langle L', M | \ell'_{r_1}, m_r, \ell_{r_2}, -m_r \rangle \langle L, M | \ell_{r_1}, m_r, \ell_{r_2}, -m_r \rangle \quad (6.64)$$

and

$$\langle \Psi' | V_{las}(\mathbf{r}_2) | \Psi \rangle = -E_z R \sqrt{\frac{(2\ell'_{r_2} + 1)}{(2\ell_{r_2} + 1)}} \delta_{L', L \pm 1} \delta_{M', M} \delta_{\ell'_{r_1}, \ell_{r_1}} \delta_{\ell'_{r_2}, \ell_{r_2} \pm 1} \langle \ell'_{r_2}, 0, 1, 0 | \ell_{r_2}, 0 \rangle \quad (6.65)$$

$$\times \int_0^{\pi/2} \tilde{P}_{n'}^{\ell'_{r_1}, \ell'_{r_2}}(\alpha) \tilde{P}_n^{\ell_{r_1}, \ell_{r_2}}(\alpha) \sin^3(\alpha) \cos^2(\alpha) d\alpha \quad (6.66)$$

$$\times \sum_{m_r = -\min[\ell'_{r_1}, \ell_{r_1}, \ell'_{r_2}, \ell_{r_2}]}^{\min[\ell'_{r_1}, \ell_{r_1}, \ell'_{r_2}, \ell_{r_2}]} \langle \ell'_{r_2}, m_r, 1, 0 | \ell_{r_2}, m_r \rangle \quad (6.67)$$

$$\times \langle L', M | \ell_{r_1}, m_r, \ell'_{r_2}, -m_r \rangle \langle L, M | \ell_{r_1}, m_r, \ell_{r_2}, -m_r \rangle. \quad (6.68)$$

In this derivation, I used $M = 0$ therefore $m_{r_1} = -m_{r_2}$. For $M \neq 0$ adjustments to the sum are needed.

6.2 Application TBD

Chapter 7

Summary and Prospective

TODO

Bibliography

- [1] In this work we consider the case that ground and excited state have different magnetic quantum numbers ($m_g \neq m_e$). We note that for $m_g = m_e$ only the asymmetry parameters for odd γ are applicable.
- [2] The small discrepancy is due to the energy dependence of the one- and two-photon cross sections.
- [3] Lou Barreau, C. Leon M. Petersson, Markus Klinker, Antoine Camper, Carlos Marante, Timothy Gorman, Dietrich Kieseewetter, Luca Argenti, Pierre Agostini, Jesús González-Vázquez, Pascal Salières, Louis F. DiMauro, and Fernando Martín. Disentangling spectral phases of interfering autoionizing states from attosecond interferometric measurements. Phys. Rev. Lett., 122:253203, Jun 2019.
- [4] Annelise R. Beck, Birgitta Bernhardt, Erika R. Warrick, Mengxi Wu, Shaohao Chen, Mette B. Gaarde, Kenneth J. Schafer, Daniel M. Neumark, and Stephen R. Leone. Attosecond transient absorption probing of electronic superpositions of bound states in neon: detection of quantum beats. New Journal of Physics, 16(11):113016, November 2014.
- [5] Diego I. R. Boll, Omar A. Fojón, C. W. McCurdy, and Alicia Palacios. Angularly resolved two-photon above-threshold ionization of helium. Physical Review A, 99(2):023416, February 2019.
- [6] N. Böwering, T. Lischke, B. Schmidtke, N. Müller, T. Khalil, and U. Heinzmann. Asymmetry in Photoelectron Emission from Chiral Molecules Induced by Circularly Polarized Light. Physical Review Letters, 86(7):1187–1190, February 2001.
- [7] Francesca Calegari, Giuseppe Sansone, Salvatore Stagira, Caterina Vozzi, and Mauro Nisoli. Advances in attosecond science. Journal of Physics B: Atomic, Molecular and Optical Physics, 49(6):062001, February 2016.
- [8] A. L. Cavalieri, N. Müller, Th Uphues, V. S. Yakovlev, A. Baltuška, B. Horvath, B. Schmidt, L. Blümel, R. Holzwarth, S. Hendel, M. Drescher, U. Kleineberg, P. M. Echenique, R. Kienberger, F. Krausz, and U. Heinzmann. Attosecond spectroscopy in condensed matter. Nature, 449(7165):1029–1032, October 2007.
- [9] Szczepan Chelkowski and André D. Bandrauk. Sensitivity of spatial photoelectron distributions to the absolute phase of an ultrashort intense laser pulse. Physical Review A, 65(6):061802, February 2002.

- [10] Ming-Chang Chen, Christopher Mancuso, Carlos Hernández-García, Franklin Dollar, Ben Galloway, Dimitar Popmintchev, Pei-Chi Huang, Barry Walker, Luis Plaja, Agnieszka A. Jaroń-Becker, Andreas Becker, Margaret M. Murnane, Henry C. Kapteyn, and Tenio Popmintchev. Generation of bright isolated attosecond soft X-ray pulses driven by multicycle midinfrared lasers. Proceedings of the National Academy of Sciences, 111(23):E2361–E2367, 2014.
- [11] Michael Chini, Kun Zhao, and Zenghu Chang. The generation, characterization and applications of broadband isolated attosecond pulses. Nature Photonics, 8(3):178–186, March 2014.
- [12] Claudio Cirelli, Carlos Marante, Sebastian Heuser, C. L. M. Petersson, Álvaro Jiménez Galán, Luca Argenti, Shiyang Zhong, David Busto, Marcus Isinger, Saikat Nandi, Sylvain Maclot, Linnea Rading, Per Johnsson, Mathieu Gisselbrecht, Matteo Lucchini, Lukas Gallmann, J. Marcus Dahlström, Eva Lindroth, Anne L’Huillier, Fernando Martín, and Ursula Keller. Anisotropic photoemission time delays close to a Fano resonance. Nature Communications, 9(1):1–9, March 2018.
- [13] V. K. Dolmatov, A. S. Kheifets, P. C. Deshmukh, and S. T. Manson. Attosecond time delay in the photoionization of mn in the region of the $3p \rightarrow 3d$ giant resonance. Phys. Rev. A, 91:053415, May 2015.
- [14] Nicolas Douguet, Alexei N. Grum-Grzhimailo, Elena V. Gryzlova, Ekaterina I. Staroselskaya, Joel Venzke, and Klaus Bartschat. Photoelectron angular distributions in bichromatic atomic ionization induced by circularly polarized VUV femtosecond pulses. Physical Review A, 93(3):033402, March 2016.
- [15] H. Eichmann, A. Egbert, S. Nolte, C. Momma, B. Wellegehausen, W. Becker, S. Long, and J. K. McIver. Polarization-dependent high-order two-color mixing. Phys. Rev. A, 51:R3414–R3417, May 1995.
- [16] Tingting Fan, Patrik Grychtol, Ronny Knut, Carlos Hernández-García, Daniel D. Hickstein, Dmitriy Zusin, Christian Gentry, Franklin J. Dollar, Christopher A. Mancuso, Craig W. Hogle, Ofer Kfir, Dominik Legut, Karel Carva, Jennifer L. Ellis, Kevin M. Dorney, Cong Chen, Oleg G. Shpyrko, Eric E. Fullerton, Oren Cohen, Peter M. Oppeneer, Dejan B. Milošević, Andreas Becker, Agnieszka A. Jaroń-Becker, Tenio Popmintchev, Margaret M. Murnane, and Henry C. Kapteyn. Bright circularly polarized soft X-ray high harmonics for X-ray magnetic circular dichroism. Proceedings of the National Academy of Sciences, 112(46):14206–14211, November 2015.
- [17] J. Feist, S. Nagele, C. Ticknor, B. I. Schneider, L. A. Collins, and J. Burgdörfer. Attosecond two-photon interferometry for doubly excited states of helium. Phys. Rev. Lett., 107:093005, Aug 2011.
- [18] Avner Fleischer, Ofer Kfir, Tzvi Diskin, Pavel Sidorenko, and Oren Cohen. Spin angular momentum and tunable polarization in high-harmonic generation. Nature Photonics, 8(7):543–549, July 2014.
- [19] Bengt Fornberg. Generation of finite difference formulas on arbitrarily spaced grids. Mathematics of Computation, 51(184):699–706, 1988.
- [20] Bengt Fornberg and Natasha Flyer. A Primer on Radial Basis Functions with Applications to the Geosciences. Society for Industrial and Applied Mathematics, Philadelphia, PA, 2015.

- [21] Gustavo A. Garcia, Laurent Nahon, Steven Daly, and Ivan Powis. Vibrationally induced inversion of photoelectron forward-backward asymmetry in chiral molecule photoionization by circularly polarized light. *Nature Communications*, 4(1):2132, July 2013.
- [22] Xiaochun Gong, Cheng Lin, Feng He, Qiying Song, Kang Lin, Qinying Ji, Wenbin Zhang, Junyang Ma, Peifen Lu, Yunquan Liu, Heping Zeng, Weifeng Yang, and Jian Wu. Energy-resolved ultrashort delays of photoelectron emission clocked by orthogonal two-color laser fields. *Phys. Rev. Lett.*, 118:143203, Apr 2017.
- [23] Eleftherios Goulielmakis, Zhi-Heng Loh, Adrian Wirth, Robin Santra, Nina Rohringer, Vladislav S. Yakovlev, Sergey Zherebtsov, Thomas Pfeifer, Abdallah M. Azzeer, Matthias F. Kling, Stephen R. Leone, and Ferenc Krausz. Real-time observation of valence electron motion. *Nature*, 466(7307):739–743, August 2010.
- [24] Alexei N. Grum-Grzhimailo, Elena V. Gryzlova, Ekaterina I. Staroselskaya, Joel Venzke, and Klaus Bartschat. Interfering one-photon and two-photon ionization by femtosecond VUV pulses in the region of an intermediate resonance. *Physical Review A*, 91(6):063418, June 2015.
- [25] V. Gruson, L. Barreau, á Jiménez-Galan, F. Risoud, J. Caillat, A. Maquet, B. Carré, F. Lepetit, J.-F. Hergott, T. Ruchon, L. Argenti, R. Taïeb, F. Martín, and P. Salières. Attosecond dynamics through a Fano resonance: Monitoring the birth of a photoelectron. *Science*, 354(6313):734–738, November 2016.
- [26] M. Th Hassan, T. T. Luu, A. Moulet, O. Raskazovskaya, P. Zhokhov, M. Garg, N. Karpowicz, A. M. Zheltikov, V. Pervak, F. Krausz, and E. Goulielmakis. Optical attosecond pulses and tracking the nonlinear response of bound electrons. *Nature*, 530(7588):66–70, February 2016.
- [27] F. He, C. Ruiz, and A. Becker. Absorbing boundaries in numerical solutions of the time-dependent schrödinger equation on a grid using exterior complex scaling. *Phys. Rev. A*, 75:053407, May 2007.
- [28] Mingrui He, Yang Li, Yueming Zhou, Min Li, Wei Cao, and Peixiang Lu. Direct visualization of valence electron motion using strong-field photoelectron holography. *Phys. Rev. Lett.*, 120:133204, Mar 2018.
- [29] Daniel D. Hickstein, Franklin J. Dollar, Patrik Grychtol, Jennifer L. Ellis, Ronny Knut, Carlos Hernández-García, Dmitriy Zusin, Christian Gentry, Justin M. Shaw, Tingting Fan, Kevin M. Dorney, Andreas Becker, Agnieszka Jaroń-Becker, Henry C. Kapteyn, Margaret M. Murnane, and Charles G. Durfee. Non-collinear generation of angularly isolated circularly polarized high harmonics. *Nature Photonics*, 9(11):743–750, November 2015.
- [30] Paul Hockett, Christer Z. Bisgaard, Owen J. Clarkin, and Albert Stolow. Time-resolved imaging of purely valence-electron dynamics during a chemical reaction. *Nature Physics*, 7(8):612–615, August 2011.
- [31] J. Hofbrucker, A. V. Volotka, and S. Fritzsche. Maximum elliptical dichroism in atomic two-photon ionization. *Phys. Rev. Lett.*, 121:053401, Jul 2018.
- [32] M. Holler, F. Schapper, L. Gallmann, and U. Keller. Attosecond electron wave-packet interference observed by transient absorption. *Phys. Rev. Lett.*, 106:123601, Mar 2011.

- [33] S. X. Hu and L. A. Collins. Attosecond pump probe: Exploring ultrafast electron motion inside an atom. Phys. Rev. Lett., 96:073004, Feb 2006.
- [34] Pei-Chi Huang, Carlos Hernández-García, Jen-Ting Huang, Po-Yao Huang, Chih-Hsuan Lu, Laura Rego, Daniel D. Hickstein, Jennifer L. Ellis, Agnieszka Jaron-Becker, Andreas Becker, Shang-Da Yang, Charles G. Durfee, Luis Plaja, Henry C. Kapteyn, Margaret M. Murnane, A. H. Kung, and Ming-Chang Chen. Polarization control of isolated high-harmonic pulses. Nature Photonics, 12(6):349–354, June 2018.
- [35] M. Ilchen, G. Hartmann, E. V. Gryzlova, A. Achner, E. Allaria, A. Beckmann, M. Braune, J. Buck, C. Callegari, R. N. Coffee, R. Cucini, M. Danailov, A. De Fanis, A. Demidovich, E. Ferrari, P. Finetti, L. Glaser, A. Knie, A. O. Lindahl, O. Plekan, N. Mahne, T. Mazza, L. Raimondi, E. Roussel, F. Scholz, J. Seltmann, I. Shevchuk, C. Svetina, P. Walter, M. Zangrando, J. Viefhaus, A. N. Grum-Grzhimailo, and M. Meyer. Symmetry breakdown of electron emission in extreme ultraviolet photoionization of argon. Nature Communications, 9(1):4659, November 2018.
- [36] Kenichi L. Ishikawa and Kiyoshi Ueda. Competition of resonant and nonresonant paths in resonance-enhanced two-photon single ionization of he by an ultrashort extreme-ultraviolet pulse. Phys. Rev. Lett., 108:033003, Jan 2012.
- [37] M. Isinger, R. J. Squibb, D. Busto, S. Zhong, A. Harth, D. Kroon, S. Nandi, C. L. Arnold, M. Miranda, J. M. Dahlström, E. Lindroth, R. Feifel, M. Gisselbrecht, and A. L’Huillier. Photoionization in the time and frequency domain. Science, 358(6365):893–896, November 2017.
- [38] Wei-Chao Jiang, Xiao-Min Tong, Renate Pazourek, Stefan Nagele, and Joachim Burgdörfer. Theory of bound-state coherences generated and probed by optical attosecond pulses. Phys. Rev. A, 101:053435, May 2020.
- [39] Álvaro Jiménez-Galán, Luca Argenti, and Fernando Martín. Modulation of attosecond beating in resonant two-photon ionization. Phys. Rev. Lett., 113:263001, Dec 2014.
- [40] A. Kaldun, A. Blättermann, V. StooB, S. Donsa, H. Wei, R. Pazourek, S. Nagele, C. Ott, C. D. Lin, J. Burgdörfer, and T. Pfeifer. Observing the ultrafast buildup of a Fano resonance in the time domain. Science, 354(6313):738–741, November 2016.
- [41] Kyung Taec Kim, Dong Hyuk Ko, Juyun Park, Nark Nyul Choi, Chul Min Kim, Kenichi L. Ishikawa, Jongmin Lee, and Chang Hee Nam. Amplitude and phase reconstruction of electron wave packets for probing ultrafast photoionization dynamics. Phys. Rev. Lett., 108:093001, Feb 2012.
- [42] K. Klünder, J. M. Dahlström, M. Gisselbrecht, T. Fordell, M. Swoboda, D. Guénot, P. Johnsson, J. Caillat, J. Mauritsson, A. Maquet, R. Taïeb, and A. L’Huillier. Probing single-photon ionization on the attosecond time scale. Phys. Rev. Lett., 106:143002, Apr 2011.
- [43] K. Klünder, P. Johnsson, M. Swoboda, A. L’Huillier, G. Sansone, M. Nisoli, M. J. J. Vrakking, K. J. Schafer, and J. Mauritsson. Reconstruction of attosecond electron wave packets using quantum state holography. Phys. Rev. A, 88:033404, Sep 2013.

- [44] M. Kotur, D. Guénot, á Jiménez-Galán, D. Kroon, E. W. Larsen, M. Louisy, S. Bengtsson, M. Miranda, J. Mauritsson, C. L. Arnold, S. E. Canton, M. Gisselbrecht, T. Carette, J. M. Dahlström, E. Lindroth, A. Maquet, L. Argenti, F. Martín, and A. L’Huillier. Spectral phase measurement of a Fano resonance using tunable attosecond pulses. Nature Communications, 7(1):10566, February 2016.
- [45] R. Ma, K. Motomura, K. L. Ishikawa, S. Mondal, H. Fukuzawa, A. Yamada, K. Ueda, K. Nagaya, S. Yase, Y. Mizoguchi, M. Yao, A. Rouze, A. Hundermark, M. J. J. Vrakking, P. Johnsson, M. Nagasono, K. Tono, T. Togashi, Y. Senba, H. Ohashi, M. Yabashi, and T. Ishikawa. Photoelectron angular distributions for the two-photon ionization of helium by ultrashort extreme ultraviolet free-electron laser pulses. Journal of Physics B: Atomic, Molecular and Optical Physics, 46(16):164018, August 2013.
- [46] F. Maulbetsch and J. S. Briggs. Asymmetry parameter for double photoionization. Physical Review Letters, 68(13):2004–2006, March 1992.
- [47] J. Mauritsson, T. Remetter, M. Swoboda, K. Klünder, A. L’Huillier, K. J. Schafer, O. Ghafer, F. Kelkensberg, W. Siu, P. Johnsson, M. J. J. Vrakking, I. Znakovskaya, T. Uphues, S. Zherebtsov, M. F. Kling, F. Lépine, E. Benedetti, F. Ferrari, G. Sansone, and M. Nisoli. Attosecond electron spectroscopy using a novel interferometric pump-probe technique. Phys. Rev. Lett., 105:053001, Jul 2010.
- [48] T. Mazza, M. Ilchen, A. J. Rafipoor, C. Callegari, P. Finetti, O. Plekan, K. C. Prince, R. Richter, M. B. Danailov, A. Demidovich, G. De Ninno, C. Grazioli, R. Ivanov, N. Mahne, L. Raimondi, C. Svetina, L. Avaldi, P. Bolognesi, M. Coreno, P. O’Keeffe, M. Di Fraia, M. Devetta, Y. Ovcharenko, Th Möller, V. Lyamayev, F. Stienkemeier, S. Düsterer, K. Ueda, J. T. Costello, A. K. Kazansky, N. M. Kabachnik, and M. Meyer. Determining the polarization state of an extreme ultraviolet free-electron laser beam using atomic circular dichroism. Nature Communications, 5(1):1–6, April 2014.
- [49] K. C. McCormick, Keller J., Burd S. C., Wineland D. J., Wilson A. C., and Leibfried D. Quantum-enhanced sensing of a single-ion mechanical oscillator. Nature, 572:86, 2019.
- [50] Erik P. Månsson, Diego Guénot, Cord L. Arnold, David Kroon, Susan Kasper, J. Marcus Dahlström, Eva Lindroth, Anatoli S. Kheifets, Anne L’Huillier, Stacey L. Sorensen, and Mathieu Gisselbrecht. Double ionization probed on the attosecond timescale. Nature Physics, 10(3):207–211, March 2014.
- [51] H. G. Muller. Reconstruction of attosecond harmonic beating by interference of two-photon transitions. Applied Physics B, 74(1):s17–s21, June 2002.
- [52] Christian Ott, Andreas Kaldun, Luca Argenti, Philipp Raith, Kristina Meyer, Martin Laux, Yizhu Zhang, Alexander Blättermann, Steffen Hagstotz, Thomas Ding, Robert Heck, Javier Madroño, Fernando Martín, and Thomas Pfeifer. Reconstruction and control of a time-dependent two-electron wave packet. Nature, 516(7531):374–378, December 2014.
- [53] P. M. Paul, E. S. Toma, P. Breger, G. Mullot, F. Augé, Ph Balcou, H. G. Muller, and P. Agostini. Observation of a Train of Attosecond Pulses from High Harmonic Generation. Science, 292(5522):1689–1692, June 2001.

- [54] Renate Pazourek, Johannes Feist, Stefan Nagele, and Joachim Burgdörfer. Attosecond streaking of correlated two-electron transitions in helium. Phys. Rev. Lett., 108:163001, Apr 2012.
- [55] Renate Pazourek, Stefan Nagele, and Joachim Burgdörfer. Attosecond chronoscopy of photoemission. Rev. Mod. Phys., 87:765–802, Aug 2015.
- [56] Peng Peng, Claude Marceau, and David M. Villeneuve. Attosecond imaging of molecules using high harmonic spectroscopy. Nature Reviews Physics, 1(2):144–155, February 2019.
- [57] Adrian N. Pfeiffer, Claudio Cirelli, Mathias Smolarski, Reinhard Dörner, and Ursula Keller. Timing the release in sequential double ionization. Nature Physics, 7(5):428–433, May 2011.
- [58] Tenio Popmintchev, Ming-Chang Chen, Paul Arpin, Margaret M. Murnane, and Henry C. Kapteyn. The attosecond nonlinear optics of bright coherent X-ray generation. Nature Photonics, 4:822, 2010.
- [59] Katharina E. Priebe, Christopher Rathje, Sergey V. Yalunin, Thorsten Hohage, Armin Feist, Sascha Schäfer, and Claus Ropers. Attosecond electron pulse trains and quantum state reconstruction in ultrafast transmission electron microscopy. Nature Photonics, 11(12):793–797, December 2017.
- [60] K. C. Prince, E. Allaria, C. Callegari, R. Cucini, G. De Ninno, S. Di Mitri, B. Diviacco, E. Ferrari, P. Finetti, D. Gauthier, L. Giannessi, N. Mahne, G. Penco, O. Plekan, L. Raimondi, P. Rebernik, E. Roussel, C. Svetina, M. Trovò, M. Zangrando, M. Negro, P. Carpeggiani, M. Reduzzi, G. Sansone, A. N. Grum-Grzhimailo, E. V. Gryzlova, S. I. Strakhova, K. Bartschat, N. Douguet, J. Venzke, D. Iablonskyi, Y. Kumagai, T. Takanashi, K. Ueda, A. Fischer, M. Coreno, F. Stienkemeier, Y. Ovcharenko, T. Mazza, and M. Meyer. Coherent control with a short-wavelength free-electron laser. Nature Photonics, 10(3):176–179, March 2016.
- [61] Krupa Ramasesha, Stephen R. Leone, and Daniel M. Neumark. Real-Time Probing of Electron Dynamics Using Attosecond Time-Resolved Spectroscopy. Annual Review of Physical Chemistry, 67(1):41–63, May 2016.
- [62] Ran Reiff, Tennessee Joyce, Agnieszka Jaron-Becker, and Andreas Becker. Single-active electron calculations of high-order harmonic generation from valence shells in atoms for quantitative comparison with TDDFT calculations. Journal of Physics Communications, 2020.
- [63] T. Remetter, P. Johnsson, J. Mauritsson, K. Varjú, Y. Ni, F. Lépine, E. Gustafsson, M. Kling, J. Khan, R. López-Martens, K. J. Schafer, M. J. J. Vrakking, and A. L’Huillier. Attosecond electron wave packet interferometry. Nature Physics, 2(5):323–326, May 2006.
- [64] Womersley RS and Sloan IH. Interpolation and cubature on the sphere. <http://web.maths.unsw.edu.au/~rsw/Sphere/>, year = 2007.
- [65] M. Sabbar, S. Heuser, R. Boge, M. Lucchini, T. Carette, E. Lindroth, L. Gallmann, C. Cirelli, and U. Keller. Resonance effects in photoemission time delays. Phys. Rev. Lett., 115:133001, Sep 2015.
- [66] M Saffman. Quantum computing with atomic qubits and rydberg interactions: progress and challenges. Journal of Physics B: Atomic, Molecular and Optical Physics, 49(20):202001, oct 2016.

- [67] M. Schultze, M. Fieß, N. Karpowicz, J. Gagnon, M. Korbman, M. Hofstetter, S. Neppl, A. L. Cavalieri, Y. Komninos, Th Mercouris, C. A. Nicolaides, R. Pazourek, S. Nagele, J. Feist, J. Burgdörfer, A. M. Azzeer, R. Ernstorfer, R. Kienberger, U. Kleineberg, E. Goulielmakis, F. Krausz, and V. S. Yakovlev. Delay in Photoemission. Science, 328(5986):1658–1662, June 2010.
- [68] Armin Scrinzi. Infinite-range exterior complex scaling as a perfect absorber in time-dependent problems. Phys. Rev. A, 81:053845, May 2010.
- [69] E. A. Seddon, J. A. Clarke, D. J. Dunning, C. Masciovecchio, C. J. Milne, F. Parmigiani, D. Rugg, J. C. H. Spence, N. R. Thompson, K. Ueda, S. M. Vinko, J. S. Wark, and W. Wurth. Short-wavelength free-electron laser sources and science: a review. Reports on Progress in Physics, 80(11):115901, October 2017.
- [70] C. Spezzani, E. Allaria, M. Coreno, B. Diviacco, E. Ferrari, G. Geloni, E. Karantzoulis, B. Mahieu, M. Vento, and G. De Ninno. Coherent light with tunable polarization from single-pass free-electron lasers. Phys. Rev. Lett., 107:084801, Aug 2011.
- [71] Jing Su, Hongcheng Ni, Agnieszka Jaroń Becker, and Andreas Becker. Time delays in two-photon ionization. Phys. Rev. Lett., 113:263002, Dec 2014.
- [72] Zhensheng Tao, Cong Chen, Tibor Szilvási, Mark Keller, Manos Mavrikakis, Henry Kapteyn, and Margaret Murnane. Direct time-domain observation of attosecond final-state lifetimes in photoemission from solids. Science, 353(6294):62–67, July 2016.
- [73] J. Venzke, A. Becker, and A. Jaron-Becker. submitted for publication.
- [74] J. Venzke, A. Jaron-Becker, and A. Becker. Ionization of helium by an ultrashort extreme-ultraviolet laser pulse. Journal of Physics B: Atomic, Molecular and Optical Physics, 53(8):085602, April 2020.
- [75] J. Venzke, T. Joyce, Z. Xue, A. Becker, and A. Jaron-Becker. Central frequency of few-cycle laser pulses in strong-field processes. Physical Review A, 98(6):063409, December 2018.
- [76] Marc J. J. Vrakking. Attosecond imaging. Physical Chemistry Chemical Physics, 16(7):2775–2789, January 2014.
- [77] Samuel G. Walt, Niraghatam Bhargava Ram, Marcos Atala, Nikolay I. Shvetsov-Shilovski, Aaron von Conta, Denitsa Baykusheva, Manfred Lein, and Hans Jakob Wörner. Dynamics of valence-shell electrons and nuclei probed by strong-field holography and rescattering. Nature Communications, 8(1):1–8, June 2017.
- [78] Mu-Xue Wang, Hao Liang, Xiang-Ru Xiao, Si-Ge Chen, and Liang-You Peng. Time-dependent perturbation theory beyond the dipole approximation for two-photon ionization of atoms. Physical Review A, 99(2):023407, February 2019.
- [79] Xinhua Xie, Stefan Roither, Daniil Kartashov, Emil Persson, Diego G. Arbó, Li Zhang, Stefanie Gräfe, Markus S. Schöffler, Joachim Burgdörfer, Andrius Baltuška, and Markus Kitzler. Attosecond probe of valence-electron wave packets by subcycle sculpted laser fields. Phys. Rev. Lett., 108:193004, May 2012.

- [80] Junliang Xu, Cosmin I. Blaga, Pierre Agostini, and Louis F. DiMauro. Time-resolved molecular imaging. Journal of Physics B: Atomic, Molecular and Optical Physics, 49(11):112001, May 2016.
- [81] Yi-Yian Yin, Ce Chen, D. S. Elliott, and A. V. Smith. Asymmetric photoelectron angular distributions from interfering photoionization processes. Physical Review Letters, 69(16):2353–2356, October 1992.
- [82] Linda Young, Kiyoshi Ueda, Markus Gühr, Philip H. Bucksbaum, Marc Simon, Shaul Mukamel, Nina Rohringer, Kevin C. Prince, Claudio Masciovecchio, Michael Meyer, Artem Rudenko, Daniel Rolles, Christoph Bostedt, Matthias Fuchs, David A. Reis, Robin Santra, Henry Kapteyn, Margaret Murnane, Heide Ibrahim, François Légaré, Marc Vrakking, Marcus Isinger, David Kroon, Mathieu Gisselbrecht, Anne L’Huillier, Hans Jakob Wörner, and Stephen R. Leone. Roadmap of ultrafast x-ray atomic and molecular physics. Journal of Physics B: Atomic, Molecular and Optical Physics, 51(3):032003, January 2018.
- [83] Kun Zhao, Qi Zhang, Michael Chini, Yi Wu, Xiaowei Wang, and Zenghu Chang. Tailoring a 67 attosecond pulse through advantageous phase-mismatch. Opt. Lett., 37(18):3891–3893, Sep 2012.